Dissertation
submitted to the
Combined Faculties for Natural Sciences and for Mathematics
of the Ruperto-Carola University of Heidelberg, Germany
for the degree of
Doctor of Natural Sciences

presented by
**Dipl.-Phys. Michael Lestinsky**
born in Ostrava

Oral examination: April 18th, 2007.

# High-Resolution Electron Collision Spectroscopy with Multicharged Ions in Merged Beams

**Michael Lestinsky**

Referees:
Prof. Dr. Andreas Wolf
Prof. Dr. H.-Jürgen Kluge

Zusammenfassung:

Der Heidelberger Ionenspeicherring Tsr erlaubt es, gegenwärtig als einziger Ring, den gespeicherten Ionenstrahl parallel mit zwei Elektronenstrahlen zu überlagern. Dies verbessert erheblich das Potential für Stoßexperimente von Elektronen mit Ionen und ermöglicht es den Ionenstrahl mittels eines Elektronenstrahls zu kühlen, während gleichzeitig der andere als dediziertes Target für energieaufgelöste Elektronenstoßprozesse, wie Rekombination, verwendet wird. Diese Arbeit beschreibt die Implementation dieses Systems für erste Elektronenstoßexperimente. Ein Nachweissystem, einschließlich Detektoraufbau und einem Softwaresystem und Instrumentierung für die spektroskopische Strahlsteuerung, wurde realisiert. Ferner wurden zur Steigerung der spektroskopischen Auflösung systematische Untersuchungen der intrinsischen Relaxationsprozesse in Abhängigkeit von verschiedenen Parametern der Elektronenstrahlerzeugung durchgeführt. Diese sind unter anderem die Elektronendichte, die Feldstärke des magnetischen Führungsfeldes und die Geometrie der Beschleunigungsstruktur. Durch Rekombinationsmessungen an tiefliegenden Resonanzen in lithiumartigem $Sc^{18+}$ wurde die $2s - 2p_{3/2}$-Übergangsenergie mit hoher Präzision bestimmt. Der Strahlbetrieb des Zwei-Elektronenstrahlen-Aufbaus wurde bei hohen Resonanzenergien ($\approx 1000$ eV) an wasserstoffartigem $Mg^{11+}$ untersucht. Schließlich wurde die einzigartige Möglichkeit, die Geometrie des Zusammenführens von Elektronen- und Ionenstrahl zu modifizieren, genutzt um dessen Bedeutung für die Elektron-Ion-Rekombinationsrate bei kleinsten Relativenergien, anhand von $F^{6+}$, zu zeigen.

Abstract:

The Heidelberg ion storage ring Tsr is currently the only ring equipped with two independent devices for the collinear merging of a cold electron beam with stored ions. This greatly improves the potential of electron-ion collision experiments, as the ion beam can be cooled with one electron beam, while the other one is used as a dedicated target for energy-resolved electron collision processes, such as recombination. The work describes the implementation of this system for first electron collision spectroscopy experiments. A detection system has been realized including an ion detector and specroscopic beam-control software and instrumentation. Moreover, in order to improve the spectroscopic resolution systematical studies of intrinsic relaxation processes in the electron beam have been carried out. These include the dependence on the electron beam density, the magnetic guiding field strength, and the acceleration geometry. The recombination measurements on low-lying resonances in lithiumlike $Sc^{18+}$ yield a high-precision measurement of the $2s - 2p_{3/2}$ transition energy in this system. Operation of the two-electron-beam setup at high collision energy ($\approx 1000$ eV) is established using resonances of hydrogenlike $Mg^{11+}$, while the unique possibility of modifying the beam-merging geometry confirms its importance for the electron-ion recombination rate at lowest relative energy, as demonstrated on $F^{6+}$.

# Contents

# Chapter 1

# Introduction

Spectroscopy played an important role in physics since the works of the lens maker Baruch Spinoza, and of Christiaan Huygens on optical instruments back in the European Age of Enlightenment. Sir Isaac Newton was one of the first who darkened his laboratory to let light from the sun passing through a small slit and fall onto a prism producing spectral decomposition. Later Bunsen and Kirchhoff repeated this experiment and pioneered many applications of spectroscopy. In 1885 Joachim Jakob Balmer discovered a simple empirical formula for the structure of absorption lines in atomic hydrogen. An understanding of this formula began to evolve only when Niels Bohr proclaimed a simple model for atomic structure which could for the first time describe the structure of the line spectrum of atomic hydrogen. Later quantum theory began to formulate a conclusive model for the atomic structure.

With progressing technology and experimental methods new fields were opened and scientists began studies of ionized matter in the plasma state. Here ions are constantly colliding with each other or with electrons, and various types of reactions may be induced, such as excitation, ionization or recombination. The observed recombination rate of ions and electrons in a plasma was enhanced over theoretical estimations and a new possible channel, dielectronic recombination (DR), was proposed to explain the discrepancy in the 1930s. The process is understood as a free electron interacting with an electron bound to an ion. This Coulomb interaction transfers energy from the free to the bound electron and the initially free electron ends up bound to the ionic potential. A doubly excited state is formed which has several ways for stabilization, one being the auto-ionization by reversal of the capture process, and the other being radiative deexcitation leading into a singly excited state which is then stable against auto-ionization.

It took another half century of technological advances until DR could be observed under well defined conditions in a laboratory and considered as a highly resolving spectroscopic method. Only by the advent of heavy ion accelerators and storage rings was it possible to produce and sustain large amounts of highly charged heavy ions and bring them into uniform motion. Overlapped with a mono-energetic co-propagating electron cloud, the reaction products can be generated at sufficient intensity and detected with high efficiency.

Modern experimental fields for studies of the atomic structure are contributions from nuclear, many-body, and QED effects, which reveal themselves among others by the energetic positions of DR resonances. Moreover, DR rate measurements provide valuable data to the fields of plasma physics and astrophysics. They can even be used for identification and modeling of stellar plasmas from distant stars and thus for studies of the structure of the universe.

With the development of a new electron beam device as dedicated high resolution electron target [Spr03] for the Max-Planck-Institut für Kernphysik heavy ion storage ring TSR with a high yield thermionic electron gun and an alternative cryogenic photocathode [Wei03] the energy spread of the scanning electron beam has been significantly reduced, strongly improving the achievable resolution. Furthermore the electron target implements a concept of adiabatic acceleration for reduction of relaxation mechanisms inside the electron beam. Systematic studies of the relaxation processes allowed the electron beam parameters to be optimized substantially. The results of this research will be of great help for the design of new electron beam devices at future storage ring facilities, such as the NESR [SPA04] and the CSR [ZWS+05].

To complete the setup for electron-ion collision reactions the planned setup [Wis02] for detection of atomic ions has been realized and taken into operation. A versatile data acquisition system for control of the experiment and readout of various detector instruments has been set up. Moreover, a systematic test series was performed in order to understand the properties of the acceleration scheme and to optimize the precision of electron collision experiments. With the completed setup a number of beamtimes with atomic and molecular ions have been performed. Here, three beamtimes on atomic ions will be discussed in order to point out advantages of the electron target setup. First, the measurement on $Sc^{18+}$ demonstrates the capability of exceptionally low energy resolution for low-energy dielectronic recombination. Then, a measurement on DR in hydrogenlike $Mg^{11+}$ investigates the electron beam properties at highest relative energies of up to $\approx$ 1500 eV. Finally, low-energy recombination in lithiumlike $F^{6+}$ is studied using the advantages of the electron target and cooler combination, which offers continuous phase-space cooling of the ion beam and allows to basically modify the merging field geometry in the electron target.

To pick up the historic digression of the beginning, spectroscopy is a vivid field of state-of-the-art research, albeit the experimental methods have changed dramatically during the past 400 years. One powerful method is energy-resolved electron collision with ions, which gives an insight into the innermost atomic shell, where other spectroscopic methods are not available. Experimental data are vital for many fields of present research, such as atomic structure or the understanding of ionic plasmas.

This work is organized as follows. The present state of experimental and theoretical understanding of electron collision spectroscopy is presented in Chapter 2. Chapter 3 gives an overview of the experimental setup used in this work. Chapter 4 describes various experimental and methodic measures to decrease the energy spread and instabilities of the electron beam. The three example ionic systems mentioned above making use of the advantages of the electron target setup for experiments on electron induced

reactions are discussed in Chapter 5. Chapter 6 summarizes the results and gives an outlook for future experiments at the planned NESR storage ring in Darmstadt and the cryogenic electrostatic storage ring CSR in Heidelberg.

# Chapter 2

# The framework of electron collision spectroscopy

## 2.1 Motivation and experimental methods

The motivation for studies of multiply charged ions by electron impact reactions is driven mainly by two different fields, atomic structure theory and plasma physics. Depending on the impact energy, different reaction channels are open for resonant dielectronic or non-resonant radiative electron capture or electron impact ionization. The resonant process gives a deep insight into the atomic structure of the ion and allows comparison with state of the art theoretical calculations. Especially simple, few-electron ionic systems are of concern for these studies, as the structure codes have to take care of electron-electron correlations, nuclear effects (hyperfine structure, nuclear charge radius). Lithium-like systems are of special interest, as they give access to a system with a closed inner K shell and one electron in the L shell. This $2l$ electron is, apart from correlations to the inner shell and nuclear influence, mostly undisturbed and gives access to the $2s - 2p$ Lamb-shift.

Experimental studies of $2s - 2p$ transitions in Li-like systems have been carried out applying various methods. Storage ring dielectronic recombination experiments were performed on $F^{6+}$ [TEG+02], $Na^{8+}$ [NLK+04] and $Sc^{18+}$ [KSS+04]. Recently the $2p_{1/2} - 2s$ deexcitation energy in $U^{89+}$ could be measured [BCTT05] at the Livermore SuperEBIT.

Reactions of electrons with multiply charged ions are observable also in astrophysical plasma, such as stellar coronae, active galactic nucleae (AGN), or planetary nebulae (PNe) and supernova remnants (SNR). The originating plasmas consist of electrons and a composition of elements ionized to multiple charge states.

In high temperature environments the ionization is dominated by collisions in the gas. Near high intensity radiation sources the photo-ionization dominates. Recombination reactions inside this plasmas create energetic photons in the X-ray spectrum of the stars which are traceable [ABG+01, Gu02, NKB+03] by orbital X-ray telescopes, as the Chandra (NASA) or the XMM-Newton (ESA) satellites. The nuclear fusion chain in stars towards the end of their lifetime varies, depending mainly on the mass

of the star. The composition of the first stars in the universe was dominated by the primordial elements, hydrogen, helium and traces of lithium. All other elements were produced during the life cycle of these stars and later generations contain the *ashes* of their precursor. So the composition of the ionized gas reflects the evolution of the stellar neighborhood of the gas cloud from which a star developed. Modeling of the plasmas requires absolute measurements of the reaction rates and allows to determine the composition and subsequently learn about the evolution of the plasma and its neighborhood.

In the field of fusion reactors multiply charged ions play a crucial role. The confining walls in Tokamak vessels are exposed to heavy bombardment with high energetic particles. These impacts causes displacement in the sheet lattice. Simulations of the ion radiation load in the ITER fusion reactor estimate approximately 5 displacements per atom per MWa/m$^2$. The structural integrity is strained during the lifetime of the wall sheets. The emission of X-ray photons by excited multiply charged ions allows a confined plasma to dissipate energy, thus, This reduces its temperature and reduces the radiation load on the wall blankets. The envisaged operation of the ITER reactor in *high confinement mode* requires application of localized plasma cooling close to the walls of the vacuum vessel. Moreover, X-ray line profiles are used for electron- and ion-temperature diagnostics in high temperature plasmas [WBD$^+$95].

Laboratory studies allow quantitative understanding of the involved processes in a well-controlled fashion. Various experimental methods are applicable to study these systems. The energy of photons in the visible range is too low for most transitions among the lower levels of highly charged ions, although within a certain range methods have been shown to compensate this by relativistic ion beams which are exposed to blue-shifted photons. Radiative spectroscopy on multicharged heavy ions therefore demands sources for high-energy photons. These are not available for all energy ranges, the soft X-ray regime is just coming into reach by modern synchrotron radiation sources (e.g. ALS) or free-electron lasers (FLASH at DESY, Hamburg). The spectrum of synchrotron sources is not continuous and has to be mangled by lossy monochromators to achieve the required narrow bandwidth. A promising approach is based on the principle of self-amplified stimulated emission (SASE) which is currently subject to investigation of the beam dynamics at the FLASH site. This will boost the brilliance of the emitted photon beam. The limitations of radiative experimental methods are, however, the availability of tunable high-intensity high-energy light sources. Moreover, the fundamental limit of optical selection rules restricts these methods to dipole-allowed transitions only.

Electron beam ion trap (EBIT) setups [LMB$^+$89, CDMU99] have drawn a lot of attention lately, as they are able to breed heavy ions in highest charge states, up to hydrogenic and bare Uranium [KBC$^+$95,MEK94]. A high density electron beam is shot axially through a Penning trap. The high magnetic field (typ. $3 - 8$ T) compresses the electron beam to $\approx 50$ $\mu$m. The space charge potential ($\Delta V \approx 100$ eV) formed by the dense electron distribution ($n_e \approx 10^{13}/\mathrm{cm}^3$) is attractive to positively charged ions which will accumulate in the center of the electron cloud. The electrons collisionally

ionize the stored ions and breed higher charge states. High-energetic photons stem from collisional excitation and recombination processes of the electron beam with the trapped ions and are traceable by X-ray sensitive detectors mounted outside of the trap. The performance of EBITs reduces towards low energies, as the electron beam parameters are continuously degrading.

A powerful method for studies electron-ion reactions has become available by the development of cooler storage rings, which can store molecular or atomic ions for several seconds up to minutes. The ion beam is prepared and fed into the storage ring by ion beam accelerators. Cooling methods are applied to reduce the spatial and velocity spread of the ion beam. The most common methods being electron cooling, laser cooling or stochastic cooling. Laser cooling methods require the setup being tuned to an ion-specific wavelength. Stochastic cooling works best at relativistic energies. Electron cooling is applicable to all ion types and at all energies and can be implemented by one dedicated device. A collinearly merged monoenergetic electron beam is used for cooling of the ion beam at matched velocities, or as probes in electron collision experiments at variable energy relative to the ion beam. Well controlled conditions allow to reduce the spatial and velocity spread and counteract intrinsic heating mechanism of stored ion beams.

## 2.2 Reaction channels of electrons and ions

Electrons and the electronic shell of ions can interact in many ways. Next to ionization by electron impact, the dominant reactions with the electronic shell of the ion are by non-resonant radiative recombination (RR) or by resonant dielectronic recombination. Trielectronic recombination was observed [Sch03] in Be-like systems. Even higher orders of multielectronic recombination are discussed in theory [GS03].

Molecular ions show additional degrees of freedom for vibrationally and rotationally excited states. The captured electron reshapes the molecular potential curves into repulsive configuration and dissociation of the molecule is observed (dissociative recombination).

### 2.2.1 Radiative recombination

The radiative recombination (RR) is a non-resonant capture of an electron into an ion at simultaneous photon emission.

$$e^- + X^{q+} \Rightarrow X^{(q-1)+} + \hbar\omega. \tag{2.1}$$

where the photon carries away the liberated energy, $\hbar\omega = E_{\mathrm{rel}} + E_n$, with is the collision energy of the electron $E_{\mathrm{rel}}$, and the binding energy $E_n$ of the formed Rydberg state $n$. For bare ions this process has been described by [BS57]. The capture cross-section into a state with main quantum number $n$ is calculated semi-classically by [BS57]

$$\sigma_{\mathrm{RR}}(n, E_{\mathrm{rel}}) = \sigma_0 Z^2 \frac{Ry}{E_{\mathrm{rel}}} \frac{E_n}{E_n + E_{\mathrm{rel}}} \tag{2.2}$$

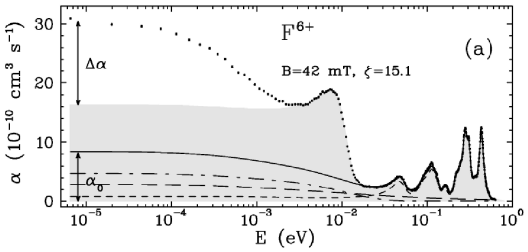


**Fig. 2.1:** *Electron-ion recombination reactions at electron cooler devices in ion storage rings show an excess rate $\Delta\alpha$ at small relative energy in lithiumlike $F^{6+}$ [GH+00] and others. The shaded areas in the figure indicate the expected recombination rate from RR+DR theory.*

with the nuclear charge $Z$, the electron's relative energy $E_{\mathrm{rel}}$, the binding energy of the final state $E_n = Ry\ q^2/n$, and the Rydberg constant $Ry = 13.606$ eV. Moreover,

$$\sigma_0 = \frac{32\pi}{3\sqrt{3}}\alpha^3 r_B^2 = 2.1 \cdot 10^{-22}\ \mathrm{cm}^2, \tag{2.3}$$

with the fine-structure constant $\alpha \approx 1/137$, and the Bohr radius $r_B$.

RR in not completely ionized ions can be calculated by considering the screening of the nucleus by the residual electrons and replacing the nuclear charge $Z$ by an effective charge $q_{\mathrm{eff}}$. The maximum capture rate is observable at low relative energies, and is infinite at zero relative energy, $\sigma_{\mathrm{RR}} \propto 1/E_{\mathrm{rel}}$. However in reality it is limited by the finite electron temperature.

Early recombination experiments reported enhancement of the RR rate at small relative energies for $Au^{50+}$ [U+97b] or $Pb^{53+}$ [B+95] by several orders of magnitude. While it is not clear whether these excess rates are not caused by unknown DR resonances, a pronounced enhancement was shown even for RR in naked ions, that cannot show DR features [U+97a, GH+00].

The experimental analysis performed in [GH+00] show a clear dependence on the magnetic guiding field in the electron beam apparatus and the electron beam parameters, while no dependence on the electron density was evident.

This lead to vivid theoretical speculations on the origin of the enhancement effects. Proposed effects were three-body recombination [GSZ+97], density enhancement by plasma screening [ST00], or increased cross-section due to the chaotic dynamics in the magnetic field of an electron cooler [HYTB03]. However, these models failed to describe quantitatively the experimental observations.

A promising approach has been presented recently [HYW+05]. This model proposes a distortion of the ion's Coulomb potential by induced time-dependent electric field in the merging and demerging toroidal fields of the electron coolers.

### 2.2.2 Dielectronic recombination

At collision energies below the threshold for excitation or ionization by electron scattering a different mechanism is available. In a binary Coulomb interaction the initially free electron approaches the Coulomb potential of the ionic core (Fig. 2.2(a)). Its released kinetic energy is transferred onto a bound electron and thereby ending up itself in a bound state. The ionic charge state is reduced by one and the shell is doubly

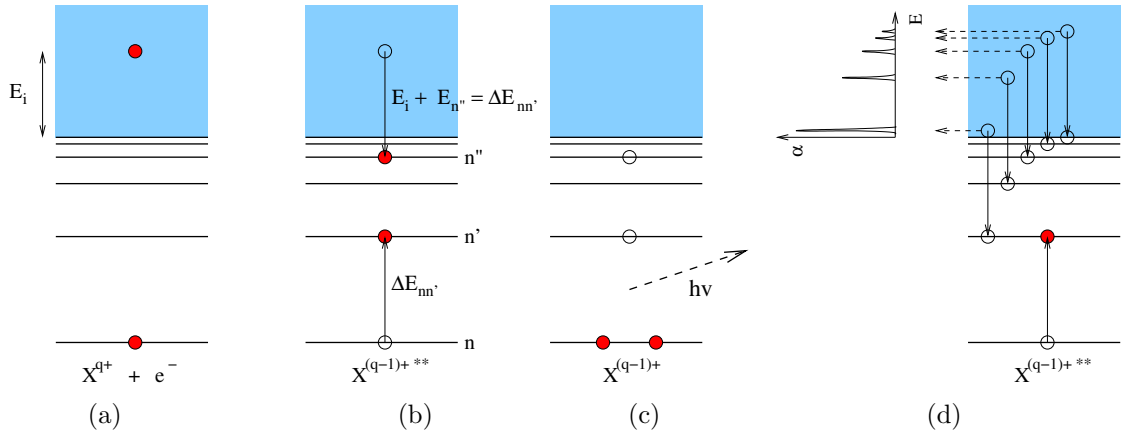


**Fig. 2.2:** *Principle of the dielectronic recombination process*

excited. (Fig. 2.2(b)). This state is unstable against auto-ionization, by reversal of the capture process. With a certain probability it may however stabilize by photon emission (Fig. 2.2(c)):

$$e^- + X^{q+} \rightarrow \left(X^{(q-1)+}\right)^{**} \rightarrow \left(X^{(q-1)+}\right)^{*} + h\nu. \tag{2.4}$$

This is a resonant process and time-inverse to the Augerprocess. Depending on the collision energy many different states might be populated, forming a Rydberg series of resonances (Fig. 2.2(d)) which have the same excited core.

The dielectronic capture rate $A_{dc}(i \rightarrow d)$ from the initial state $i$ to the doubly excited state $d$ can be expressed by the auto-ionization rate $A_a(d \rightarrow i)$ following the principle of detailed balance. The averaged cross-section for a resonance with energy $E_r$ is calculated for the interval $\Delta E$ as [KHS+92]:

$$\bar{\sigma}_{\mathrm{DR}}(E_r)\Delta E = \frac{\pi^2\hbar^3}{m_e}\frac{g_d}{2g_i}\frac{1}{E_r}A_{\mathrm{DR}} \tag{2.5}$$

with the statistical weight ratio $\frac{g_d}{2g_i}$ of the initial state $i$ and the intermediate state $d$, and the rate $A_{\mathrm{DR}}$

$$A_{\mathrm{DR}} = A_a(d \rightarrow i) \cdot \frac{\sum_f A_r(d \rightarrow f)}{\sum_{i'} A_a(d \rightarrow i') + \sum_{f'} A_r(d \rightarrow f')}. \tag{2.6}$$

## 2.3 High resolution electron-ion collision experiments

### 2.3.1 Merged beam kinematics

The electron coolers in storage rings overlay a collinear electron beam on top of the ion beam. Such merged beams feature special kinematics, which allow highest resolution at small relative energies.

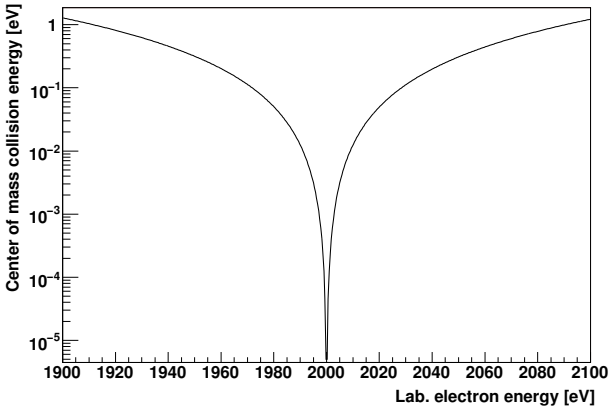


**Fig. 2.3:** *Electron-ion collision energy in the center of mass frame (2.7) at* $E_{\mathrm{cool}} = 2000$ eV. *At small detuning energies one finds highest sensitivity.*

In a Galileo transformation the relative velocity of an electron beam collinear with the ion beam is

$$\begin{aligned} v_{\mathrm{rel}} &= v_{\mathrm{e}} - v_{\mathrm{ion}} \\ \sqrt{\frac{2E_{\mathrm{rel}}}{\mu}} = |v_{\mathrm{rel}}| &= \sqrt{\frac{2E_{\mathrm{ion}}}{m_{\mathrm{ion}}}} - \sqrt{\frac{2E_{\mathrm{e}}}{m_{\mathrm{e}}}} \end{aligned}$$

With the electron's reduced mass $\mu$ and $m_{\mathrm{e}} \ll m_{\mathrm{ion}}$

$$\mu = \frac{m_{\mathrm{e}} m_{\mathrm{ion}}}{m_{\mathrm{e}} + m_{\mathrm{ion}}} \approx m_{\mathrm{e}}$$

one obtains

$$E_{\mathrm{rel}} \approx \left( \sqrt{E_{\mathrm{e}}} - \sqrt{\frac{m_{\mathrm{e}}}{m_{\mathrm{ion}}} E_{\mathrm{ion}}} \right)^2 . \tag{2.7}$$

$\frac{m_{\mathrm{e}}}{m_{\mathrm{ion}}} E_{\mathrm{ion}} = E_{\mathrm{cool}}$ corresponds to the electron's kinetic energy when matched to the velocity of the ion beam.

(2.7) is a non-relativistic expression and a useful relation for estimations at small energies ($\gamma \approx 1$). The relativistically correct is the term, used by the data reduction routines is [KSS+04]

$$E_{\mathrm{rel}} = m_{\mathrm{ion}} c^2 (1 + M) \left[ \sqrt{1 + 2M(1 + M)^{-2}(G - 1)} - 1 \right], \tag{2.8}$$

with the electron-ion mass-ratio $M = m_{\mathrm{e}}/m_{\mathrm{ion}}$,

$$G = \gamma_{\mathrm{ion}} \gamma_{\mathrm{e}} - \cos\theta \sqrt{(\gamma_{\mathrm{ion}}^2 - 1)(\gamma_{\mathrm{e}}^2 - 1)},$$

and the laboratory angle $\theta$ between the two beams.

Relation (2.7) shows highest sensitivity at small detuning energies (Fig. 2.3). With reasonably precise determination of the laboratory energy one is able to achieve highest resolution for small relative energies down to the meV range.

### 2.3.2 Rydberg resonances for precision atomic structure studies

Low-lying DR resonances are interesting candidates for precise spectroscopy of the ionic core. The binding energy $E_n$ of an electron captured into a high Rydberg state can be calculated with small uncertainty for large $n$. In sum with the precisely determined relative energy (see section 2.3.1) this corresponds to the excitation energy of the ionic core (see also Fig. 2.4)

$$E(2\mathrm{s} - 2\mathrm{p}_j) = E_n + E_{\mathrm{rel}}. \tag{2.9}$$

In lithium-like systems this opens a window for precise spectroscopy of 2s – 2p transitions. This method has been first employed in Lithium-like $F^{6+}$ [TEG+02], and was later applied to $Na^{8+}$ [NLK+04] and $Sc^{18+}$ [KSS+04].

The measurement of $Sc^{18+}$ gave an absolute error of 1.9 meV on the $2s–2p_{3/2}$ transition energy of 44.3107 eV. The dominant limiting uncertainty was the ion beam energy dragging due to the detuned electron beam have been serious limitations to the achievable precision. Using independent electron beams for cooling and for spectroscopy eliminates this limit and gives static ion beam conditions. Especially for low-density spectroscopic beams, the influence of the additional cooling force can be eliminated.

$^{45}Sc$ is an isotope with nuclear spin ($I = 1/2$). The 2s electron ($j = 1/2$) is oriented parallel or anti-parallel to the nuclear moment ($F = 4$ or $F = 3$ respectively) and hyperfine splitting is present. The magnetic moment of this isotope has been known with sufficiently small uncertainty for several decades [SW50, SG78]. [SST97, BI00] calculate a 2s ground state hyperfine splitting of approximately 6.1 meV. The hyperfine splitting of the isolated resonance at 68 meV [KSS+04] is expected to be resolvable by the ultracold electron beam from a photocathode ($k_B T_\perp = 0.5$ meV, $k_B T_\parallel = 20$ $\mu$eV [OSL+05]) at the electron target.

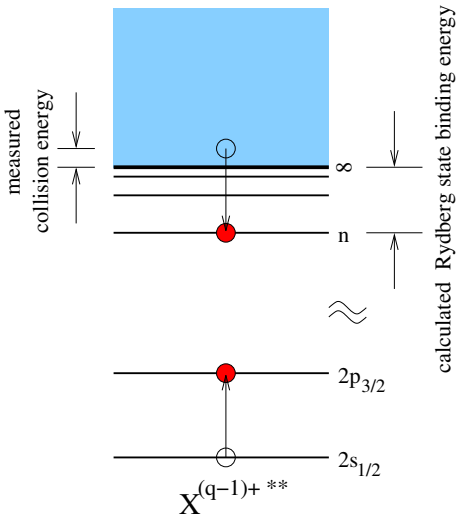


**Fig. 2.4:** *Core excitation energies are accessible by means of dielectronic recombination. The kinematics of merged beams allows highest resolution at small relative energies. The binding energy of the formed high-n Rydberg state can be calculated with small uncertainties.*

### 2.3.3 High-lying doubly excited resonances

Although EBIT experiments have been proven to be extremely suitable for highly charged ions, the limitation of this technique is the reduced resolution due to the high electron beam and ion ensemble temperatures. Furthermore, the trap ion cloud often is a composition of ions in various charge states. The applicability of EBIT-type experiments to intermediate charge states, as they occur in astrophysical plasmas, has to be shown yet.

The superior quality of the electron beam and the possibility of pure ion beams with well-defined charge state is an interesting opportunity for experiments at the TSR. Such experiments were performed for a long time at the *old* setup with one electron beam only. However, with the development of the electron target the reach into higher relative energies turned out to be problematic. The physical reasons and technical solutions for these problems are addressed in this work. A very simple atomic ion, hydrogen-like $Mg^{11+}$ has been chosen as a benchmark system for detection of high energetic resonances at $\Delta E_{\mathrm{c.m.}} \geq 1000$ eV. Theoretical calculations [Fri05] are compared.

## 2.4 Magnetically guided beams

### 2.4.1 Basic definitions

It is useful to define a few practical quantities for description of an electron beam plasma. Wherever useful indices denoting the parallel ($\parallel$) or perpendicular ($\perp$) direction relative to the general beam motion will be used.

The electron density $n_e$ of a homogeneous electron beam is

$$n_e = \frac{I}{e\xi\pi r_{\mathrm{cath}}^2 \beta\gamma}. \tag{2.10}$$

with expansion ratio $\xi = B_{\mathrm{gun}}/B_{\mathrm{guide}}$ and the relativistic parameters $\gamma = (E_{\mathrm{rel}}+E_0)/E_0$ and $\beta = \sqrt{1-1/\gamma^2}$. The mean inter-electron distance $d$ is connected to the density via

$$d = n_e^{-1/3}. \tag{2.11}$$

The close arrangement of electrons leads to a deviation from the Coulomb potential. However, this is small on scales below the *Debye length*

$$\lambda_d = \sqrt{\frac{k_B T}{m}}\omega_{\mathrm{pl}}^{-1}. \tag{2.12}$$

An important relation is the *thermal distance of closest approach*,

$$b = \frac{q^2}{4\pi\epsilon_0}(k_B T)^{-1} \tag{2.13}$$

which is the distance at which the Coulomb repulsion equals to the thermal energy $k_B T$. It can be given for the transverse and longitudinal energy spreads of the electrons and will by denoted as $b_\perp$ and $b_\parallel$ respectively in the following.

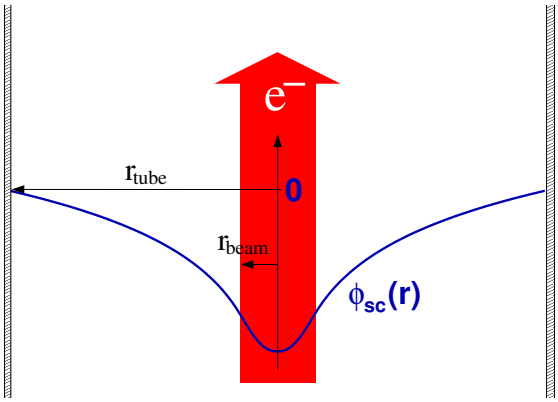


**Fig. 2.5:** *The repulsive Coulomb force between the electrons creates a space charge potential $\Phi_{\mathrm{sc}}(r)$. For a cylindrical beam of homogeneous density in a cylindrical beam tube the radial dependence of the space charge potential is given by equation (2.18)*

An electron beam is a one-component plasma of particles coupled to each other by the Coulomb force. This plasma reacts onto distortions from the equilibrium on a timescale given by the plasma frequency

$$\omega_{\mathrm{pl}} = \sqrt{\frac{e^2 n_e}{m_e \epsilon_0}}. \tag{2.14}$$

The cyclotron frequency of a charge $q$ with mass $m$ in a magnetic field of strength $B$ is

$$\omega_{\mathrm{cycl}} = \frac{q}{m} B. \tag{2.15}$$

The charged particles are forced onto a circular motion with radius

$$r_{\mathrm{cycl}} = \frac{m v_{\perp}}{qB}. \tag{2.16}$$

A typical order of magnitude for the cyclotron radius $r_{\mathrm{cycl}}$ is a few $\mu$m.

### 2.4.2 Space charge

The repulsive Coulomb force between the electrons in the beam creates a space charge potential $\Phi_{\mathrm{sc}}(r, n_e)$. An electron approaching the beam is screened by this potential, lowering its kinetic energy.

$$E_{\mathrm{e}} = eU_0 - e\Phi_{\mathrm{sc}}(r, n_e) \tag{2.17}$$

For a cylindrical electron beam with homogeneous density profile in a cylindrical beam tube one finds:

$$\Phi_{\mathrm{sc}}(r, n_e) = \frac{n_e e r_{\mathrm{beam}}^2}{4\epsilon_0} \begin{cases} 1 - \frac{r}{r_{\mathrm{beam}}} + 2\ln\frac{r_{\mathrm{tube}}}{r_{\mathrm{beam}}} & r < r_{\mathrm{beam}} \\ 2\ln\frac{r_{\mathrm{tube}}}{r} & r_{\mathrm{beam}} > r > r_{\mathrm{tube}} \end{cases} \tag{2.18}$$

Since the space charge potential depends on the electron density (2.10), and the density again depends via (2.17) on the space charge correction, both quantities have to be obtained in an iterative way.

The space charge of the beam is directed outwards and would lead to a quick blowing up of the charge cloud. To suppress the blow-up a magnetic field is applied.

### 2.4.3 Electron temperatures

In a magnetized electron beam the longitudinal and transverse degree of freedom are mostly decoupled. The electron distribution can be described by an anisotropic flattened double Maxwellian distribution [DAB+94]

$$f(v) = \frac{m_e}{2\pi k_B T_\perp}\left(\frac{m_e}{2\pi k_B T_\parallel}\right)^2 \times \exp\left(-\frac{m_e v_\perp^2}{2k_B T_\perp} - \frac{m_e v_\parallel^2}{2k_B T_\parallel}\right). \tag{2.19}$$

In usual setups the longitudinal degree of freedom is a few orders of magnitude smaller than the transverse. The formation process of the electron beam determines its temperature. The first link in this chain are the initial conditions of the plasma, when the electrons are emitted from the cathode material. In the next stages the electron plasma is shaped by electric and magnetic fields to form the favored beam profile and accelerated to collision energy.

Concepts for reduction of the transverse and longitudinal temperature were discussed early. One way for the reduction of the transverse degree of freedom is the adiabatic transverse expansion and the first device to employ this method was reported by [DAB+94]. The influence of accelerating field gradient on the longitudinal temperature was discussed earlier [DKL+88]. These basic concepts were implemented in the design of the new Heidelberg electron target [Spr03]. A newly developed cryogenic semiconductor photocathode [Wei03, OSL+05] lowers the initial temperature of the emitted of the electron cloud and allows to achieve ultimately low electron velocity spreads.

Electron cooling and electron collision spectroscopy are limited by the temperature of the interacting electron plasma. The role of the electron temperature in these two cases shall be briefly laid out here.

**Electron cooling.** The electrons have an average velocity $\langle v_e \rangle$ and a temperature $k_B T$. Ions with a detuned velocity $v_{\mathrm{Ion}}$ are continuously *kicked* by Coulomb interactions with the electrons until the velocities are matched. This is described by a dissipative cooling force $F_{\mathrm{cool}}$ [Pot90]

$$\vec{F}_{\mathrm{cool}}(u) = \frac{3}{2} c^2 F_0 L_c \frac{u}{|u|^3 + 2\Delta_e^3}\frac{\vec{u}}{|u|}. \tag{2.20}$$

with $u = v_{\mathrm{Ion}} - v_e$ and the mean electron velocity spread $\Delta_e$. The force has a node at $u = 0$, it converges towards 0 for $|u| \to \infty$, but reaches extreme values for $|u| = \Delta_e$ [Pot90]. At small detunings the strength of the $F_{\mathrm{cool}}$ depends on the electron density and temperature. The longitudinal component of the cooling force is shown in Fig. 2.6.

**Spectroscopic resolution.** The production of an electron beam in typical setups yields an anisotropic distribution of the transverse and longitudinal degree of freedom, which are mostly decoupled by the magnetic guiding field and $k_B T_\parallel \ll k_B T_\perp$. In

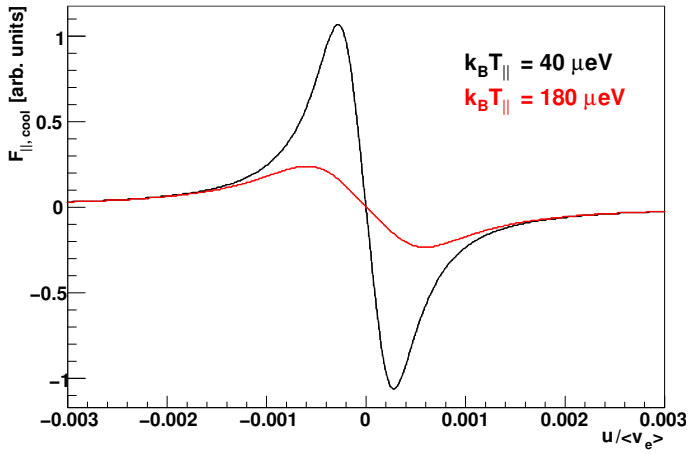


**Fig. 2.6:** *The cooling force (2.20) depends on the electron temperature. Black curve:* $k_B T_\parallel = 40$ *μeV; red curve:* $k_B T_\parallel = 180$ *μeV. Colder electrons impose a stronger force at small detunings. Due to* $k_B T_\parallel \ll k_B T_\perp$*, the transverse component of the cooling force is much weaker.*

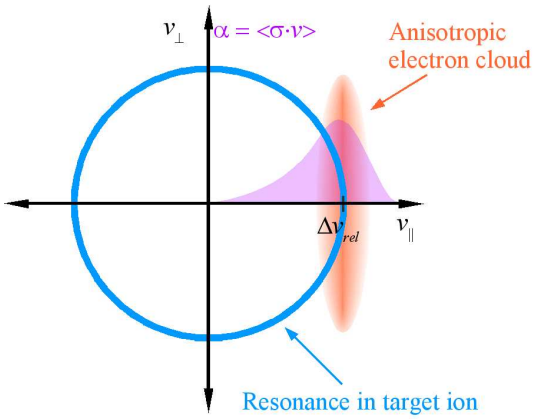


**Fig. 2.7:** *In the velocity frame the anisotropy of the electron distribution forms a "lens"-shape (orange). A* narrow *resonance of a given ion gives a hollow sphere in this frame (blue circle).*
*Tuning the relative energy shifts the electron distribution along the X-axis. Reactions are observed for all energies where the electron distribution overlaps the range of possible recombination vectors. This forms the observed asymmetric line shape with an extended low-energy tail (violet curve).*

a velocity-frame the electron distributions has the shape of a lens. By varying the electron energy this distribution is moved along the longitudinal axis ($v_\parallel$). A narrow ionic resonance, with a negligible natural line width forms a hollow sphere in such a frame. The overlap of both distributions results in the observed asymmetric resonance line shape (see Fig. 2.7)

$$\alpha = \int_0^\infty \sigma(v) v f(v_d, \vec{v}) d^3v = \langle v\sigma \rangle \tag{2.21}$$

of the rate coefficient $\alpha$ as a convolution of the natural width of the line with the flattened double Maxwellian electron distribution $f(v)$.

From the resonance shape one can estimate the transverse and longitudinal temperature. The shape of a resonance's high-energetic flank is determined by the longitudinal temperature and with the extrapolation to zero transverse temperature one gets the longitudinal spreading by

$$\Delta E_{\mathrm{hi}} = \sqrt{16 k_B T_\parallel E \ln 2}, \tag{2.22}$$

similarly the transverse spreading can be deduced from the low-energetic side

$$\Delta E_{\mathrm{lo}} = k_B T_\perp \ln 2. \tag{2.23}$$

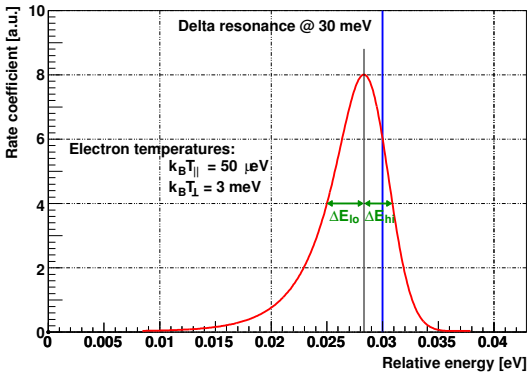


**Fig. 2.8:** *Convolution of a cross-section of a δ-resonance at 30 meV resonance energy with an electron distribution with* $k_B T_{\parallel} = 50$ μeV *and* $k_B T_{\perp} = 3$ meV. *One finds an asymmetric line shape with a broadened low-energy flank and a shifting of the rate coefficient maximum from the resonance position towards a lower energy.*

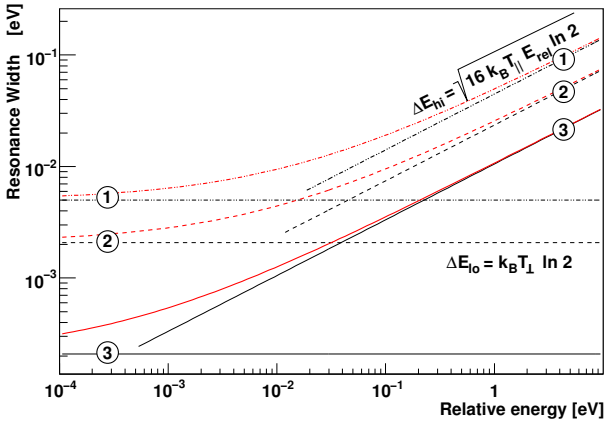


**Fig. 2.9:** *Resonance width vs. collision energy.* ① *electron cooler (*$k_B T_{\perp} = 7.2$ meV, $k_B T_{\parallel} = 180$ μeV, *[KSS+04])* ② *estimated electron target with thermionic cathode (*$k_B T_{\perp} = 3$ meV, $k_B T_{\parallel} = 80$ μeV*)* ③ *anticipated electron target with cryogenic photocathode (*$k_B T_{\perp} = 0.3$ meV, $k_B T_{\parallel} = 20$ μeV*) The red curve is the total width as a sum of the transverse and the longitudinal contributions, respectively.*

The total peak width is given by the sum of both,

$$\Delta E = \Delta E_{hi} + \Delta E_{lo}. \tag{2.24}$$

It is obvious that the peak width is a function of the resonance energy $E_{\mathrm{rel}}$ (see Fig. 2.9). At low relative energies it is dominated by the transverse temperature, which contributes a constant broadening. Towards higher energies the contribution of the longitudinal temperature dominates.

It is also important to point out, that the transverse spread shifts the maximum of the $\alpha$ distribution towards slightly lower energies, so that it does not coincide with the cross-section maximum. So one has to know the true transverse temperature of the electrons rather precise to derive the correct resonance energy. While this downwards-shift is true for the whole energy range, it is most pronounced at low-energetic resonances. At higher-energetic resonances other effects dominate the uncertainty of the resonance energy.

The development of a new type of electron source [Wei03], using a negative electron affinity (NEA) [Sv65] cryogenic GaAs semiconductor provides electron beams of unprecedentedly low energy spread. Usage of this cathode type at the electron target will allow unprecedentedly high resolution in electron collision spectroscopy.

The influences of heating mechanisms on the electron beam temperature , denoted as transverse-longitudinal (TLR) and longitudinal-longitudinal relaxation (LLR) will be discussed below.

### 2.4.4 Electron sources

Generally two different types of electron emitters are available, which form the beams by either thermionic or photo-emission.

#### Thermionic electron emitters

Electrons in the conduction band of a metallic lattice are a degenerate Fermi gas. The temperature of the solid is mostly determined by the temperature of the bound electron plasma.

An electron at the surface has to overcome the binding energy to be emitted. The binding energy is a material specific constant and is typically in the range of few eV. By heating the solid emitter material a fraction of the Fermi tail populates the energetic regime above the work function threshold. These electrons can diffuse towards the surface and be emitted. The advantage of thermionic electron sources is that they can yield very high electron currents. A drawback is the high temperature of the emitted electrons.

#### Photo emitters

A very different approach is used in photo-emitters. The semiconductor GaAs is known to have a state of negative electron affinity (NEA) [Sv65] for the valence band. Electrons near the surface are excited by laser illumination into the valence band and diffuse to the surface, where they are emitted into vacuum. Since the necessary energy for the emission is provided by a laser no heating of the emitter material is needed. Cooling with liquid nitrogen even decreases the temperature further to $\approx 100$ K.

The cold cathodes make ultracold electron beams feasible. However, the short lifetime of a running cathode sample of typically 15 hours, and the low electron yield impose limitations on their use.

The Heidelberg electron target has been designed to apply both types of electron sources. Successfully performed experiments will be laid out in detail in Chapter 5.

### 2.4.5 Transverse temperature

Transferring an electron beam from a region of high magnetic field into a region of low magnetic field leads to a blow-up of the electron beam and to transverse expansion. The transverse temperature $k_B T_\perp$ depends on this expansion ratio,

$$k_B T_\perp = \frac{k_B T_{\text{cath}}}{\xi} \tag{2.25}$$

with $\xi = B_{\text{c}}/B_{\text{guide}}$ being the ratio of the magnetic field at the gun region and the final field (Fig. 2.10). The first successful demonstration of adiabatic transverse expansion has been shown in [DAB+94] and has been adopted by many electron beam devices in storage rings since then.

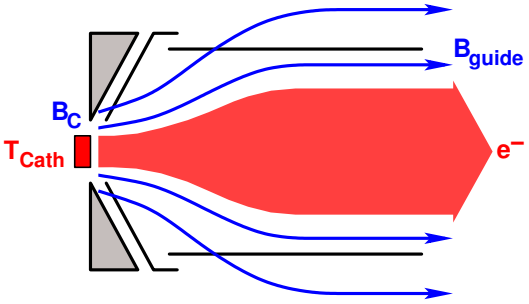


**Fig. 2.10:** *A magnetized electron beam passing from a region with a high magnetic field into a low field region experience transverse expansion.*

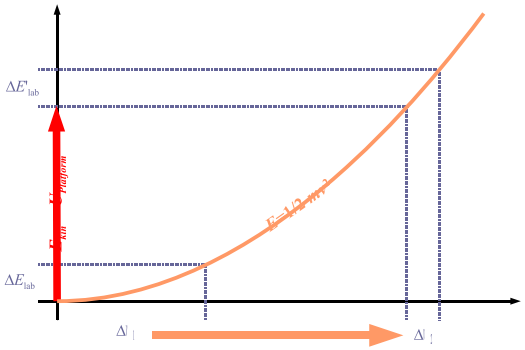

**Fig. 2.11:** *Kinematic transformation of the longitudinal temperature of accelerated electron beams reduces the velocity spread. In the restframe of the electrons the reduced velocity spread leads to a decrease of the longitudinal energy spread.*

### 2.4.6 Longitudinal temperature

The longitudinal temperature is dominantly the result of kinematic transformation. The acceleration of electrons does not change the energy spread of the distribution. But, due to the square dependence of the kinetic energy on the velocity, at high kinetic energies the velocity spread is reduced (see Fig. 2.11). In a co-moving frame the energy distribution can be given by [DKL+88]

$$k_B T_{\parallel}^{\mathrm{kin}} = \frac{(k_B T_{\mathrm{cath}})^2}{2E}, \tag{2.26}$$

with the final kinetic energy $E = eU$ of the accelerated electron beam. Already for low final electron energies the kinematic contribution is vanishingly small and in the range of a few $\mu$eV.

The longitudinal temperatures which were reported in experiments were however much higher (typ. $\approx 180$ $\mu$eV). And two heating effects are used to explain the discrepancy, transverse-longitudinal-relaxation and longitudinal-longitudinal-relaxation. They will be explained in the following sections and contribute to the final longitudinal temperature by

$$k_B T_{\parallel} = k_B T_{\parallel}^{\mathrm{kin}} + \frac{\partial \Delta E_{\mathrm{TLR}}}{\partial x} dx + \Delta E_{\mathrm{LLR}}. \tag{2.27}$$

### 2.4.7 Transverse-longitudinal-relaxation (TLR)

In typical beam operations a strong anisotropy of the transverse and the longitudinal electron temperature is observed, where the longitudinal temperature is typically of the order of $k_B T_{\parallel} \approx 50$ $\mu$eV and the transverse temperature about $k_B T_{\perp} \approx 5$ meV or

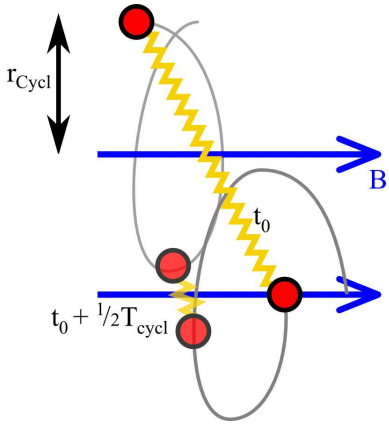


**Fig. 2.12:** *The inter-electron distance of two nearby electrons varies due to the cyclotron motion and constantly approach and depart from each other on the phase of the cyclotron motion. This creates an oscillation of the repulsive inter-electron Coulomb force. The temperature anisotropy of the longitudinal and transverse degrees of freedom leads couple by the repulsive Coulomb force and energy is transferred. This leads to a increase of the longitudinal temperature.*

$k_B T_\perp \approx 100 \times k_B T_\parallel$. The magnetization suppresses energy transfer between the two degrees of freedom to some extend, however not completely. In a simple picture two close-by electrons with different phases in their cyclotron motion continuously approach and depart from each other (see Fig. 2.12). The changing repulsive Coulomb potential in such a situation leads to an energy transfer. Since the transverse degree of freedom is frozen by the magnetic field, the energy relaxes into the longitudinal degree of freedom.

Quantitative descriptions for these processes were presented by [DKL+88], giving an empirical formula,

$$\left(\frac{dT_\parallel}{dz}\right)^{\mathrm{ad}} = \left(\frac{dT_\parallel}{dz}\right)^{0} C_1 \exp\left(-\frac{C_2}{r_c\left(n_e^{1/3} + \frac{C_3}{b_\parallel}\right)}\right) \tag{2.28}$$

with the thermal distance of closest approach $b_\parallel$ (equation 2.13) assigned to the longitudinal temperature $k_B T_\parallel$, and

$$\left(\frac{dT_\parallel}{dz}\right)^{0} = \frac{\pi e^4 n_e}{(4\pi\epsilon_0)^2 k_B \sqrt{E_{\mathrm{kin}} k_B T_\perp}}. \tag{2.29}$$

The parameters $C_1$, $C_2$ and $C_3$ are empirically derived and different values have been reported by [Ale90], [DKL+88] and [Kra92].

In a Plasma theory description [OH85] one obtains a slightly different formula:

$$\left(\frac{dT_\parallel}{dz}\right) = \frac{4e^4 n_e}{(4\pi\epsilon_0)^2 k_{\mathrm{B}} \sqrt{E_{\mathrm{kin}} k_B T_\perp}} \ln\frac{r_c}{2b_\perp} \exp\left[-2.3\left(\frac{b_\parallel}{r_c}\right)\right] \tag{2.30}$$

### 2.4.8 Longitudinal-longitudinal-relaxation (LLR)

A different heating mechanism stems from the acceleration of the electron beam towards collision energy. The governing timescale for intrinsic rearrangements inside the electron beam is given by the plasma frequency $\omega_{\mathrm{plasma}}$. Thermal jittering of the electrons continuously rearranges the plasma. An acceleration of the plasma enhances results in a decrease of the electron density $n_e$, and therefore the mean inter-electron distance $d$ (equation 2.11). If this acceleration happens fast relative to the plasma

frequency, the thermal oscillations are quasi frozen out. The stretching of the relative distance $d$ during the acceleration proportionally also amplifies the jitter amplitude. The resulting disequilibrium situation of the electron plasma after acceleration leads to relaxation of the inter-electron Coulomb potential which succeedingly heats the plasma.

The LLR contribution is estimated by [DKL+88]:

$$\Delta E_{\mathrm{LLR}} = C \cdot \frac{e^2}{4\pi\epsilon_0} n_e^{1/3}, \tag{2.31}$$

with the parameter $C$ describing the adiabaticity of the acceleration process. This formula describes the LLR heating as an fractional contribution of the inter-electron Coulomb potential. For fast acceleration [DKL+88] has calculated $C = 1.9$ For slower acceleration the electron positions can continuously adjust to the changing plasma conditions and thus $C$ is expected to get down to values of the order of 0.4.

The electron target setup [Spr03] implements such a slow acceleration by shaping the gradient of the accelerating field in multiple small steps over a distance of 1.4 m (see Fig. 2.13). The electron beam emerges from the cathode and is passed into the drift region for magnetic expansion. The length of this region [1] is $L_{\mathrm{D}} = 0.21$ m and the electron energy in this region is $E_{\mathrm{Drift}} = e(U_0 - U_{\mathrm{Drift}})$. The region for adiabatic acceleration follows and can be flexibly shaped by ring electrodes surrounding the electron beam. The gap width between two neighboring ring electrodes is 12.5 mm and the arrangement includes 77 ring electrodes in total. The potential structure can include an optional drift region $L_{\mathrm{D+}}$ which retains the electron energy $E_{\mathrm{Drift}}$ for some distance. A field gradient is applied over a distance $L_{\mathrm{grad}}$ to accelerate the electron beam towards their final kinetic energy $E_{\mathrm{kin}} = eU_0$. The electrons pass the remainder of the acceleration section $L_{\mathrm{FE}}$ before they get merged into the TSR on top of the ion beam in the downstream toroid section.

Apart from a generally small observed longitudinal temperature ($\approx 50$ $\mu$m [Spr03]) compared to other setups (TSR electron cooler: $k_B T_{\parallel} \approx 180$ $\mu$eV [KSS+04]) no clear demonstration of the impact of the accelerating field-gradient was available so far.

## 2.5 Storage ring electron collision spectroscopy

In earlier experiments at the TSR the electron cooler has been used both for cooling of the ion beam and as a probe for energy resolved electron collision spectroscopy [KHS+92]. After an initial cooling period the measurement scheme foresaw measurement steps at variable energy interleaved with cooling steps to reestablish the ion beam quality.

A new electron beam device has been constructed and taken into operation in 2003 [Spr03,SLO+04] in the TSR storage ring. With this the TSR is the only heavy ion storage ring worldwide which features two electron beams collinear to the ion beam. This has several beneficial consequences, listed below, as it allows to separate the tasks

[1] A modified drift tube exists with a length $L'_{\mathrm{D}} = 0.285$ m and is installed at high energy experiments.

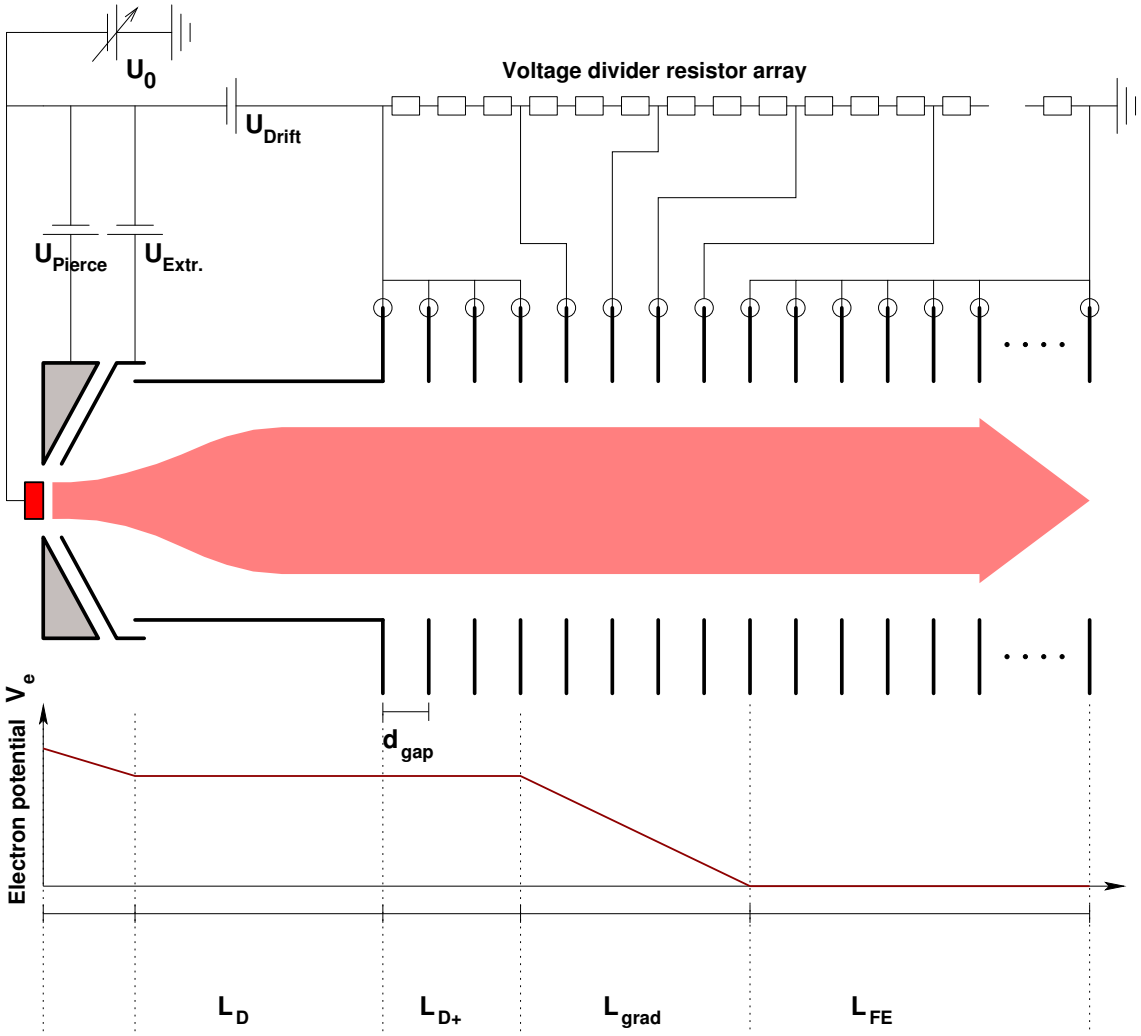


**Fig. 2.13:** *Schematic structure of the beam formation and acceleration section. The cathode is surround by a Pierce electrode. An extraction electrode on attractive potential pulls electrons from the electron cloud in front of the cathode. A succeeding drift tube (length $L_{\mathrm{D}} = 28$ cm) keeps the electron beam at static velocity during the magnetic expansion stage. 77 ring electrodes surrounding the electron beam shape the electrostatic acceleration field to bring the electrons to their final collision energy. The configuration of the accelerating electric field is variable and established by connecting the ring electrodes to a staged voltage divider. It includes an optional drift length $L_{\mathrm{D+}}$, a potential drop from $U_0 - U_{\mathrm{drift}}$ to ground potential on a length $L_{\mathrm{grad}}$ and the remainder of the acceleration section at full energy, $L_{\mathrm{FE}}$.*

of electron cooling and target operation between them, while in previous experiments these tasks were handled alternatingly by one electron beam.

1. The most obvious advantage of the improved new setup is, that the ion beam can now be continuously cooled without interruption. The ion beam velocity spread approaches a minimum value where external and intrinsic heating mechanisms are balanced by the friction in the heat-bath of the cooling electron beam.

2. The presence of two electron beams also allows static conditions, so that transient effects can be eliminated. A detuned electron beam still imposes its friction force onto the nearby ion beam and drags the ion beam energy non-linearly. However, the effect now becomes much smaller and can be further decreased by attenuating the probe beam electron density.

3. Large energy detunings are available by two independent HV platforms. Slew-rate effects are reduced and a bigger dynamic range is available.

4. An improved duty cycle is possible, as interleaved re-cooling steps to reestablish the ion beam quality are no longer needed.

All this results in a large gain of resolution and energy accuracy in the scan of electron collision resonances and makes it possible to perform spectroscopic experiments as described below.

## 2.6 Goals

With the considerations summarized in this chapter one can formulate the following objectives for the present work.

1. Implement an efficient detection and data acquisition system at the TSR for measurement of DR products. This includes the setup of a detector and a versatile data acquisition system,

2. Improve the understanding of the TLR and LLR heating effects on the electron beam temperature and find possible ways for reducing their influence.

3. Analyze the electron beam properties at high energy.

4. Apply the improved energy resolution in electron-ion collision experiments to low-energetic $\Delta n = 0$ dielectronic recombination resonances. A promising system for demonstrating the potential of this type of electron collision spectroscopy is the lithium-like $^{45}Sc^{18+}$, in particular using an electron beam from a cryogenic photocathode.

5. Establish high precision for measurements at high relative energies. DR measurements of hydrogen-like $^{24}Mg^{11+}$ are an ideal test system for measurements of this type.

6. Apply the advantages of the electron target setup to address the radiative recombination puzzle. Lithiumlike $F^{6+}$ is a suitable candidate, its DR resonance structure is well understood and has been used for systematic RR studies previously.

# Chapter 3

# Detection and data acquisition system

## 3.1 Overview of the heavy ion storage ring TSR

The experiments in this work have been performed at the heavy ion storage ring TSR at the Max-Planck-Institute for Nuclear Physics, Heidelberg. The TSR is a magnetic storage ring, its schematic layout is shown in Fig. 3.1. The ring consists of a toroidal vessel with ultrahigh vacuum (UHV, $p \approx 5 \times 10^{-11}$ mbar). The circumference on the ion beam trajectory is approximately 55.4 m. Eight dipole magnets deflect the stored ions by 45° each to form a closed loop. They are arranged pairwise with short straight corner sections and four long straight sections in between. The long straight sections are used for injection and extraction, electron cooling, experiment, and diagnostics. Quadrupole magnets in the straight sections in doublet and triplet configuration implement an alternating gradient strong focusing of the stored ions.

The ion beam revolution frequency may be recorded with a Schottky pickup. The cylindrical pickup electrode surrounds the ion beam axis and records induced random fluctuations in the ion beam. A Fourier-analysis of the signal allows to reconstruct the ion beam's revolution frequency and its spread. The frequency spread corresponds to the momentum spread of the ion beam. For a cooled ion beam one observes a typical frequency spread of $\Delta f/f \approx 10^{-4}$.

Restgas atoms are ionized by the stored ions. A homogeneous transverse electrical field maps them onto position sensitive detectors (resistive anode). The original (thermal) momentum of the restgas atoms when ionized is negligible, so that the impact position on the detector is a projection of the point where they were formed, i.e. the beam of stored ions. A horizontal and a vertical arrangement allows to obtain transverse ion beam profiles in both directions.

The ion beam current is measured by a DC transformer. An alternative ion current measurement is possible by the beam profile monitor. However this is very sensitive to the restgas pressure, which could vary during a measurement.

Two electron beam devices are available, merging a magnetically guided electron beam for a 1.5 m distance collinear to the ion trajectory. They are used for electron

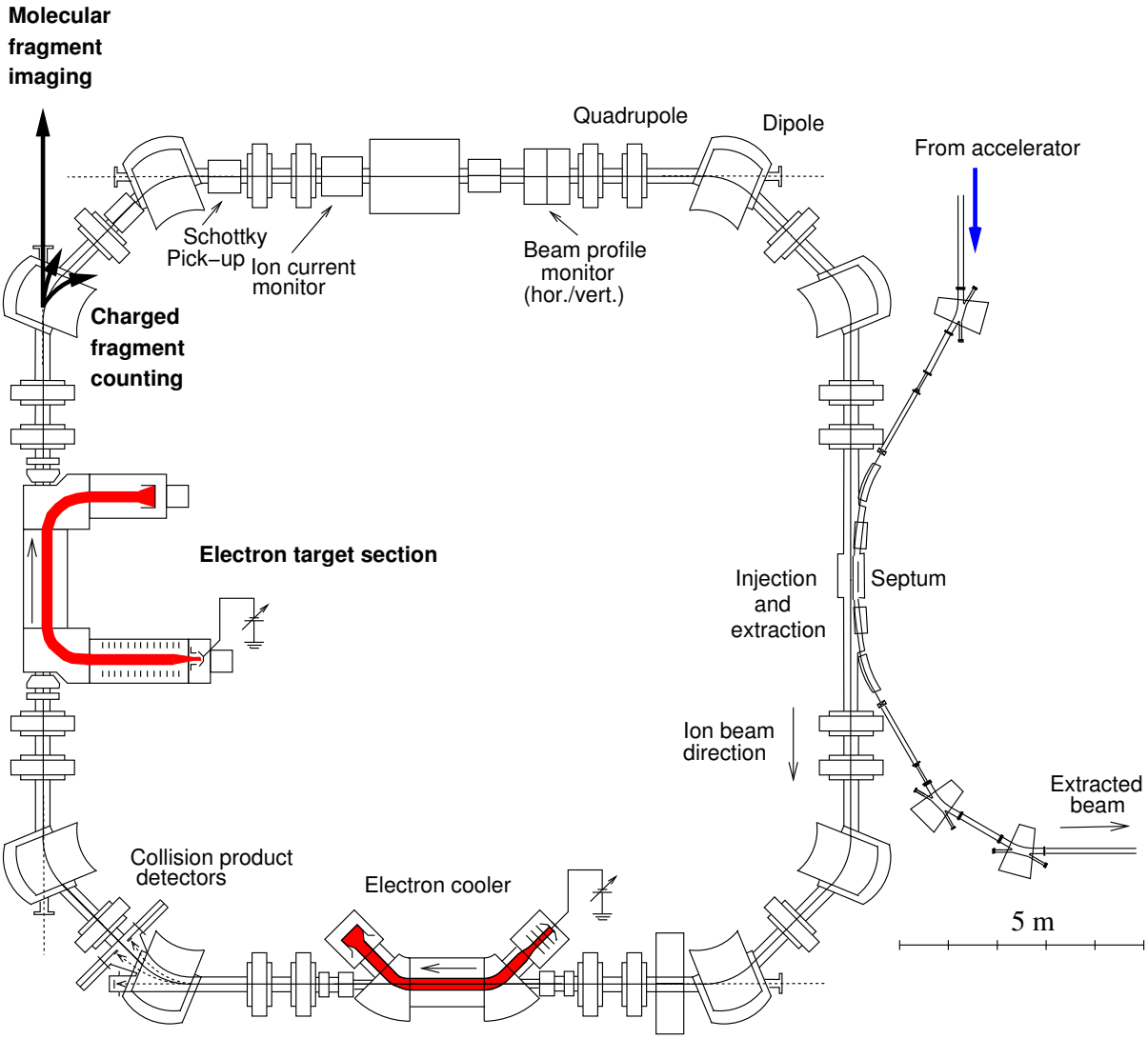


**Fig. 3.1:** *A schematic drawing of the TSR heavy ion storage ring with two electron beam devices, the electron cooler and the electron target. Detectors for charged and neutral fragments are installed downstream of the electron target.*

cooling and as target for collision experiments. The second electron beam device has been installed in 2003 and is used as a dedicated high resolution electron target for recombination experiments. It will be described in detail in Section 4.1. Various detectors are available following the first downstream bending magnet of each electron beam device.

The TSR stores ions with a rigidity $B\rho$ of up to 1.5 Tm [Gri06]. The polarity of the dipole bending magnets may be reversed to allow storage of negative or positive ions. For this work it has been set to storage of positive ions, which is silently assumed through out the remainder of this work.

The two electron beam devices in the TSR are placed in two consecutive straight sections. The previously existing device is usually operated in cooling mode velocity-

matched to the ion beam (and hence referred to as electron cooler in the following). The new electron beam device [Spr03] is operates as collision probe (referred to as electron target subsequently). Using two electron beams allows to eliminate transient energy instabilities, increases the dynamic range and the duty cycle, as has been discussed in section 2.5.

The setup of the electron target will be described in section 4 in detail.

## 3.2 The MIDAS detector

The released amount of energy in electron collision reactions with the atomic or molecular shell $\Delta E \approx$ eV is small compared to the ion beam energy (typ. $E_{\mathrm{kin}}^{ion} \approx 5 \ldots 300$ MeV), so that the product ions mostly retain their original trajectory in the straight section of the TSR. They are separated from their parent ion beam by the next downstream magnetic dipole field which is selective to the $q/m$-ratio,

$$r = \frac{mv}{qB}. \tag{3.1}$$

It is useful to define a quantity $\kappa$ which relates the charge to mass ratio of the product ion to the parent ion,

$$\kappa = \frac{[q_{\mathrm{P}}/m_{\mathrm{P}}]}{[q_{\mathrm{i}}/m_{\mathrm{i}}]}. \tag{3.2}$$

The index P denotes the product fragment, the index i the stored ion beam. The products' bending radius $r_{\mathrm{P}}$ depends on the ion and product species and is a function of $\kappa$,

$$r_{\mathrm{P}}(\kappa) = \frac{r_{\mathrm{i}}}{\kappa}, \tag{3.3}$$

with $r_{\mathrm{i}} = 1.15$ m [Gri06] being the TSR-specific bending radius of the stored ion beam. The detectors need to be moved to the corresponding position of the specific charged product.

Molecular reactions often result in bond-breaking and production of multiple fragments of various masses and charge states. For products from atomic ion species ($m_{\mathrm{P}} = m_{\mathrm{i}} \pm m_e$; $m_e \ll m_{\mathrm{i}}$) the $\kappa < 1$-range corresponds to capture of an electron ($q_{\mathrm{P}} < q_{\mathrm{i}}$), whereas ionized products have $\kappa > 1$ ($q_{\mathrm{P}} > q_{\mathrm{i}}$).

A vacuum chamber has been constructed [Wis02] to give access to various detectors which cover different $\kappa$-ranges:

$$\begin{aligned}
\kappa < 0 \quad &: \quad \text{Negative (molecular) fragments} \\
\kappa = 0 \quad &: \quad \text{Neutral fragments} \\
1/2 \leq \kappa \leq 3/2 \quad &: \quad \text{positive fragments, atomic ion products} \\
3/2 < \kappa \quad &: \quad \text{positive light molecular fragments}
\end{aligned} \tag{3.4}$$

This allows detection of a wide range of product species and reaches beyond the former detector setup downstream to the electron cooler [MHK+96].

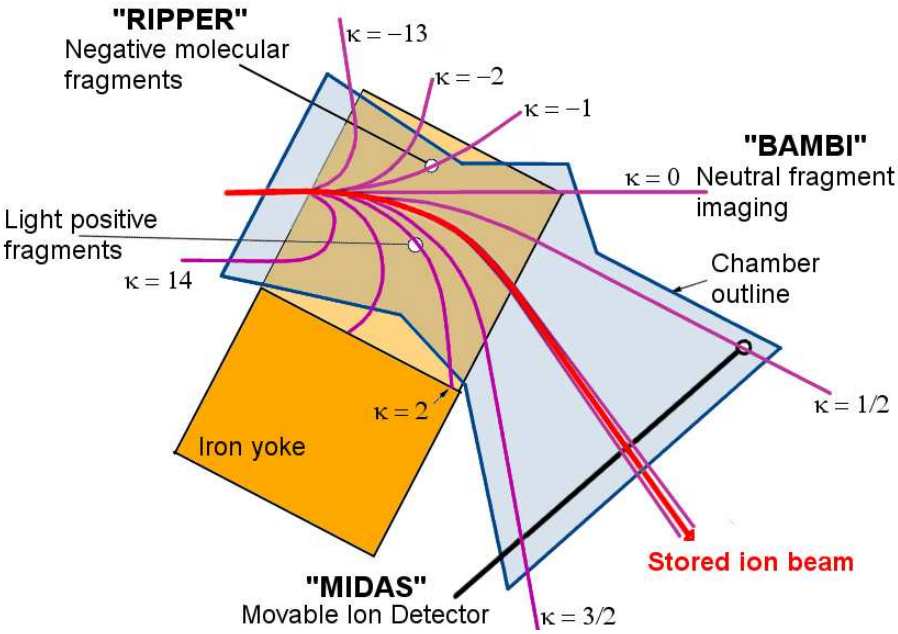


**Fig. 3.2:** *Schematic view from top onto the detector chamber for the dipole downstream of the electron target. The movable ion detector for atomic spectroscopy – MIDAS – can be positioned within the ion product range of* $3/2 \leq \kappa \leq 1/2$.

For detection of negative ion fragments ($\kappa < 0$), stemming mainly from resonant ion pair production in molecules, a new detector setup (RIPPER) is currently being implemented [Hof].

Neutral fragments ($\kappa = 0$) are studied mainly in molecular breakup reactions, like dissociative recombination. A versatile detector setup, *Bambi*, has been installed for neutral fragment counting [Buh06] and three-dimensional fragment imaging [Nov04].

The recombination of an atomic ion with an electron reduces the charge state by one, and one finds $\kappa < 1$. The lowest ionic product is formed in $X^{2+} + e^- \rightarrow X^+$, thus $\kappa \geq 1/2$. Ionization reactions enhance the charge state, thus $\kappa > 1$. The dimensions of the dipole constraints the ionization products which may be detected outside of the dipole yoke. The lowest outside detectable parent charge state is $q = 2+$ forming $q = 3+$ products, thus $\kappa = 3/2$. The $1/2 \leq \kappa \leq 3/2$ range of atomic product ions is covered by the *MIDAS* detector — Movable Ion Detector for Atomic Spectroscopy — and is used for all experiments in this work.

The development for the MIDAS detector was driven by the wish to have single-ion counting with efficiency $\eta = 100$ % for a wide charge-, mass- and energy-range.

The following points were considered [Wis02] for the the design of the detector:

- For atomic ions the impact energy of the detected product does not need to be measured with high precision, as it is the same as the parent ion's kinetic energy. This allows usage of fast scintillation detectors.

- The wide possible $\kappa$ range requires the detector to be movable.

**Fig. 3.3:** *MIDAS detector setup.*

- The detector is exposed to high count rates of up to 500 kHz and needs to be resistive to radiation damage.

- The range of impact energies can vary between a few MeV for light species up to several hundred MeV for highest masses and charge states. Low-Z products with small impact energy are stopped in thin layers of solids, so that any material in front of the detector interferes with the detection efficiency. Therefore the detector is best uncovered and directly exposed to the beam inside of the ultrahigh vacuum of the TSR.

The detector material studies [Wis02] led to the decision for the scintillating crystal material YAP:Ce (Cer-doped Yttrium-Aluminum-Perowskit), which has a high photon yield, fast decay time of 25-30 ns, emits photons at 330 to 380 nm wavelength, [BKM$^+$91], and is non-hygroscopic and thus usable in UHV conditions.

The basic layout of the system was established by [Wis02]. The detector arrangement was set up and taken into operation in this work. The whole setup is mounted on the inside of the TSR. A photograph of the completed setup is shown in Fig. 3.2.

The dimensions of the crystal are 20 × 20 × 10 mm (width×height×depth). It is enveloped by a aluminum casing for fixation and shielding from stray light. A thin aluminum foil (thickness 0.75 $\mu$m) blocks stray-light from the entrance window. The light is coupled out of the crystal on its underside. The crystal's top and side-surfaces are polished and coated with aluminum to reflect the emitted light to the crystal's underside and increase the photon count. A glass rod transmits the emitted scintillation light from the crystal onto a side-on Hamamatsu R2693 photomultiplier tube (PMT).

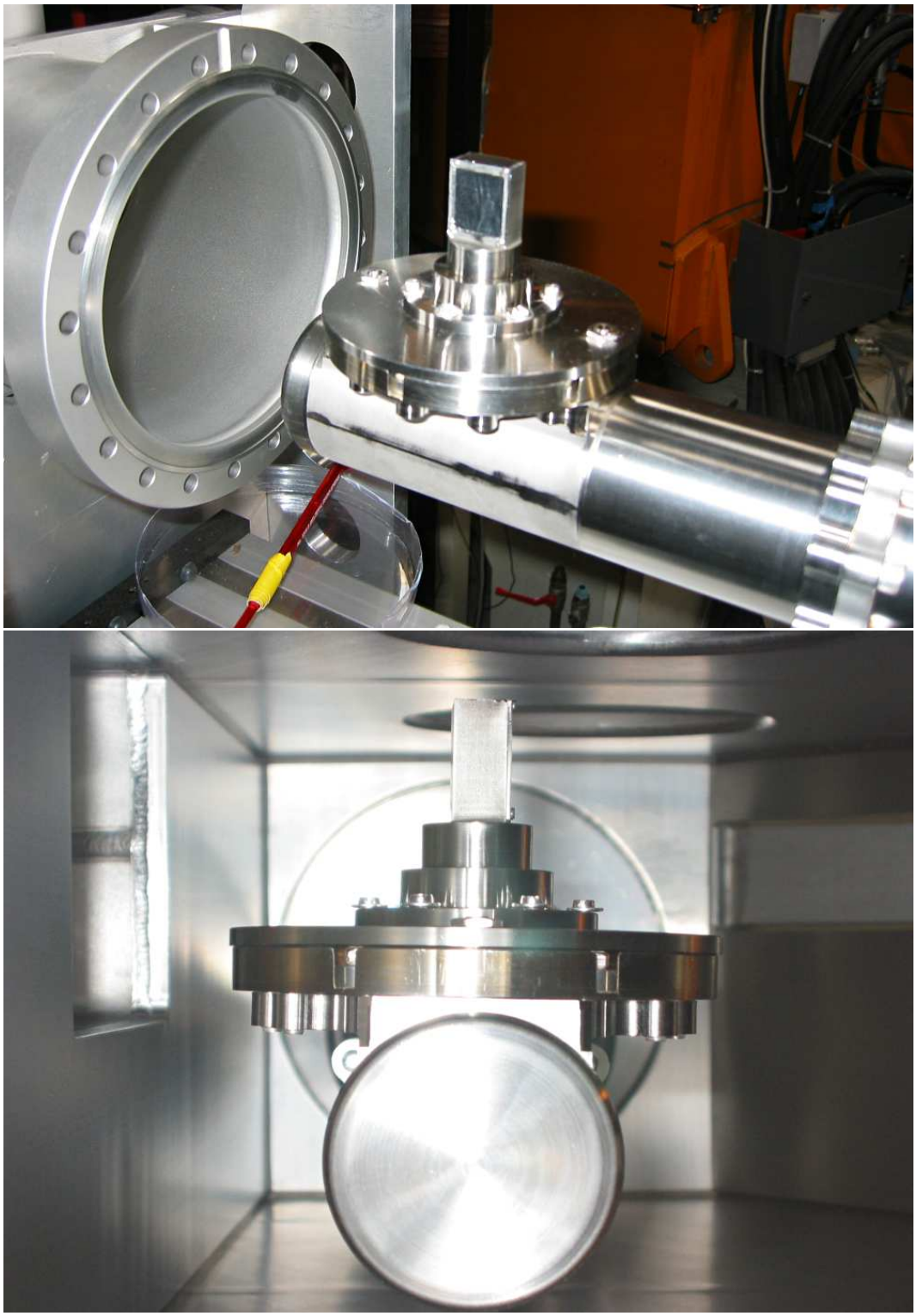

**Fig. 3.4:** *Upper: Head of the detector before installation into the vacuum system. Lower: The MIDAS detector inside of the dipole chamber. On the left Product fragments enter from the right. The stored ion beam passes above the cylindrical support tube into the ongoing* TSR *beamline.*

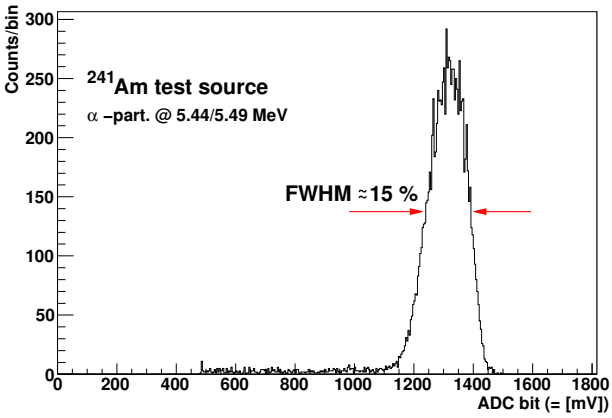


**Fig. 3.5:** *Pulse height spectrum of $\alpha$ particles from a $^{241}Am$ test source at* MIDAS. *One broad distribution with a width of $\approx$ 15 % FWHM is observed. The $^{241}Am$ source emits $\alpha$-particles mainly at two different energies of* 5.442 *or* 5.485 *MeV [LS78]. The difference corresponds the width of two bins and thus may be ignored.*

The glass rod is soldered into a non-magnetic stainless-steel frame and separates the UHV side from the low-pressure inside of the support tube. The support tube houses the photo-multiplier and is on *low* pressure, pumped by a regular oil pump. One end is mounted on a movable slide. The head of the detector support is made of titanium to reduce the weight. As insulation in between the steel and titanium surface the original design had foreseen to squeeze gaskets of gold-wire. However, it had turned out in several attempts, that the leak rate of the gold-gaskets was unacceptable high and the UHV-part of the detector didn't reach vacuum pressure below $10^{-7}$ mbar. The flange surfaces were refined several times, without much impact on the final vacuum. As a compromise PTFE[1] gaskets were installed. However, PTFE is not an ideal material for UHV-conditions, as it leaks as well slightly and gases out hydrocarbons. With the PTFE gaskets the final vacuum in the detector chamber improved significantly. The leaking is worked around by pumping of inner support tube with a regular oil pump. With this measures the detector chamber sustains a vacuum with a rest-gas pressure of $2 \times 10^{-10}$ mbar by itself with the installed pumps.

The pulseheight is proportional to the impact energy. The resolution is limited by the photon statistics. A measurement of the pulseheight spectrum is shown in Fig. 3.5. This spectrum shows detected 5.5 MeV $\alpha$ particles from a $^{241}$Am test source.

## 3.3 Experiment control and data acquisition

The control of the instruments for experiments at the TSR is divided into two domains, fast and slow parameters.

The slow domain is accessible through a dedicated EUNet system[2]. This consists of a networking master, to which several remote slave units with digital and remote IO can be connected via serial or optical fiber lines. The slaves house multiple digital and analog in- and outputs. High latencies inhibit usage of the EUNet system on time scales below a second. A unified interface based on the HSI-Pult software[3] allows

[1] Poly-tetra-flour-ethylene
[2] MPI-K, in-house standard, W. Schreiner, et al.
[3] MPI-K, Holger Schneider, Rolf Epking

the experimenter to precisely tune every parameter. During a measurement these parameters are kept static.

Decoupled from this domain is the data acquisition system (DAQ). It controls all fast parameters and reads out the state of the involved instruments. Among the fast parameters are injection requests to the accelerator, variation of the electrons kinetic energy and detector readout.

**Data acquisition setup** A VME computer system has been installed as a DAQ front-end. Based on a Debian-Linux[4] operating system with VME support [Kih01] a special software system, *mileDAQ* (See Appendix A and [Les06, LSH]), was implemented as a part of this work. The system implements VME boards for counting of digital pulses, peak-sensing ADC channels, digital IO, and a optical fiber communication system to set the platform voltages of both coolers.

Most fast parameters at the TSR have traditionally been frequency-coded digital pulses. The advantage is that digital pulses can be transferred without information loss over long distances and are easily converted to the desired level. Analog signals are converted on-site to a frequency signal using voltage-to-frequency converters (VFC). For counting of the pulses the DAQ front-end houses a 250MHz 32-channel multiscaler board Struck SIS3820 (Firmware-version 1.02). The input channels are arranged in four groups of eight channels. Additional logic input channels allow enabling and disabling the channels group-wise. Starting, stopping and latching of the scaler board happens via the VME backplane.

A 8-channel peak sensing ADC with 16 bit resolution is used for recording of pulse-height information from, e.g., surface-barrier semiconductor detectors.

Digital IO is done by a MPIORL trigger board with interrupt capability.

A master gate is implemented on one of the MPIORL output channels can be coupled in a logical &-operation to the scaler channels and detector readout. This allows simultaneous switching of all input signals and ensures synchronicity of the data.

For variation of the electrons kinetic energy a fast bipolar HV amplifier (Kepco BOP1000M) is stacked on top of the slow main HV power supply. Control of the desired value of the HV amplifier is established by a Burr-Brown DAC703 bipolar 16-bit digital-to-analog converter (DAC) which is installed into the high voltage cage. This DAC is connected to the data acquisition system via an optical fiber for galvanic decoupling. The VME setup houses an IPC01 carrier board, and the optical transmitter is piggy-packed on top of this. The transmitter has two outputs, so that independent DACs can be installed into the electron cooler and electron target platforms. The overall response time, from writing the desired DAC value into the serial communication line's output buffer up to establishing the requested value on the analog DAC output is below 64 $\mu$s.

**Product fragment detection** Depending on the used detector type, the detection of product impacts is recorded differently. The scintillation light from the *MIDAS*

[4] `http://www.debian.org`

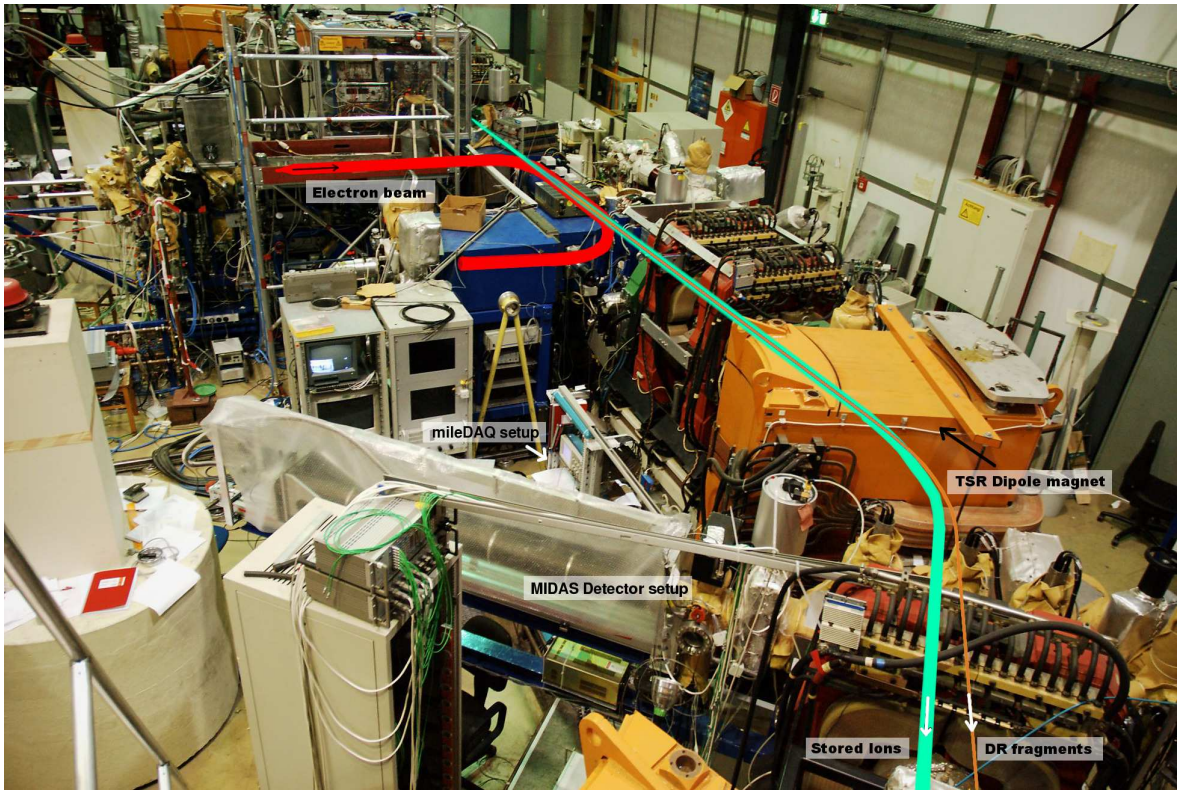


**Fig. 3.6:** *Overview of the experimental setup at the* TSR.

detector crystal is read out by a photomultiplier (PMT). Pulses from this detector are evidence for a particle impact. The pulse itself contains all important information, as only one species of products may be detected due to the $\kappa$-selectivity of the detector. Background radiation count rate is below $f_{\text{back}} < 1$ Hz and may be ignored for almost all experiments. Using fast analog electronics the output signal from the PMT is amplified, shaped and discriminated. If the pulse-height of the detected particle is above the background threshold the discriminator produces a logical pulse. This pulse is counted by the scaler.

In molecular experiments, where neutral fragments of different masses are detectable at the *Bambi* beamline, a surface barrier semiconductor detector is used for detection of the product masses. The signal is amplified and recorded by the peak-sensing ADC for acquisition of pulse-height spectra. Since the time resolution of the semiconductor is to low, it records the mass sum of all incidenting fragments.

**Measurement scheme** The DAQ software is able to implement various measurement schemes. However, for measurement of dielectronic recombination the following standard scheme has been established.

The platform HV is set to a start value; depending on the specific experiment this can be the voltage at cooling or the voltage of the first measurement step. An injection is requested from the ring control by sending out a short TTL pulse and confirmation by the accelerator control. Give the ion beam time for cooling. A *wobble*-scheme is

implemented to scan a preconfigured energy range. It is flexible and may interleave steps for ion-beam cooling at zero relative energy or measurement of the background contribution at a non-zero relative energy, where no DR contributions are expected. The order of the steps within one wobble-cycle is specified in the configuration file by the experimenter. The electron beam energy during reference- and cooling-steps is constant throughout the scan. During the measurement-step the electron energy is ramped in pre-configured intervals. Each individual step in this scheme starts by setting the individual voltage for this step, then a short time ($\approx$ 5 ms) is waited to allow the platform voltage to settle. Next the master gate is enabled. A specified acquisition time is awaited, until the master gate is turned off again. Then the DAQ software sweeps through all counters and writes the raw data to file.

For the ramp configuration of the measurement voltage one has generally two options which have different strengths and drawbacks, depending on the situation.

**Complete energy scan within one injection loop:** The energy of the next measurement step is iterated after finishing one wobble-cycle. The whole energy range is scanned within one injection loop. The advantages of this method are

- The whole energy range is quickly covered and overview scans obtained in a short time.
- Each injection loop is repeated at similar conditions.

The disadvantages of this method are

- Delays due to limited slew rate restrict to short energy intervals per scan for shortly-lived ion species.

**Iterate electron energy after completed injection loop:** The energy of the measurement step is kept constant within one injection loop. The wobble cycle in such a loop repeats multiple times. Advantages of this method are

- The energy range is not limited by the ion beam lifetime.

Disadvantages are

- Long-term variations of the restgas pressure, due to the slowly iterating electron energy in the measurement step lead to variable ion beam lifetimes and background rates, depending on the progress in the energy scan.
- It takes a long time to complete the scan range.

Both methods are in use. While the first method is common for experiments on atomic ions, which have long ion beam life times in the TSR, the second method is applied to short-lived molecular ions.

# Chapter 4

# Beam optimization and control in high-resolution electron targets

Merged collinear electron beams are produced in most modern heavy ion storage rings, where they serve the purpose of electron cooling or as targets for electron impact spectroscopy. In cooling mode the ion beam repeatedly passes through a heat bath of cold electrons and transfers its relative energy onto the electrons. By continuously providing a reservoir of cold electrons the ion beam reaches a regime where the ion beam's internal relative energy is in equilibrium with external heating mechanisms. At this stage the longitudinal and transverse energy spread of the ions is reduced and the density and brilliance of the ion beam are increased.

In a different mode of operation the electrons serve as energy-detuned targets for spectroscopy of ionization-, excitation-, and recombination experiments on atomic or molecular ion beams.

Electron cooling and target operation impose a strong demand for intrinsically cold electron beams with well-defined kinetic energy. The production of monoenergetic electron beams is outlined in this chapter. Systematic studies of heating effects by transverse-longitudinal- and longitudinal-longitudinal-relaxation are presented in this chapter.

## 4.1 The Heidelberg electron target

The heavy ion storage ring TSR has been equipped with a second electron beam device [Spr03] as a dedicated target for electron impact spectroscopy, in addition to its electron cooler. A description of the implication for TSR measurements is given in Chapter 3.

The electron target is set up as shown in Fig. 4.1. The orientation of the electron beam is in the horizontal plane. It is divided into sections for beam formation and acceleration, merging, interaction, demerging and a collector section. The setup is mounted on rails and can be removed from the TSR to allow installation of different experimental setups, such as for laser spectroscopy [Rei05].

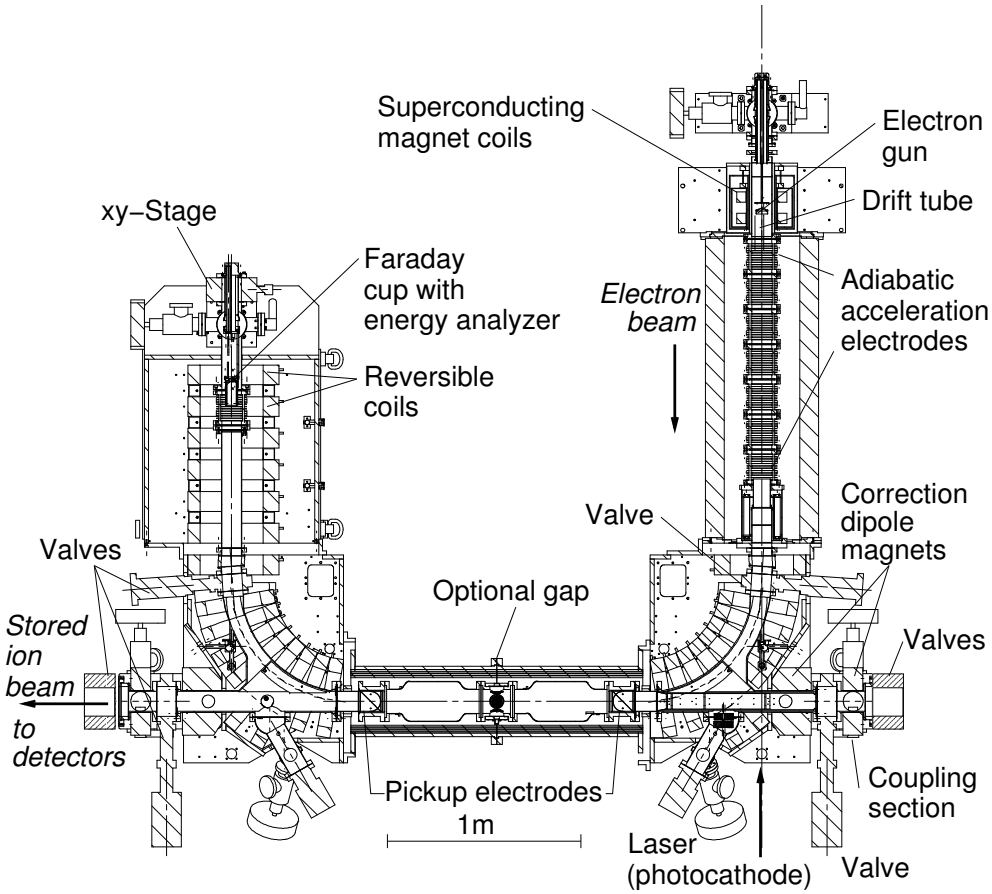


**Fig. 4.1:** *Schematic overview of the Heidelberg electron target device.*

**Beam formation section** The section for beam formation employs methods for adiabatic transverse expansion and adiabatic acceleration. Two different types of electron emitters are available. In regular operation a Heatwave thermionic cathode produces intense electron beams up to 100 mA.

Highest resolution may be achieved by the developments on GaAs semiconductor photoemitters [Wei03], which have made an ultracold photocathode available. Cathode lifetimes of 15 hours were possible at electron currents of 200 $\mu$A.

The adiabatic transverse expansion is achieved by placing the cathode into a region of high magnetic field and extracting the electrons into a region of a reduced guiding field. This beam expansion effectively reduces the transverse energy spread (See Section 2.4.5).

The acceleration of the electron beam to its final collision energy is applied in multiple steps to suppress relaxation contributions to the longitudinal temperature (see Section 2.4.6). For this 77 ring electrodes are aligned on a straight 1.4 m section after the transverse expansion region. The potential on these ring electrodes can be adjusted individually.

**Interaction Section** The interaction section provides a homogeneous magnetic field parallel to the ion beam. The geometrical length of this region is 1.47 m [Spr03].

In order to obtain the ion- and electron beam positions the position sensitive pickup electrodes have been installed at the entrance and exit of the interaction section.

To allow observation of photons originating from the collision process it is possible to open a small gap of about 4 cm in the magnetic shielding in the middle of the interaction section. Additional detectors may be installed there.

**Merging and demerging sections** The merging and demerging with the ion beam is done by 90° toroidal magnetic fields. The electrons are light and follow the magnetic field lines, while the force onto the heavier stored ions ($m_{\text{ion}} \approx 1836 \cdot A \cdot m_e$) produces a slight distortion from the anticipated straight path. The toroidal field produces a horizontal magnetic field component $\vec{B}_\perp$, which is perpendicular to the ion trajectory. The Lorentz force $\vec{F} \propto \vec{v} \times \vec{B}_\perp$ bends the ion beam out of the ring plane. To adjust a closed orbit one has to correct this field. Therefore two dipole magnets are installed in front of the merging and behind the demerging toroids to produce, together with the toroidal field, a $\uparrow\downarrow\uparrow$-type sequence of magnetic fields perpendicular the ion motion.

**Collector section** The collector section decelerates the electron beam and dumps it onto a collector cup. The collector region can be operated in two different modes. In normal operation the last coil of the guiding field is set to reversed magnetic field polarity against all other coils. This spreads the electron beam to a larger diameter on the collector cup. For electron beam analysis the coil polarity can be retained parallel to the other sections. A fraction of the electron beam passes through a tiny pinhole in the collector cup and reaches into a retarding field analyzer. This analyzer is used for measurements of the transverse electron density profiles and longitudinal energy spread.

**Platform voltage** A critical parameter for measurements with the electron target are the platform voltage, defining the cathode potential and thus the energy of the electrons. A calibrated module has been provided by the workgroup of Prof. Alfred Müller, Universität Gießen, to achieve a precise measurement of the platform voltage. This module is a voltage divider for measurements up to 10 kV. The measured voltage is stepped down by a factor of 1/1000. For submission to the data acquisition system (section 3.3) the stepped down voltage is translated into a frequency signal using a voltage-to-frequency converter (VFC) with $f \propto U_{\text{cath}}$ with a maximum frequency of $f_{\text{max}} = 500$ kHz for $U_{\text{cath}} = 10$ kV. The relative precision of the voltage divider is $10^{-4}$ [Scha].

Non-evaporative getter pumps, Titanium sublimation getter pumps and ion getter pumps are installed in all sections to establish conditions of ultrahigh vacuum ($< 10^{-10}$ mbar).

All sections are equipped with steering coils for alignment of the electron beam

**Table 4.1:** *Measured transverse displacement of the electron beam xy the steering coils at ($B_{\text{guide}} = 0.04$ T) at the analyzer position..*

| Steerer | Displacement | |
|---|---|---|
| | [mm/A] | [inch/A] |
| Acceleration X | -3.98 | -0.156 |
| Acceleration Y | -4.06 | -0.160 |
| Toroid 1 X | 2.72 | 0.107 |
| Toroid 1 Y | -3.58 | -0.141 |
| Interaction X | -8.00 | -0.315 |
| Interaction Y | -8.89 | -0.350 |
| Toroid 2 X | -2.68 | -0.106 |
| Toroid 2 Y | -3.34 | -0.133 |
| Collector X | 1.87 | 0.074 |
| Collector Y | -2.19 | -0.086 |

position. These coils stretch along each section respectively and are arranged in vertical and horizontal couples, surrounding the vacuum tube. The steering provides one of the most important control functions, as it allows to tilt the magnetic guiding field $\vec{B}_{\text{guide}}$ and thus the magnetized electron beam in the horizontal $x$ and the vertical $y$ direction. They provide a tunable magnetic field component $\vec{B}_x$ and $\vec{B}_y$ perpendicular to the main guiding field $\vec{B}_z = (0, 0, B_z)$. The additional field tilts the sum field $\vec{B}_{\text{guide}} = \vec{B}_x + \vec{B}_y + \vec{B}_z$. This tilting is local to the respective section covered by the steering coils. In the downstream sections, this provides an offset of the electron beam position.

## 4.2 Steering magnet calibration

The effect of the steering coils can be measured directly by the movable retarding field analyzer, which is mounted on a precision XY-translation stage. Varying the electrical current through each steering coil couple, the shift of the transverse electron beam profile at the position of the collector can be measured. From these measurements one can obtain a calibration $D$ of the steering coils. Measurements of the displacement parameters $D$ have been performed at a guiding field of $B_{\text{guide}} = 0.04T$. The obtained displacement parameters $D$ are summarized in Table 4.1.

## 4.3 Measurements of the electron temperature

The retarding field analyzer (Fig. 4.2) is used to measure the longitudinal energy spread of the electron beam in the collector section. For these measurements the magnetic field configuration in this region section is set to homogeneous mode, else the electron beam would spread out. A small hole in the collector allows a fraction of the beam to pass to the analyzer. A collimating electrode reduces the diameter of the passing beam ($d = 50$ $\mu$m, [Spr03]) in the collector cup and allows a small fraction of the total electron beam to pass through onto a analyzer cup. A cylindrical ring electrode in between

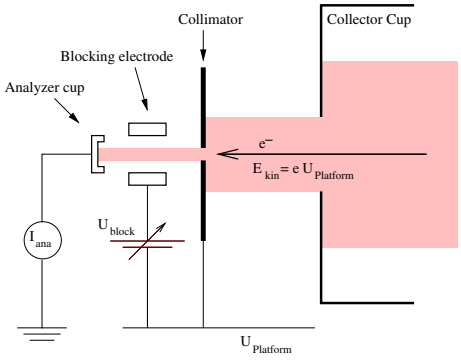


**Fig. 4.2:** *A small hole in the collector cup allows a tiny part of the electron beam to pass through to the analyzer. An entering aperture collimates the beam to a diameter of* $\approx 50$ $\mu$m*. A blocking electrode surrounds the analyzer current and creates a potential wall for the electrons. The passing fraction is measured as a function of the blocking potential.*

creates a variable potential wall $U_{\text{block}}$ for the electrons passing through the aperture. The fraction of the electron beam $I_{\text{ana}}$ reaching the analyzers collector is measured by a sensitive $I/U$-converter. Measuring the transmitted fraction in dependence of the blocking potential allows to determine the energy distribution of the electron beam. One obtains the longitudinal temperature $k_B T_\parallel$ by

$$k_B T_\parallel = \frac{\sigma^2}{2E_{\text{kin}}}, \tag{4.1}$$

with $\sigma$ the spread of the electron energy, and the electrons kinetic energy $E_{\text{kin}}$. The operation of the system and the basic analysis procedures for extracting the longitudinal temperature is given in [Spr03]. With it one can systematically analyze the contributions of TLR and LLR effects. The following describes a series of measurements on the dependence on various parameters of the beam formation region to clarify the dependence of the longitudinal temperature on the density of the electron beam, the length of the low-energy drift region, magnetic guiding field, and energy of the low-energy drift region. Due to the larger range of possible electron currents these have been acquired using the thermionic electron gun.

**Density dependence** Equation (2.31) for the description of the longitudinal-longitudinal relaxation is proportional to the reciprocal value of the mean electron distance $1/d = n_e^{1/3}$. One would expect to be able make to use of this dependence to estimate the adiabaticity of the acceleration structure at the electron target setup by comparing measurements at different densities.

For this purpose a series of measurements was performed at $E_{\text{kin}} = 2000$ eV, $B_{\text{guide}} = 0.04T$ and expansion ratio $\xi = 20$. The electrons were extracted with currents ranging from 1.75 mA to 14 mA and a 50 V potential difference was kept between the extraction electrode and the drift tube. At the exit of the drift-tube the electrons were accelerated towards ground potential in a linearly sloped potential drop, established by eight succeeding ring electrodes over a distance of 100 mm.

The observed behavior is shown in Fig. 4.3. The blue line is shown to guide the eye only. One finds a good agreement with the expected linearity of the temperature increase at small electron densities. However, towards the higher density regime a strongly increasing longitudinal temperature is observed, which is in deviation from

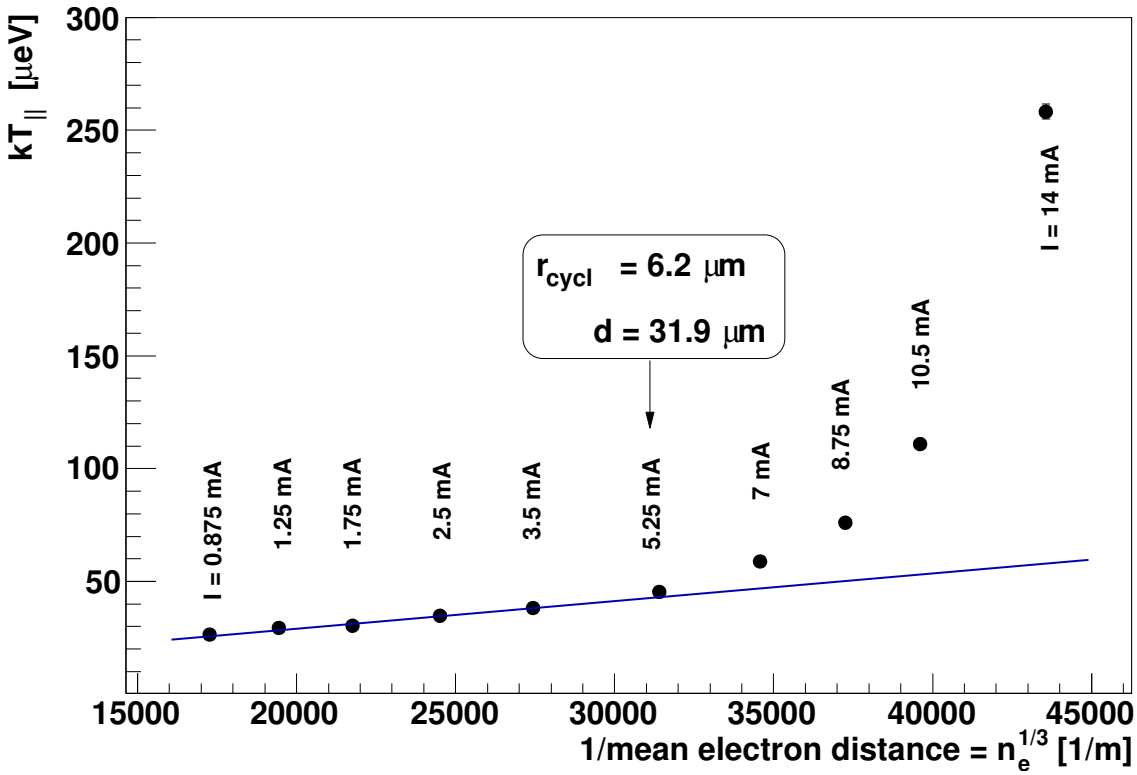


**Fig. 4.3:** *Dependence of the measured longitudinal temperature $k_B T_\parallel$ on the density of the electron beam $n_e$. The blue line is to guide the eye only.*

the expected linear (equation 2.31). The critical electron current up to which LLR largely dominates the heating process at the conditions of this measurement is 5.3 mA.

The most probable explanation for this behavior is the onset of additional TLR, transferring energy from the transverse motion, which increases towards higher densities, as the inter-electron distance $d$ decreases while the radius of the cyclotron motion $r_{\mathrm{cycl}}$ is defined by the transverse temperature $k_B T_\perp$. A clarification of the observed behavior will be achieved in the following.

**Drift length dependence** At a kinetic energy of the electron beam of $eU = 2000$ eV the TLR contributions were measured. The anisotropy of the transverse and longitudinal temperature ($k_B T_\perp \ll k_B T_\parallel$) causes continuous energy transfer from the transverse onto the longitudinal degree of freedom. This process is strong, when the electron density is high and the mean electron distance and the cyclotron radius are of the same order of magnitude. Then the electrons circulating along the magnetic field lines repeatedly approach and depart from each other. The Coulomb repulsion between the electrons varies, as their relative distance varies, and leads to transfer of energy. Thus the transfer has to be an ongoing process, which happens along the full beam length and a dependence of the beam length should be observed.

However, this length cannot be easily tuned at the electron target setup and one has to apply a simple trick. The beam formation stage of the electron target allows to freely shape the accelerating potential. Following to the drift section 77 ring electrodes

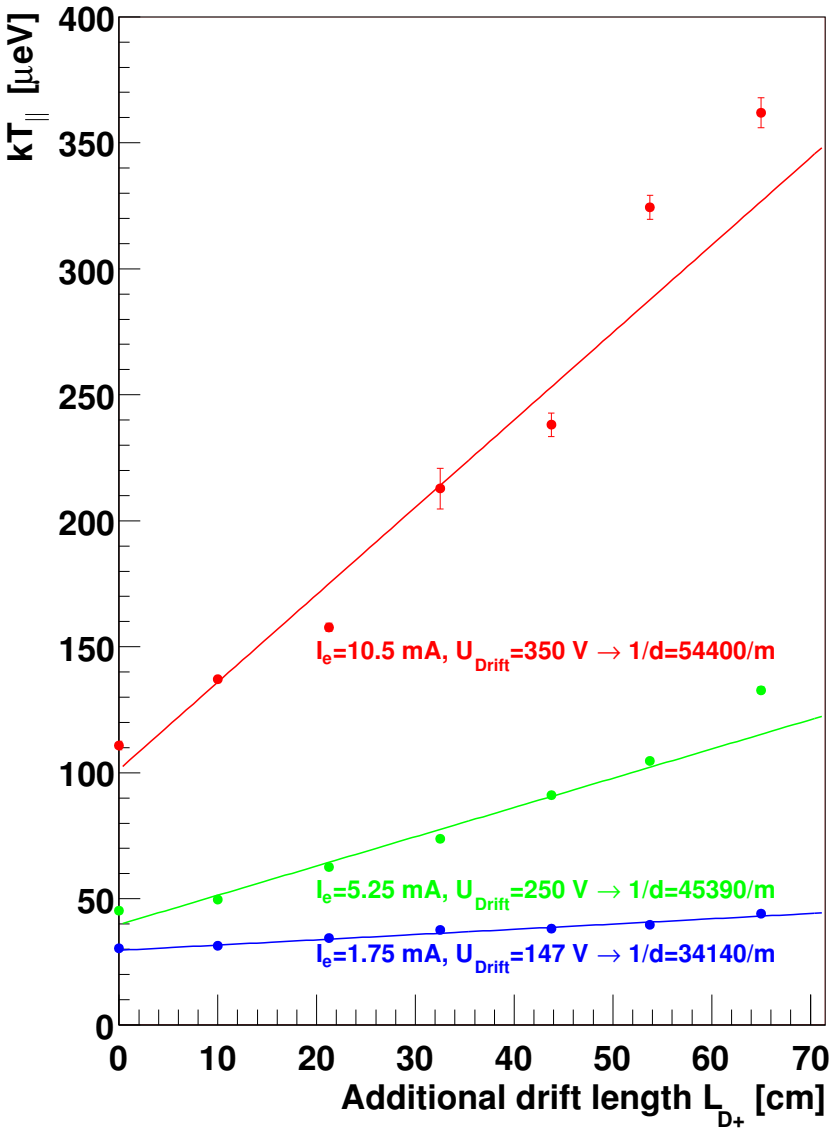


**Fig. 4.4:** *Longitudinal temperature measured for different lengths of the additional drift region $L_{D+}$ (see Fig. 2.13) and three different electron currents. Heating rates of $dk_BT_\parallel/dz$ = 0.21 $\mu$eV/cm, 1.16 $\mu$eV/cm, and 3.48 $\mu$eV/cm are found for $I_e$ = 1.75 $mA$, 5.25 $mA$, and 10.5 $mA$, respectively.*

surround the beam and allow shaping of the potential drop (see Fig. 2.13). By introducing an additional drift region of length $L_{D+}$ connected to the drift tube potential, the low-energy drift region can be variably prolongated. Due to the reduced voltage in this drift region, the electron density is higher compared to the remainder of the electron target and it is assumed that the dominant TLR contribution originates from this region, thus possible small TLR contributions from the remaining high-energy sections are ignored.

The results of such measurements are shown in Fig. 4.4 for different electron beam currents and drift energies.

**Magnetic guiding field dependence** Using the artificially prolonged drift section and the enhanced TLR contribution one can vary the magnetic guiding field $B_{\text{guide}}$. The radius of the cyclotron motion is reduced at higher magnetic field and one expects a decrease of the TLR contribution (see Fig. 2.12). The increased magnetic guiding

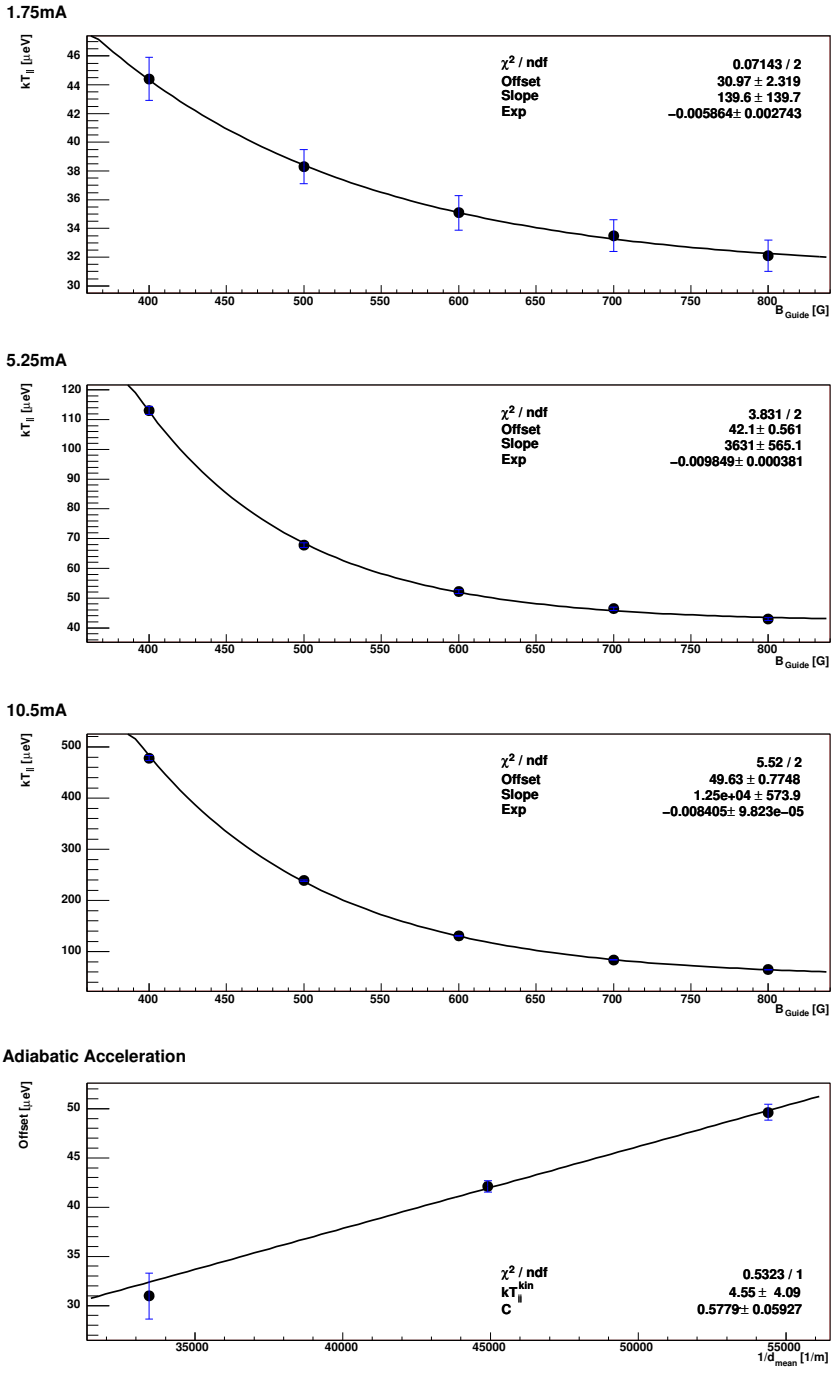


**Fig. 4.5:** *TLR dependence on the magnetic guiding field strength $B_{\text{guide}}$ for electron currents of 1.75 mA, 5.25 mA and 10.5 mA from top to bottom. Lowest graph: Fitted offsets are an extrapolation to infinite mangetic guiding field and all TLR contributions are suppressed. This allow determination of the C-parameter of LLR (equation 2.31).*

field was compensated by proportional increase of the magnetic field in the gun region to keep the transverse electron temperatures constant throughout this series. The measurements agree with the expectations (see Fig. 4.5). The solid lines are fits to the data points using an exponential function

$$k_B T_{\parallel}(B_{\text{guide}}) = \langle \text{Offset} \rangle + \langle \text{Slope} \rangle \exp(\langle \text{Exp} \rangle \, B_{\text{guide}}) \tag{4.2}$$

The the fitted offset is an extrapolation to infinite magnetic field and ultimately suppressed TLR. In such a regime only kinematic transformation and LLR make up the

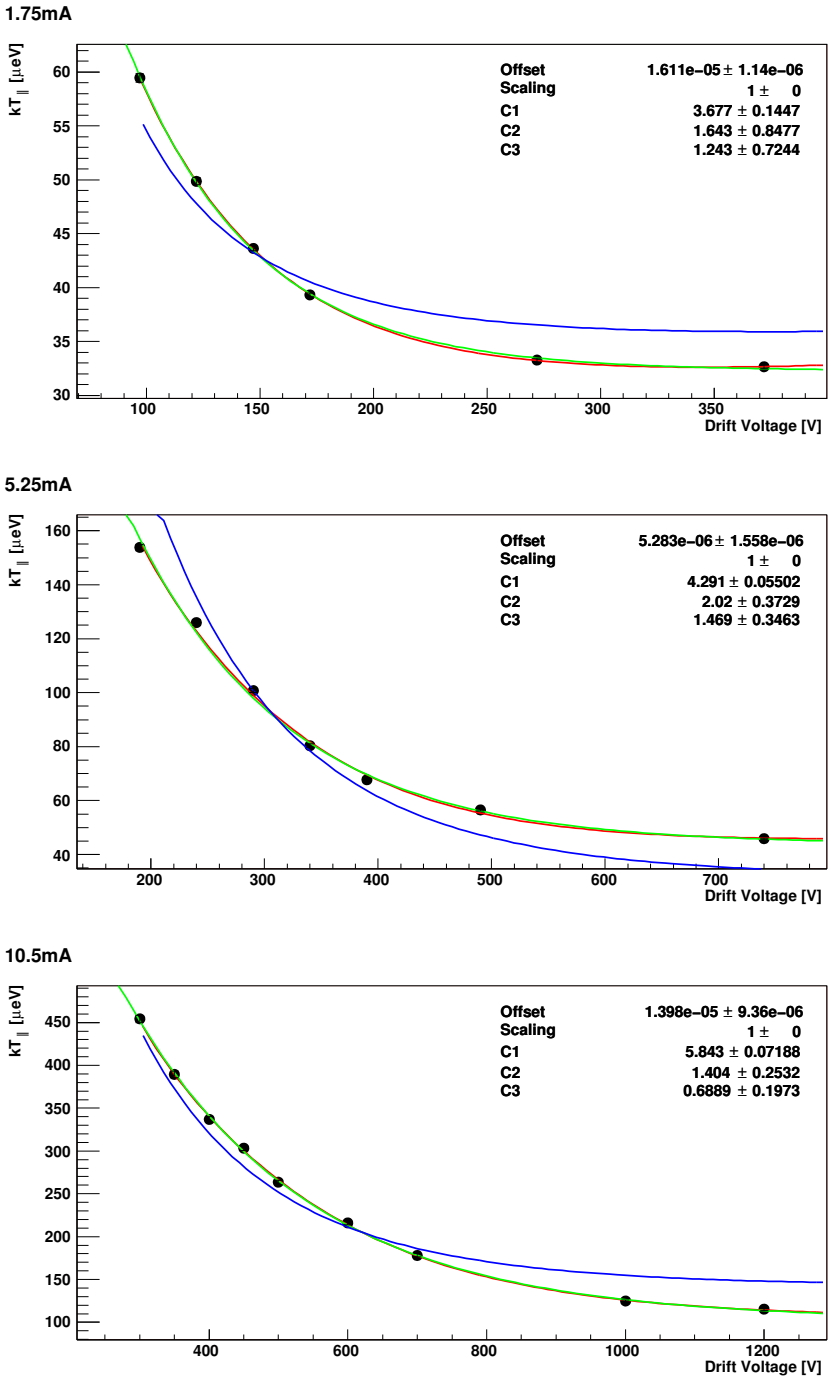


**Fig. 4.6:** *Dependence of TLR on the drift energy, measured for* 1.75, 5.25 *and* 10.5 *mA. Fitting of the different models (see description in text), based on the empirical description [DKL+88] (red curves; see equation 2.28) and the plasma theory [OH85] (blue curves; see equation 2.30). The green curves are exponential fits.*

energy spread. The lowest figure plots the fitted offsets versus $1/d_{\text{mean}} = n^{1/3}$ and a linear dependence, according to equation (2.31), is fitted. One finds $C = 0.58(6)$.

**Drift voltage dependence** The drift voltage is another important parameter for the TLR contribution. To emphasize the influence the drift section retained prolonged by $L_{D+} = 650$ mm as in the measurement shown before. Keeping the electron current constant a variation of the drift voltage affects the inter-electron distance. Faster electrons also perform less cyclotron oscillations within the drift section. Both arguments

| Reference | $C_1$ | $C_2$ | $C_3$ |
|---|---|---|---|
| [Ale90] | $6.34^{+2.26}_{-1.48}$ | $1.3^{0.4}_{-0.35}$ | $0.4^{0.21}_{-0.14}$ |
| [DKL$^+$88] | $0.87 \cdot L_c$ ($L_c \approx 6$) | 2.8 | 1 |
| [Kra92] | $6.75 \pm 1.75$ | $1.85 \pm 0.15$ | $0.3 \pm 0.1$ |
| This work 1.75 mA | $3.68 \pm 0.15$ | $1.64 \pm 0.85$ | $1.24 \pm 0.72$ |
| 5.25 mA | $4.29 \pm 0.06$ | $2.02 \pm 0.37$ | $1.47 \pm 0.35$ |
| 10.5 mA | $5.84 \pm 0.07$ | $1.40 \pm 0.25$ | $0.69 \pm 0.20$ |

**Table 4.2:** *Comparison of the parameters for Parkhomchuk's empirical TLR theory [DKL$^+$88], equation (2.28) from literature and the measurements performed here.*

indicate towards reduced TLR for higher drift-tube voltages.

The experimental behavior of the measured electron current is shown in Fig. 4.6. For currents of 1.75 mA, 5.25 mA and 10.5 mA the drift tube voltage has been varied. A lower limit for the tunable drift potential $U_{\mathrm{Drift}}$ is given by the respective potential of the extraction electrode ($U_{\mathrm{extr}} = (I/P)^{2/3}$) at a given electron current. One finds a decrease of the longitudinal temperature, as expected qualitatively.

One can compare the observed behavior with the empirical (2.28) [DKL$^+$88] and the plasma theory (2.30) [OH85] models and a simple exponential fit. A model has been made, in which electron beam was followed along the beam axis. The path $s$ of the electrons from the cathode surface was followed in 100 short steps through the drift region. For each step $s_i$ the heating contributions by TLR, as predicted by the individual theory was calculated and added on top of the longitudinal temperature $k_B T_\parallel(s_i)$ with $n_e(s_i)$, $T_\parallel(s_i)$, $b_\parallel(s_i)$, $r_{\mathrm{cycl}}(s_i)$, The model includes the feedback of the enhanced longitudinal temperature on $b_\parallel(s_i)$ (see equation 2.29). From $k_B T_\parallel(s_i)$ and $b_\parallel(s_i)$ the next iteration step $s_{i+1}$ is calculated. In addition, the model includes the LLR of the final acceleration step with $C = 0.58$ (see above). The contributions of the remaining sections of the electron target were considered to be constant and added as an offset to the final temperature. The result of the fits of both theory models, along with a simple exponential fit-function, are displayed in Fig. 4.6.

The empirical model based on equation (2.28) was fitted with free parameters $C_1$, $C_2$ and $C_3$ to the experimental data (red curve). It shows a generally good agreement with the data. The fitting results for the $C_1$, $C_2$, and $C_3$ parameters agree differently well with literature values [DKL$^+$88, Ale90, Kra92]. While insufficient agreement is found at lowest electron current, this improves towards the measurement at highest electron current. It is remarkable that the results of the measurements for there tested electron currents of 1.88 mA, 5.25 mA and 10.5 mA differ as well. A comparison is compiled in Table 4.3.

The plasma theory model (blue curve) [OH85] shows bad agreement with the experimental data. In order to improve the comparison, a variable scaling parameter has been included and fitted to the experimental data. One finds scaling factors of 2.71, 4.03, and 3.69 for the 1.75 mA, 5.25 mA, and 10.5 mA measurements, respectively.

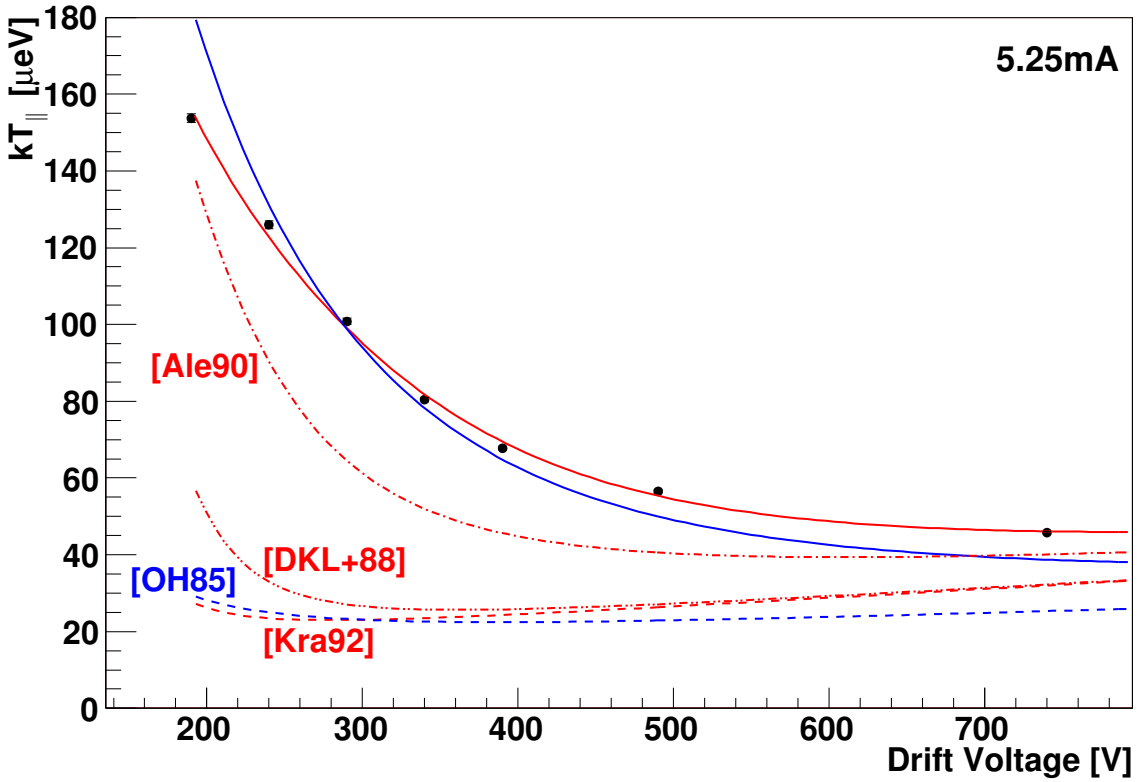


**Fig. 4.7:** *Comparison of the model results, exemplarily for the 5.25 mA measurement. The calculations based on the empirical model [DKL$^+$88] are plotted as red curves for different $C_1$, $C_2$ and $C_3$ parameters. The results based on the plasma theory model [OH85] are shown as blue curves. The solid lines are the results of the fitting performed here. The dashed and dash-dotted lines are model calculations following parameters from literature.*

**Optimization of the acceleration structure** In order to show the pure effects from LLR one needs to minimize the TLR contribution as far as possible. The strongest means to suppress the TLR effects has been found to increase the magnetic guiding field to $B_{\text{guide}} = 0.06T$. At higher magnetic fields a instability of the used power supplies was observed, so that even higher magnetic fields were excluded by technical limits. The expansion ratio for the following has been increased to $\xi = 30$. This has two beneficial effects. First, it decreases the density of the electron beam slightly. Second, and more important, the transverse temperature is reduced, which in consequence decreases the cyclotron radius (2.16).

Since a strong effect from LLR is expected to occur at very steep accelerating gradients, a increased platform voltage of $U_{\text{cath}} = 4000$ V was used. It was limited by the operation range of the retarding field analyzer. The drift section was shortened to the natural size, i.e. the length of the inserted drift-tube.

With the minimized TLR using these conditions the measurement of the density-dependence was repeated for different configurations of the acceleration structure. The results are presented in Fig. 4.8 as function of $1/d$, similar to Fig. 4.3. Since the density

is related to the inter-electron potential $V_{ee}$ via

$$V_{ee} = n_e^{1/3} q/(4\pi\epsilon_0), \tag{4.3}$$

the independent axis is scaled accordingly. With this scaling one intuitively understands the relaxation term as a release of the inter-electron potential energy. From Fig. 4.8 a) to e) the accelerating field gradient has been steepened. In subfigure a) the gradient from the exit of the drift-tube potential to ground level was stretched across 8 ring electrodes ($\approx$ 10 cm). In subfigures b) to e) the shortest possible gradient, established by two neighboring ring electrodes (distance $\approx$ 12.5 mm) has been configured and the potential drop $V = U_{\text{cath}} - U_{\text{drift}}$ has been continuously increased, to worsen the adiabaticity of the acceleration and increase the LLR contribution. One finds an increasing $C$-parameter for the relaxation term from subfigure b) to e) which is according to the expectations. However, even at the *worst* possible configuration (subfigure e)) the LLR relaxation term is still rather small ($C = 0.526 \pm 0.008$).

Another interesting comparison between subfigure a) and d) demonstrates the influence of the gradient length, as both apply the same drift-voltage, but the former shapes a smoother potential drop over a 8 times longer distance.

Of the shown configurations the *softest* accelerating gradient was established in subfigure f). The electron beam leaving the drift-tube was first accelerated in eleven steps over a distance of 14 cm to $1/3(U_{\text{cath}} - U_{\text{drift}})$. Then it propagated for 45 cm at constant energy. Finally in second 11-gap gradient the final potential drop to ground potential was established. Despite the soft gradient the observed LLR contribution is surprisingly high. In comparison with subfigure c), which uses the same drift voltage $U_{\text{drift}}$ one finds an increased $C$-parameter. The origin of this behavior is probably explained by a remaining influence from TLR.

The influence of the drift tube voltage on the LLR is shown in Fig. 4.9. This graph summarizes a series of measurements of the longitudinal temperature as a function of the drift voltage $U_{\text{drift}}$ for different electron currents and lengths of the accelerating gradient $L_{\text{grad}}$ (see Fig. 2.13). This series is a clear demonstration of the adiabatic acceleration. For each individual curve one sees an increase of the longitudinal temperature towards higher drift voltages and the obtained curves for equal current and different acceleration structure converge towards higher drift voltages. However, a clear impact of the gradient shape is visible at low drift voltages.

This can be qualitatively understood by the following consideration. The acceleration of the electron beam from cathode potential towards ground potential is a multi-step process. The electron beam extracted from the cathode is transferred into the drift-tube, where adiabatic transverse expansion is applied to the beam. The extraction and acceleration to this pre-acceleration energy is the first step, and happens on very short distance and to a mostly un-expanded beam. The density of the electrons in this region is still very high, thus the beam is very susceptible to relaxation of potential energy. High drift-tube voltages increases the roughness of this first stage and increases the pre-accelerated electron beam's temperature. Hence, to minimize the total LLR it is first desirable to reduce the drift energy. It was so far used relatively high to minimize TLR at high electron currents. At lower currents, however, it

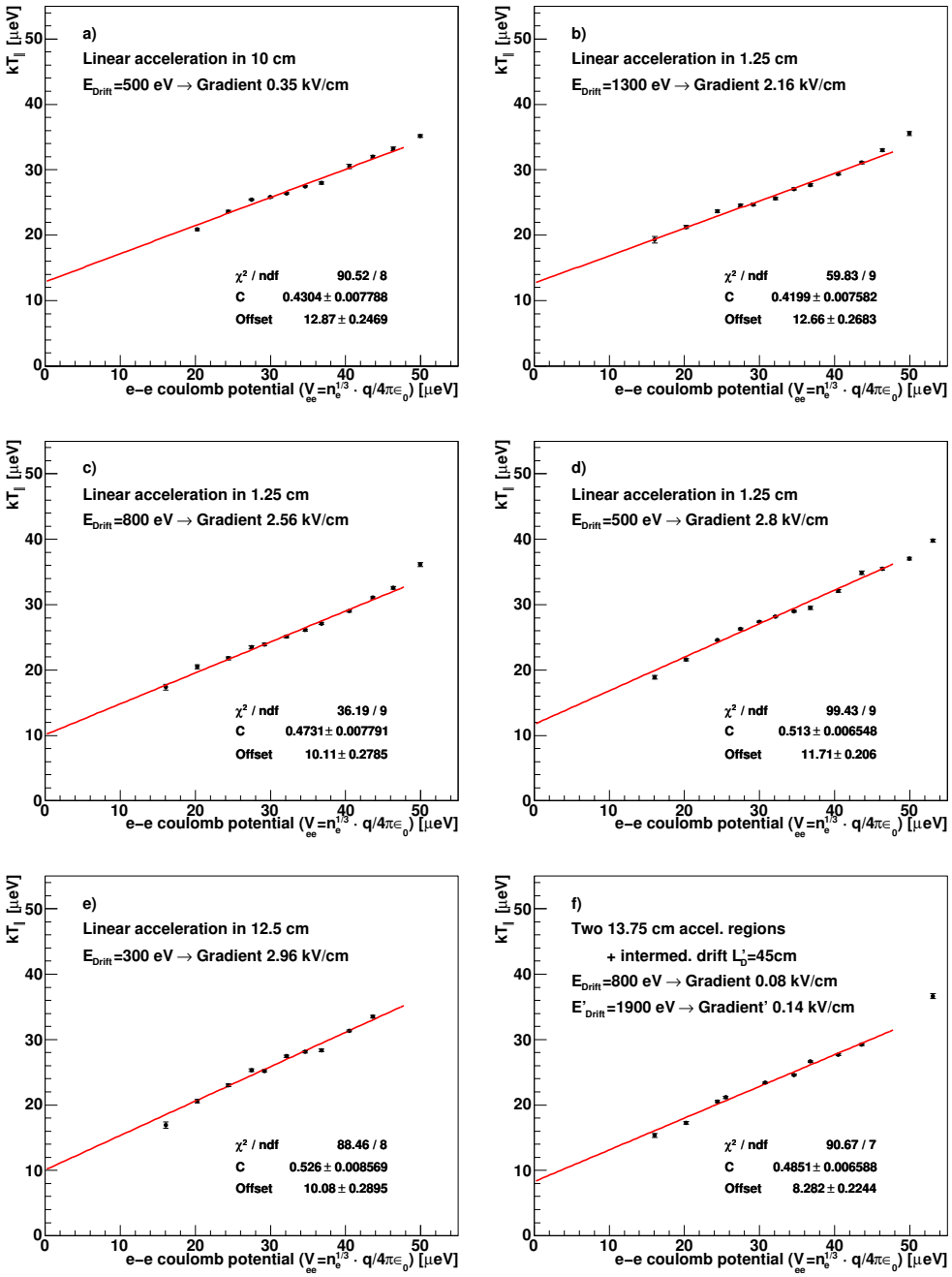


**Fig. 4.8:** *The configuration of the acceleration structure has been varied between each subfigure. The adiabaticity decreases from subfigure a) to e). Subfigure f) has been configured with an intermediate drift section in between of two linear 11-gap acceleration gradients an intermediate drift energy of* $1/3$ *of the final energy. For each figure the density has been varied. The measured* $k_B T_{\parallel}$ *is shown as a function of the inter-electron-potential, which translates to the density by* $n_e^{1/3} q/(4\pi\epsilon_0)$*. The red curves is a fit of (2.31).*

can be reduced to a level where the LLR in the main acceleration structure becomes important. The influence of TLR in in competition to LLR at low drift energies can

be seen at high electron currents ($I_e$ = 10 mA). The acceleration towards the final kinetic energy is applied in a second stage at the exit of the drift tube. The steepness of this stage decreases with increasing pre-acceleration of the electron beam. Also, the density of the pre-accelerated beam decreases with rinsing pre-acceleration, and thus the inter-electron distance is higher. At low pre-acceleration energy the final stage starts with a dense electron beam and is thus most susceptible to the accelerating field gradient.

The two steps of the acceleration contribute competing effects, at higher drift-tube voltages the LLR of the first stage dominates the final temperature, towards lower energies the influence of the final acceleration stage becomes more important.

To summarize the results of the measurements presented in this chapter one can conclude, that in order to achieve ultimately low longitudinal energy spreads one has to use a strong magnetic guiding field to suppress TLR heating and low electron currents. The contributions from LLR have become visible, however, the overall effect is small at the operation conditions used in this setup.

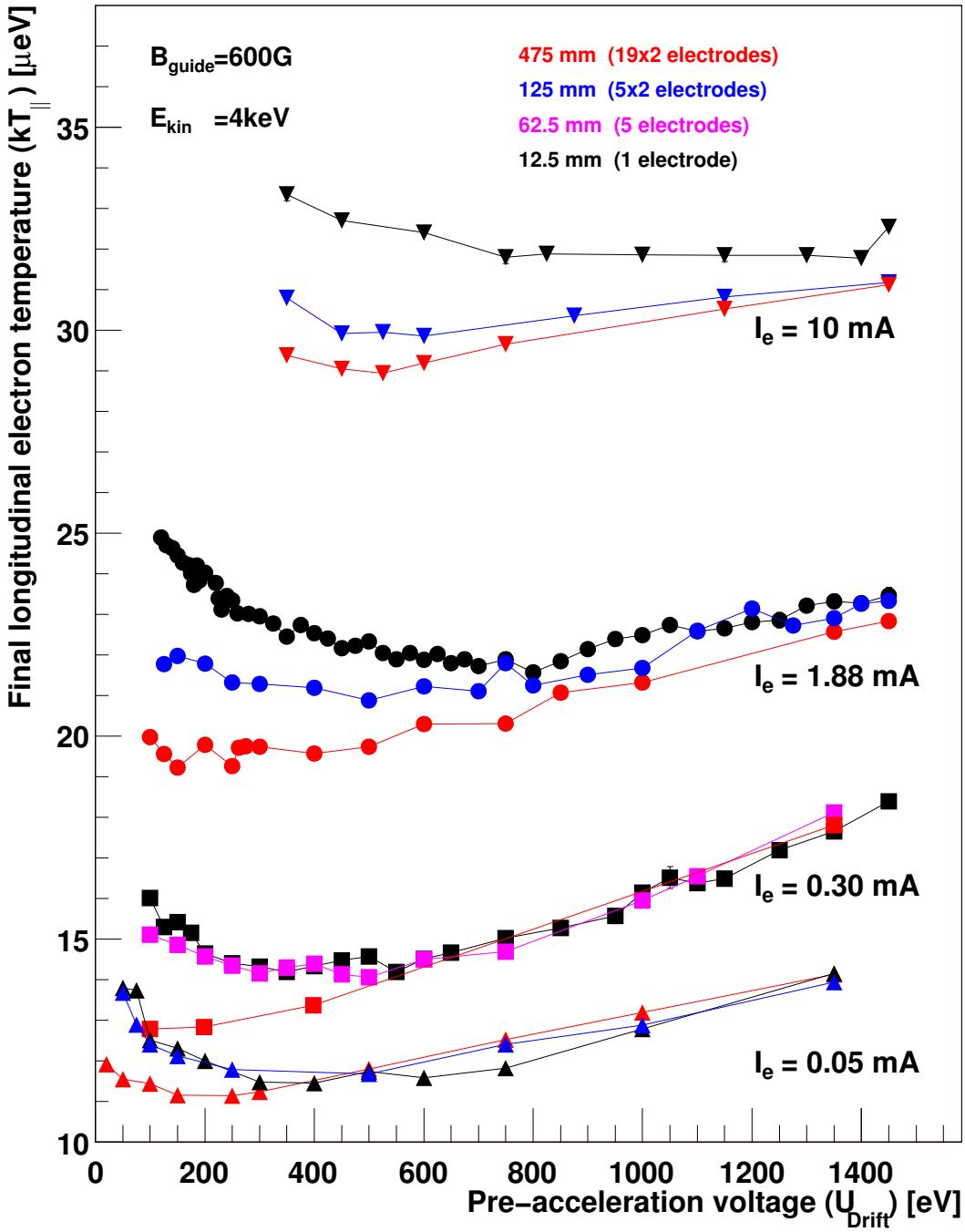


**Fig. 4.9:** *For different configurations of the acceleration field geometry the longitudinal temperature has been measured in dependence on the low-energy drift voltage. The Length of the acceleration gradient $L_{grad}$ (see Fig. 2.13) has been varied between 475 mm (red curve), 125 mm (blue curve), 62.5 mm (magneta curve), and 12.5 mm (black curve). The measurements have been repeatet for three differen electron currents of 10 mA (▼), 1.88 mA (●), 0.30 mA (■), and 0.05 mA (▲). Other electron beam parameters were Electron energy $E_{\mathrm{kin}} = 4$ keV, expansion ratio $\xi = 30$, magnetic guiding field strength $B_{\mathrm{guide}} = 0.06$ T.*

## 4.4 Development of a toroidal drift compensation

The electrons in a toroidal magnetic field are exposed to a field $\vec{B}$ oriented in the plane of the toroid. The centrifugal acceleration in the electron's restframe leads to a bending of the electron beam out of the plane of the toroid. The toroidal drift velocity is [Jac81]

$$\vec{v}_d = \frac{\gamma m v_\parallel^2}{q_e} \frac{\vec{R} \times \vec{B}}{R^2 B^2}, \tag{4.4}$$

with the vector $\vec{R}$ of the electron trajectory from the toroid center, the electron charge $q_e = -e$ and the relativistic $\gamma$ parameter. The resulting drift velocity $\vec{v}_\mathrm{d} = (0, v_y, 0)$, with

$$v_y = \frac{\gamma m v^2}{eRB}, \tag{4.5}$$

is proportional to the kinetic energy $E_\parallel$ of the electrons. The absolute drift displacement of the electron orbit can be obtained by a numerical approximation [Ley97],

$$\Delta y_\mathrm{Tor}[\mathrm{mm}] = 0.58 \frac{\theta[^\circ]\sqrt{E[\mathrm{eV}]}}{B[\mathrm{Gauss}]}. \tag{4.6}$$

For the geometry in the electron target at 0.04 T this means for the drift in one single 90° toroid, i.e. the displacement in the interaction section,

$$\Delta y_\mathrm{Tor}[\mathrm{mm}] = 0.1305\sqrt{U_0[\mathrm{V}]}, \tag{4.7}$$

with the accelerating voltage $U_0$.

The consequence of this drift is that the electron beam axis is moving during energy scans. For large energy jumps this could result in partial or complete loss of overlap of the electrons with the ion beam and is fatal for the determination of absolute rate coefficients. Another consequence is that, even in the range where the overlap is still retained, the energy calibration is wrong due to the parabolic $r$ dependence of the space charge potential (section 2.4.2). The analysis of the experimental data assumes that the ion beam is located in the center of the electron beam. A displacement out of the center violates this assumption and contributes as an energy-dependent error to the final relative energy. To gain highest precision the overlap should be retained as precisely as possible.

With the movable retarding field analyzer in the collector section one measures transverse density profiles from which the absolute beam position is determined (see

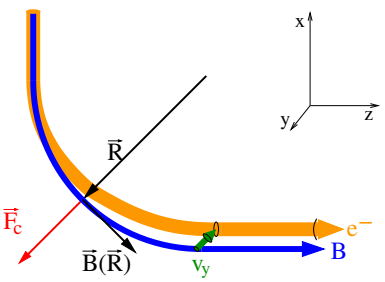


**Fig. 4.10:** *In the restframe of the electrons a centrifugal force $\vec{F}_c$ is seen along the direction of the $\vec{R}$-vector. The Lorentz force translates this into a drift $v_y$, perpendicular to the toroidal plane.*

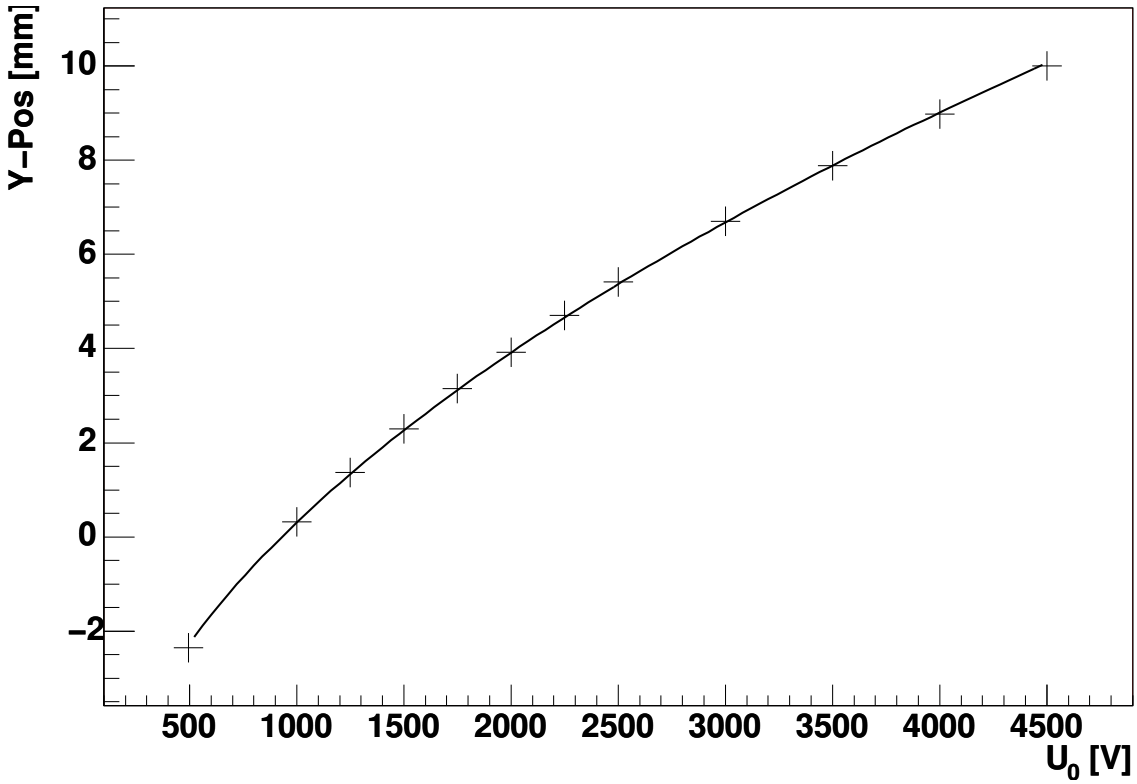


**Fig. 4.11:** *Measurement of the toroidal drift dependence on the electron acceleration potential $U_0$. The electrons were produced in the gun section of the electron target and bent by the two 90° toroids. The deviation from the original position was measured by the retarding field analyzer. The markers are measured values, the solid line is a fit with (4.6) for $\theta = 180°$*

section 4.2). For different electron kinetic energies the toroidal drifts are obtained as shown in Fig. 4.11. A fit (solid curve) with equation (4.6) and $\theta = 180°$, $B = 400$ Gauss agrees well with the observed drift. This data allows us to implement a compensation system.

Steering coils in all sections of the electron target can move the electron beam position. These coils add an field component perpendicular to the guiding magnetic field and tilt the electron beam axis approximately linear to the steering field [Spr03]. The most obvious choice to apply a lever to the drift compensation would be the vertical steering coils in the merging toroid itself. However, this would impose a fluctuating magnetic field onto the ion beam and produce undesired effects on the beam overlap. The most promising lever for compensation lies ahead of the merging toroid, in the acceleration section.

The beam overlap can be restored after small energy jumps by appropriate static correction applied via the control system. Such a system is, however, inflexible and error-prone and a safe automatic stand-alone solution is preferable. A measurement of the electron beam position in the interaction section is possible by the pickup electrodes, but they are sensitive to amplitude-modulated beams only. Thus, to set up closed loop position regulation is not possible. However, the verified drifting behavior described by

equation (4.7) allows us to implement a compensation system applying a feed-forward correction after careful calibration.

The steering field $|\vec{B}_y|$ is proportional to the electric current $I_{Ay}$ through the steerer coils. The steering power supply has a resistive control input and the output current is proportional to the input control voltage. Thus

$$\Delta y_{Ay} \propto U_{Ay}. \tag{4.8}$$

The compensation system modifies the control input $U_{Ay}$ to the "Acceleration Y" steerer power supply depending on the acceleration potential of the electron beam $U_{\mathrm{cath}}$ to establish the required displacement of the electron beam.

For computing the size of the compensation an analog electronics module has been developed in collaboration with Oliver Koschorreck, MPI-K. The detailed electronic layout of the drift compensation module is attached in Appendix B, Fig. B.1. The input signal to this module is the measured cathode voltage $U_{\mathrm{cath}}$. Since the data acquisition setup already uses a frequency-coded cathode voltage measurement which transfers a signal to ground potential, this signal ($f(U_{\mathrm{cath}}) = 50\frac{\mathrm{Hz}}{\mathrm{V}} * U_{\mathrm{cath}}$) is branched off to the compensation system. A Voltage-to-frequency converter chip (VFC32) translates the frequency signal back to an analog voltage signal $U_{\mathrm{VFC}} \propto U_{\mathrm{cath}}$. Using an analog multiplier/divider chip (Burr-Brown MPY100) the square-root $U_{\mathrm{sq}} = \sqrt{U_{\mathrm{VFC}}}$ is calculated. Various operation amplifiers adjust the polarity and gain of the MPY100's output voltage $\Delta U_{\mathrm{comp}} \propto U_{\mathrm{sq}}$ and add it as an offset onto the control value of the steerer magnet's power supply. The gain factor $\epsilon$ can be adjusted from the module's front panel by a potentiometer and a voltage inversion switch. This correction signal is added on top of the seeded steerer control signal from the EUNet system. The compensation can be expressed by

$$U_{Ay} = U_{Ay}^{\mathrm{EUNet}} + \underbrace{\epsilon \cdot \sqrt{U_{\mathrm{cath}}}}_{=\Delta U_{\mathrm{comp}}} \tag{4.9}$$

The gain factor $\epsilon$ has to be derived and calibrated experimentally.

The displacement of the electron beam $\Delta y_{Ay}$ has to be calibrated to compensate the toroidal drift $\Delta y_{\mathrm{Tor}}$

$$-\Delta y_{\mathrm{Tor}} \stackrel{!}{=} \Delta y_{Ay}. \tag{4.10}$$

As one can see from equation (4.6), the required displacement depends on the strength of the magnetic guiding field $\vec{B}$. On the other hand, the displacement $\Delta y_{Ay}$ in the acceleration Y steerer depends on the guiding field as well. The tilting of a magnetized electron beam by an angle $\alpha$ is

$$\tan\alpha = \frac{|\vec{B}_y|}{|\vec{B}_z|} = \frac{\Delta y_{Ay}}{l}, \tag{4.11}$$

with the length of the acceleration section $l$, a steering field $\vec{B}_y$ in y-direction and a magnetic guiding field $\vec{B}_z$ in the z-direction. With the equation (4.6) and (4.11) one

obtains

$$\frac{|\vec{B}_y|}{|\vec{B}_z|} \cdot l = -0.58 \frac{\theta\sqrt{U_{\text{cath}}}}{B_z}. \tag{4.12}$$

From this one can get the required steering field strength $B_y$,

$$B_y = 0.58 \frac{\theta\sqrt{U_{\text{cath}}}}{l}. \tag{4.13}$$

This important result means the required steering field for correction of the toroid drift does not depend on the strength of the magnetic guiding field, as the guiding field dependencies of the toroid drift (equation 4.6) and the steering in the acceleration section (equation 4.11) cancel out each other. Thus one can safely rely on a static calibration of the gain factor $\epsilon$ for the compensation system for all magnetic guiding field strengths.

The gain factor $\epsilon$ has been determined experimentally using the following procedure. The most precise electron beam position measurement is possible with the movable retarding field analyzer. With disabled compensation system the electron beam was aligned to the center of the collector cup at $U_{\text{cath}} = 1000$ V. Then the acceleration potential was ramped up to $U_{\text{cath}} = 4000$ V and the electron position was measured again. A vertical displacement of the electron beam is observed, which contains the contributions of both toroidal sections for merging and demerging. The compensation system is installed afterwards and the gain is varied until the electron beam position is displaced vertically by exactly half of the uncorrected amount. At this condition the electron beam position in the interaction section is independent of the electron energy, which can be verified with the position pickup electrodes on both ends of the interaction section. The remaining electron energy dependence stems from the demerging magnet and does not affect the overlap of the electron beam and the ion beam.

Once the compensation system is adjusted the gain factor can be determined to $\epsilon = 2.8928 \cdot 10^{-2}\ \sqrt{\text{V}}$. The output signal of the compensation system $U_{Ay}(U_{\text{cath}})$ (taken with $U_{Ay}^{\text{EUNet}} = 0$) shows the desired square-root dependence on the cathode voltage (Fig. 4.12).

The drift compensation module has been designed to adapt to voltage jumps on a timescale of one millisecond, which is within the typical 5 ms waiting time the data acquisition system performs. The operation range has been designed to cover the interval from 50 kHz to 500 kHz (corresponding to 1 kV to 10 kV) and covers the usual range used in DR measurements on atomic ions. It is limited by the frequency to voltage conversion.

A demonstration of the compensation system has been achieved for the first time in a beamtime on dielectronic recombination on hydrogen-like $Mg^{11+}$. DR resonances in this system start at about 1000 eV relative energy and require a strong detuning of the electron target energy from cooling conditions. The electron-ion beam overlap was adjusted at cooling energy ($eU = 1847.6$ eV). The scans for DR resonances were performed in the range of 5 keV to 8 keV. The steering coils have been controlled by the automatic system and not tuned manually in between. The results of this measurement will be discussed in section 5.2.

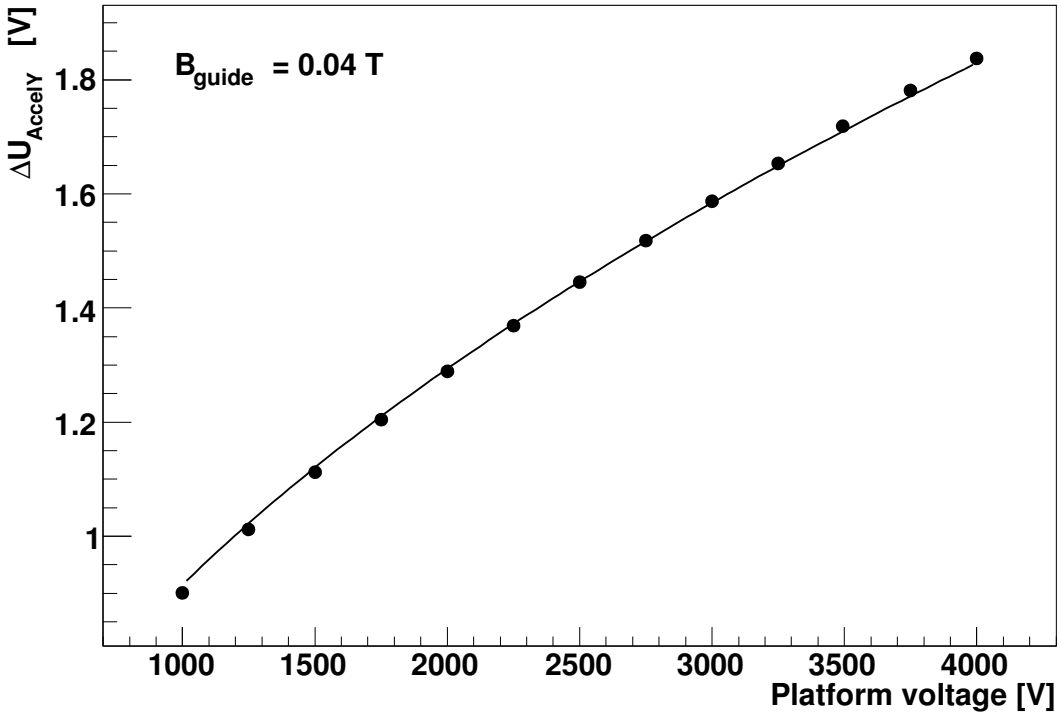


**Fig. 4.12:** *Calibrated correction $\Delta U_{Ay}$ at a magnetic guiding field of $B_{\text{guide}} = 0.04$ T. The gain factor $\epsilon$ in (4.9) is derived from a fit to the data points with $\Delta U_{Ay} = \epsilon \cdot \sqrt{U_{\text{cath}}}$ and $\epsilon = 2.8928 \cdot 10^{-2}$ $\sqrt{\text{V}}$.*

## 4.5 Energy stability

The energy precision during scans of resonances is not only subject to the internal energy spread of the electron beam but also to variations of the external acceleration voltage and emission conditions at the cathode. Random fluctuations merely broadening the resonance resemble an artificial increase of the electron beam temperature. In addition, systematic shifts in particular of the electron energy can affect the resonance positions. The most critical in this context are the stability of the involved power supply that generates the voltage of the HV platform and electron beam density fluctuations.

### 4.5.1 Slew rate of the HV platform

A principal limit for the timescale on which voltage jumps may be performed stems from the design of the high voltage platform, as it represents an RC element. The kinetic energy of the produced electrons is adjusted by the voltage of the HV platform, $E_{\text{kin}} = eU_{\text{platform}}$ and space charge corrections. However, the resistivity of the platform is not a fixed value and depends on the loss current (reflected electrons, collector water cooling circuit, etc.).

An estimate of the slew rate for the potential can be obtained from measurement. For this measurement the platform was set to a voltage of 1000 V. From this base voltage short jumps to a voltage of 1820 V were performed. After a variable delay

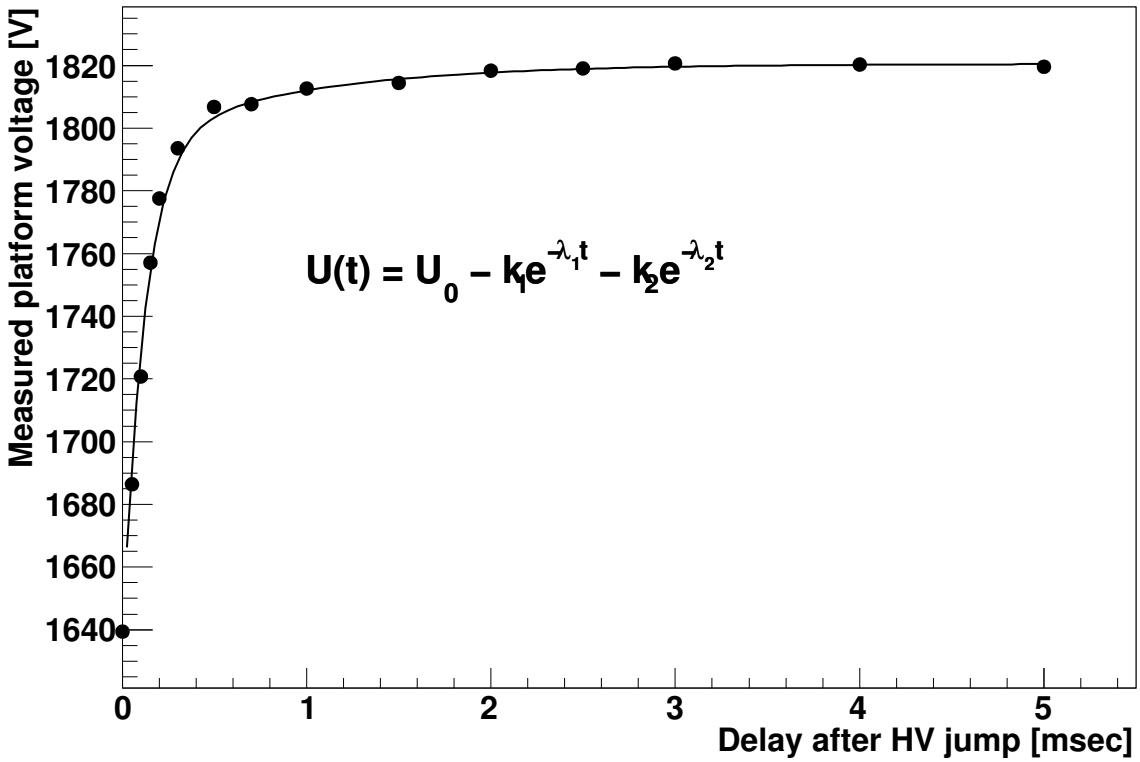


**Fig. 4.13:** *Slew rate of the HV platform. Filled circles: measurement. Solid curve: fit with coefficients* $k_1 = 160(1)$ V, $\lambda_1 = 8.4(1)$/ms, $k_2 = 25(3)$ V, $\lambda_2 = 1.1(1)$/ms.

the platform voltage was measured. The voltage measurement is established by a voltage divider which translates the platform voltage into digital pulses with frequency coding (section 4.1). The pulses from its VFC are counted for one millisecond. The results of these measurement are the markers in Fig. 4.13. An acceptable minimum delay time $t_\mathrm{d}$ is estimated when the energy deviation is below the thermal energy spread of the electron beam ($\approx k_B T_\mathrm{cath}$). For the $\Delta U = 820$ V jumps done here one finds $t_\mathrm{d} = 4$ ms for an electron beam produced by the thermionic cathode. The observed time-dependent voltage shows two contributions. One being the behavior of the Giessen voltage divider itself, and one stemming from the HV platform as an RC element, hence the double-exponential behavior. It is obvious that the deviation from the desired voltage depends on the voltage step size and is smaller for shorter $\Delta U$ jumps.

The impact on the energy resolution could be demonstrated clearly in a measurement (Fig. 4.14) [Buh06]. The specific wobble cycle was to perform steps in the order of cooling, reference, measurement with a cooling energy of $\approx 951$ eV. The platform voltage for the reference step was $\approx 194$ V higher and the measurement voltage was varied between 951 and 961 V. So the transition from the reference step to the measurement step means a reduction of the platform voltage. After 1 ms delay time, the platform voltage is still above the desired value and the electrons kinetic energy creeps during first few moments of the measurement step towards its final value. Thus one observes a washing-out of the peak structures towards lower energies and one understands the

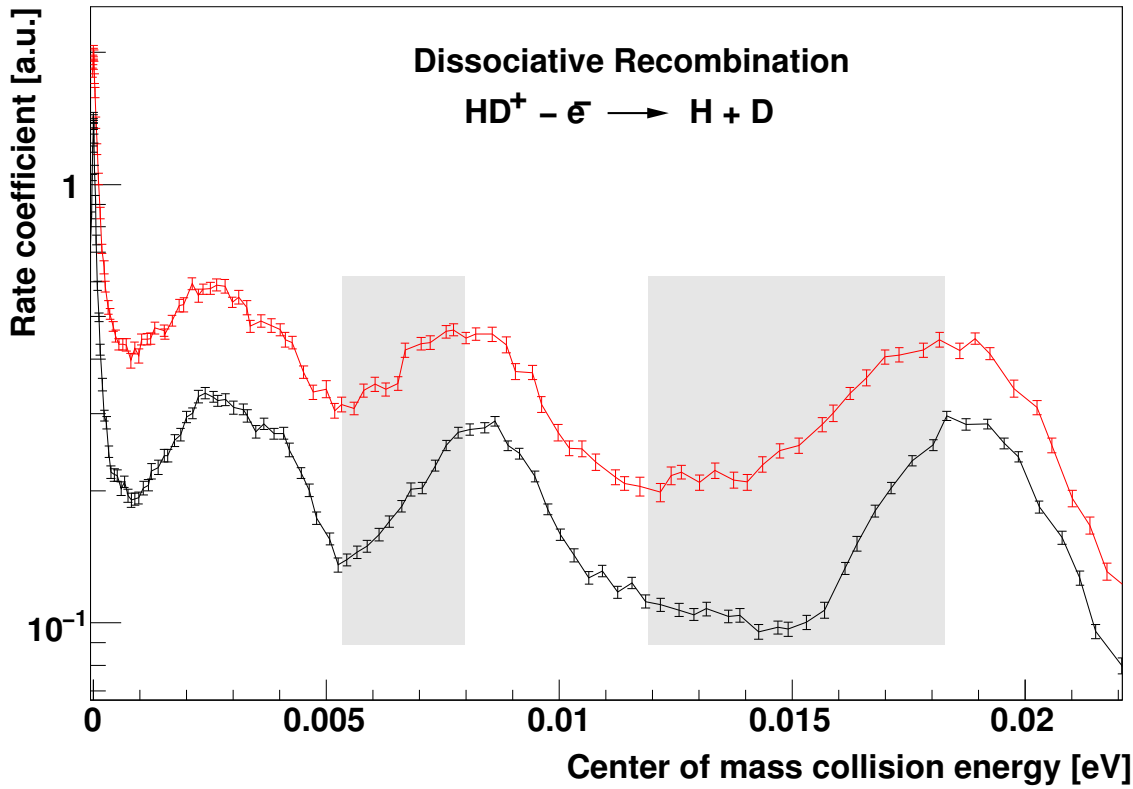


**Fig. 4.14:** *In a measurement of Dissociative Recombination in $HD^+$ [Buh06] using an electron beam from the photocathode the impact of different delay times after voltage jumps is clearly visible (shaded areas). The delay time after voltage jumps was 1 and 5 ms for the red and black curve, respectively and identical conditions else.* $E_{\mathrm{cool}} =$ 951 eV.

difference between both spectra qualitatively.

### 4.5.2 Electron beam density fluctuations

The electron density couples to the energy precision by its influence on the space charge correction (section 2.4.2). Depending on the two types of cathodes used, the stability in the measurements depends on different factors.

**Photocathode** The emission current varies through laser power fluctuations and the aging of the cesation layer. For the diode laser used, the laser emission power is well controlled by the stabilized current supply. Over longer intervals the electron emission current of the cathodes is tightly monitored. It shows stable characteristics on the timescale of a single run ($\approx$ 2 hours). Towards the end of the lifetime of a cathode sample the emitted current starts to degrade quickly. Such a cathode is replaced by a newly prepared sample.

**Thermionic cathode** The thermionic cathode is heated by a remote controllable AC power supply. Observations of this heating power supply show a variation of

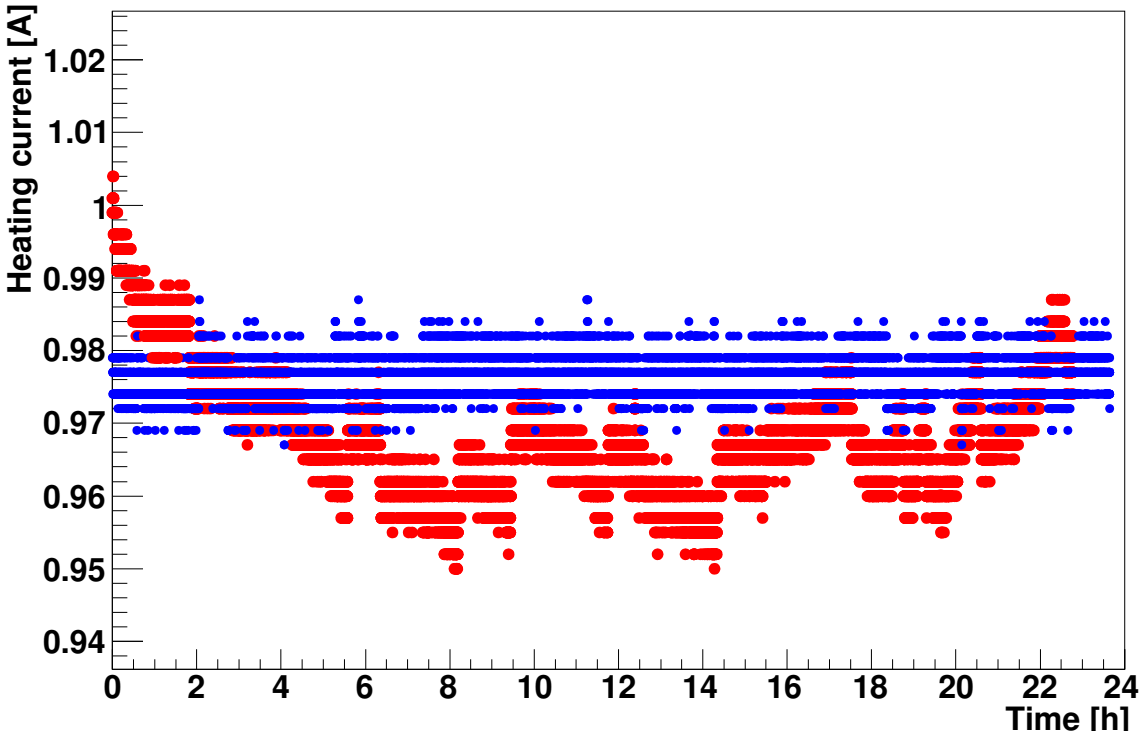


**Fig. 4.15:** *Long-term stability of the cathode heating with inactive (red) and active (blue) software stabilization system.*

the heating current on a timescale of few minutes. The origin of these fluctuations is probably found in temperature fluctuations of the electron targets HV cage housing this cathode heating power supply. The variations entail changes of the electron current on a level of a few percent. While the electron current is recorded by the data acquisition system (section 3.3), and one could in principle correct for these fluctuations in the offline analysis, this is usually a cumbersome and error-prone process.

In a first approach to assure constant conditions the DAQ software system was enhanced to implement a electron current monitoring system, which automatically stops the currently running measurement if the electron current is out of bounds. This assured constant electron current within one run. Though, if the worst comes to the worst this means the DAQ is stopping frequently and piles up large amounts of mostly unusable experiment runs with insufficient statistics for precise calibration.

To stabilize the AC power supply for the cathode heating an adaptive software servo system was created. It compares the actual heating current with the start value and acts on deviations by adjusting the desired value until the actual value is achieved again. The heating powersupply is connected to the EUNet system (section 3.3) and the actual heating current of typically $I_{\mathrm{heat}} \approx 1250$ mA is read with a digital resolution of 4.88 mA by a 12 bit digital to analog converter (DAC). If the heating current changes by more than two bit-values from the original, the control voltage is stepped up or down by a small $\Delta U$ respectively, to compensate the runaway heating current. Fig. 4.5.2 shows the heating current, measured for 24 hours, once without heating stabilization and once with the stabilization system actively controlling the heating current. It is

clear, that the long term variations are eliminated by the system.

# Chapter 5

# Electron collision spectroscopy

## 5.1 Hyperfine resolved DR resonances in Li-like $Sc^{18+}$

The former experiment on dielectronic recombination in lihtiumlike $Sc^{18+}$ [KSS+04] allowed identification of an isolated DR resonance $2p_{3/2}10d_{3/2})_3$ at around 0.068 eV. Such isolated near-zero resonances are valuable candidates for the determination of the $2s-2p_j$ splitting, as has been discussed in section 2.3.2. With this the $2s-2p_{3/2}$ splitting could be derived to 44.3107(19) eV and represented a reduction of the uncertainty by more than an order of magnitude to the thitherto most precise value from optical spectroscopy in a tokamak plasma [SCC+80].

The meanwhile improved setup at the TSR with a dedicated electron target and a cryogenic GaAs electron gun allows to achieve ultracold conditions and eliminate transient effects. This increases the precision of the resonance energy determination and allows to resolve the hyperfine splitting of the $2s$ ground state of the $^{45}$Sc ($I = 7/2$) parent ion. Radiative screening corrections to the $2s - 2p_{3/2}$ splitting will be extracted from the measured data.

### 5.1.1 Experiment

$^{45}Sc^{18+}$ ions have been produced at the Max-Planck-Institut für Kernphysik tandem accelerator facility and injected into the TSR at a kinetic energy of 177 MeV, corresponding to $v_{\mathrm{ion}} = 9.15\%$ speed of light.

The stored ion beam was overlaid by two electron beams. The electron cooler was tuned to constant cooling conditions. The acceleration voltage of the electron beam in the cooler was 2340.4 V at a beam current of 119 mA and expansion $\xi_{ecool} = 9.6$ (electron density $n_{\mathrm{e,ecool}}$ of $4 \cdot 10^7/\mathrm{cm}^3$). With a space-charge correction of 188.2 V this corresponds to a cooling energy of the electron beam of $E_{\mathrm{ecool}} = 2152.2$ eV.

The target produced an electron beam from a cryogenic GaAs photocathode [OSL+05], cooled with liquid nitrogen to a temperature of $k_B T_{\mathrm{cath}} \approx 100$ K. The extracted electron currents were of the order of $\approx 180$ $\mu$A. With a magnetic field strength in the gun region $B_{\mathrm{gun}} = 1.6$ T and a guiding field strengh $B_{\mathrm{guide}} = 0.0576$ T an expansion

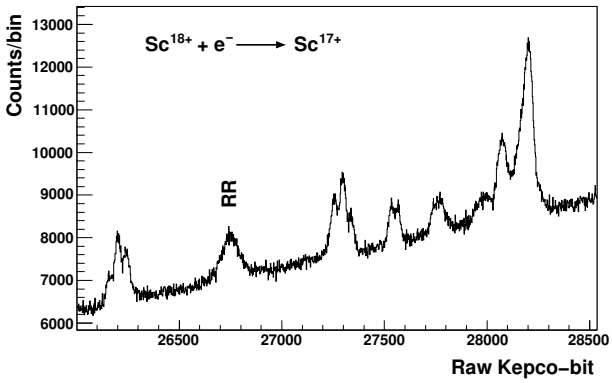


**Fig. 5.1:** *Accumulated $Sc^{18+}$ raw spectrum. The scanned energy range corresponds to $-0.04$ eV on the left to 0.4 eV on the right. The scan direction has been from top to bottom. The decrease of the background level observed from right to left corresponds to the ion beam decay.*

ratio set to $\xi_{tgt} = 27.78$[1] was set. At these conditions one finds an electron density of $n_{e,tgt} \approx 2 \cdot 10^5/\mathrm{cm}^3$. To eliminate relative drifting of the platform voltages of both electron beam devices with regard to each other, the platforms of both devices have been connected to the same base potential. On top of this base potential the fast Kepco HV amplifier has been installed to allow variation of the probe beam's electron energy.

After injection the ion beam was cooled for three seconds by the electron cooler. During this time the electron target was set to the start value of the following measurement scan.

For the energy scan the electron target energy was ramped linearly in 1280 steps of 10 msec from 2212 V to 2133.9 V. This corresponds to aproximately +0.4 eV to $-0.04$ eV energy range in the cm frame (2.7). No cooling- or reference-steps had been interleaved, to maximize the duty-cycle. Also, since the relative voltage jumps between each step was very small ($\Delta U = -0.06104$ V) the influence of the slew-rate was estimated to smear out the obtained spectra by less than one binwidth. In order to maximize the duty-cycle the slew-rate contribution was therefore ignored and the next acquisition step started immediately after setting the next voltage level, without additional waiting time in between.

### 5.1.2 Data reduction

The measured raw detector counts $D$ have been sorted into histograms, according to the measurement bit of the scanning HV-amplifier (see Fig. 5.1). These have been normalized with the accumulated time $t$, spent at each bit, the calibrated ion current $I_{\mathrm{ion}}$, and the length-ratio of TSR $L$ and the electron target overlap region $l$:

[1] In fact the experiment was carried out with a miscalibrated magnetic guiding field in the interaction section. Originally an expansion ratio $\xi_{tgt} = 40$ at a magnetic guiding field strenght of $B_{\mathrm{guide}} = 0.04$ T was chosen. However, due to a typing error in the calibration of the interaction solenoid magnet calibration, the magnetic field strength was locally set to 0.0576 T in the interaction section, while all other sections were indeed set to $B_{\mathrm{guide}} = 0.04$ T. This results in a compression of the electron beam inside the interaction section to an effective expansion ratio of $\xi = 27.78$. This has been accounted for in the data reduction steps and is silently implied in the following.

$$R_{\text{ion}}^{\text{full}} = \frac{D}{tI_{\text{ion}}}\frac{L}{l} \tag{5.1}$$

The observed ion rate $R_{\text{ion}}^{\text{full}}$ is the sum of three components,

$$R_{\text{ion}}^{\text{full}} = R_{\text{ion}}^{\text{back}} + R_{\text{ion}}^{\text{DR}} + R_{\text{ion}}^{\text{RR}}, \tag{5.2}$$

where $R_{\text{ion}}^{\text{back}}$ originates from the nonresonant electron capture of stored ions from rest-gas atoms, and $R_{\text{ion}}^{\text{DR}}$ and $R_{\text{ion}}^{\text{RR}}$ are the contributions from dielectronic and radiative recombination, respectively. Since the Photocathode electron beam is very weak the vacuum conditions are independent of the electron beam kinetic energy and a constant background $R_{\text{ion}}^{\text{background}}$ can be assumed.

From this Ion rate $R_{\text{ion}}^{\text{full}}$ the background is subtracted by fitting $R_{\text{ion}}^{\text{full}}$ in the energy range $\geq 2204$ eV, corresponding to c.m. energies of $\approx 0.3$ eV, for which no structure is predicted by the theory calculations. $R_{\text{ion}}^{\text{full}}(E \geq 0.3) = 5.595(7)\text{s}^{-1}$ is obtained. A small contribution from RR is still present and need to be considered. With the Bethe-Salpeter formula (equation 2.2) one obtains $R_{\text{ion}}^{\text{RR}} = 0.010\text{s}^{-1}$. With (5.2) one obtains $R_{\text{ion}}^{\text{back}} = 5.585(10)$. This background contribution is then subtracted from the spectrum at all energies.

The rate coefficient $\alpha$ is now obtained by normalization with the electron density,

$$\alpha = \frac{R_{\text{ion}}}{n_e}. \tag{5.3}$$

**Electron density**

The current density of electron beams produced from a photocathode are not homogeneous. Fig. 5.2 shows a 2d-cut through a measured profile. One finds a fall-off towards the edges of the electron beam. This fall-off is caused by the Pierce-shield, surrounding the cathode. A strong repulsive setting was required to eliminate blind currents from the cathode to the pierce-shield. The circle overlaid on the current density profile indicates the size of a geometrically expanded electron beam with a flat-top distribution. Instead one finds a beam profile with soft fall-off towards the edges. The shape of the profiles implies, that corrections to the density of the electron beam are necessary.

The shown profile can be parametrized by the function

$$g(r) = w \cdot \max\left\{0, \left(1 - \frac{Fr}{R'}\right)^4\right\} \tag{5.4}$$

with the constant weight $w$, the fitted flank parameter $F = 0.637$ mm and

$$R' = \frac{FR}{\sqrt[4]{1/2}} \tag{5.5}$$

with the half-weight radius $R = 5.81$ mm.

The easiest solution to account for the correct density in the data reduction process is to retain the assumed flat-top distribution with a modified beam radius $r_{eff}$. This

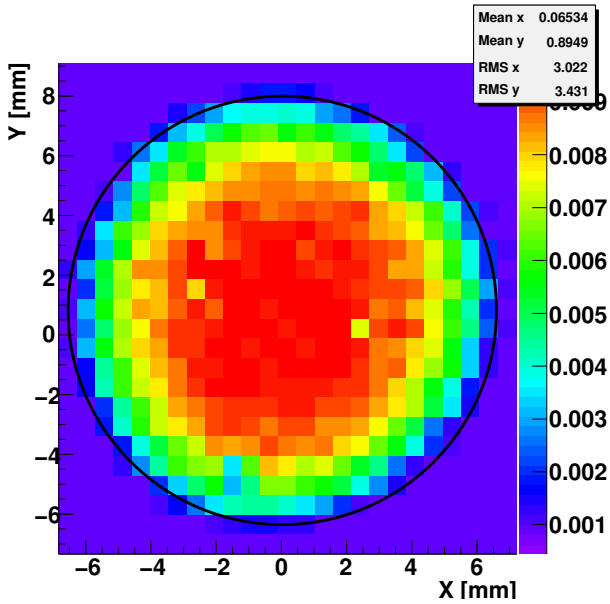


**Fig. 5.2:** *Transverse 2d cut through a typical photo-cathode electron beam expanded with $\xi = 20$ (cathode diameter $d_{\mathrm{cath}} = 3$ mm). The profile was obtained by scanning the beam with the steering magnets in the collector section across the the retarding field analyser. The overlaid circle indicates the expected size of a geometrically expanded electron beam.*

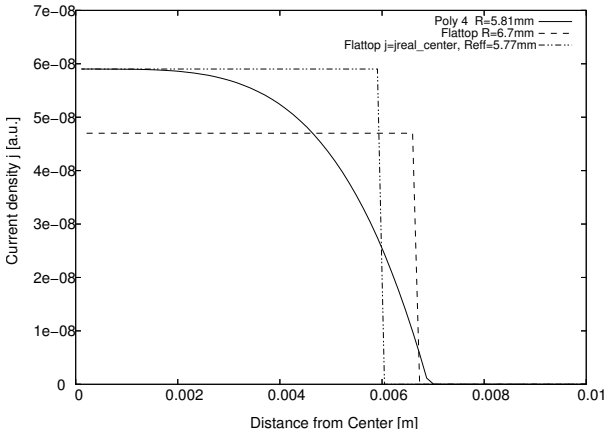


**Fig. 5.3:** *Comparison of density profiles for different distributions with same total electron current. The fitted profile (solid line) from equation (5.4) in comparison to the geometric flat-top profile (dashed line). A simple modification to the flat-top beam radius corrects the density in the center (dash-dotted line) to match the value of the fitted profile.*

is achieved by reducing the cathode radius geometric $r_{\mathrm{cath}} = 1.5$ mm to the effective cathode radius $r_{\mathrm{cath,eff}} = 1.29$ mm. Fig. 5.3 shows the fitted, geometric and modified radial electron density distributions.

An important question is how the modified current distribution impacts on the spacecharge corrections (section 2.4.2). A numerical calculation of the spacecharge of all three distributions (the fitted, geometric flat-top and modified flat-top) can shed some light on this issue. The calculated results for cooling energy $E_{\mathrm{cool}} = 2155.34$ eV (Fig. 5.4) prove a dependency of the spacecharge potential on the used electron distribution model. A clear deviation between the three models is shown. Especially between the *real* fitted distribution and the modified flat-top distribution one finds a difference of $\approx 0.025$ V. This difference is however easily correctible. More important however is the energy dependency of this difference. This can also be clarified by a numerical calculation. The spacecharge in the center of the beam has been calculated for the scanned energy range. The results are shown in Fig. 5.5. The curves for the three considered models are almost parallel. Nevertheless, the relative potential difference over the scanned energy range is not constant and changes by 0.005 eV within the

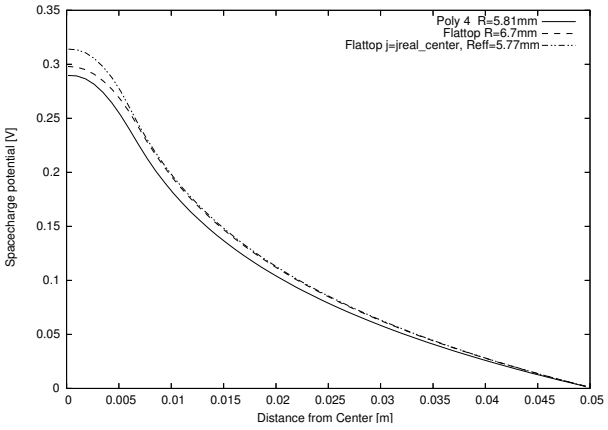


**Fig. 5.4:** *Radial dependency of the spacecharge potential . One finds different spacecharge potentials for the fitted, geometric flat-top and modified flat-top profiles.*

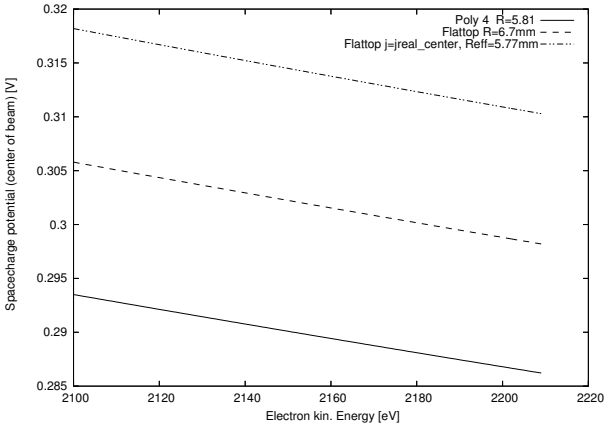


**Fig. 5.5:** *The spacecharge potential in the center of the electron beam is shown as a function of the electron energy. The three curves show a nearly parallel behaviour with constant relative offsets over the whole energy range. The deviation from a constant offset is* $< 0.005$ *V.*

scanned energy range. However, this is small and will be neglected in the following.

### Ion beam energy determination

The conversion to the center-of-mass frame requires a precise knowledge of the laboratory energy of the ion beam, which corresponds to the electron energy at cooling conditions ($E_{\mathrm{cool}} = \frac{m_e}{m_{\mathrm{ion}}} E_{\mathrm{ion}}$). Naturally, this is within the range of the maximum of the RR, which peaks at zero relative energy. As one can see from Fig. 5.1, the broad structure of the RR peak cannot be used very accurately to define lab energy, where the ion beam velocity is matched. A more sensitive method to the precise value of the cooling energy is achieved by mirroring the low-energic side ($v_e < v_{\mathrm{ion}}$) of the spectrum ontop of the high-energy side ($v_e > v_{\mathrm{ion}}$). By tuning the laboratory value of the cooling energy one can bring distinct structures into overlap by the experimenters eye. With this method a sensitivity of $\Delta E_{\mathrm{cool}} \approx 0.02$ mV to the cooling energy $E_{\mathrm{cool}}$ is achieved.

A laboratory electron energy at cooling has been determined to $E_{\mathrm{cool}} = 2155.34(2)$ eV. This is higher by 3 eV than the the value derived from the calculations for the electron cooler. Plausible reasons for this are to be found in the spacecharge potential of the electron cooler. The spacecharge potential shows a parabolic fall-off from $\Phi_c = 188.2$ V at the center to $\Phi_s = 149.2$ V on the surface of the electron beam envelope (equation 2.18). A slight misalignment of the ion beam axis out of the center of the electron beam axis leads to an error of the spacecharge correction. Another thinkable contribu-

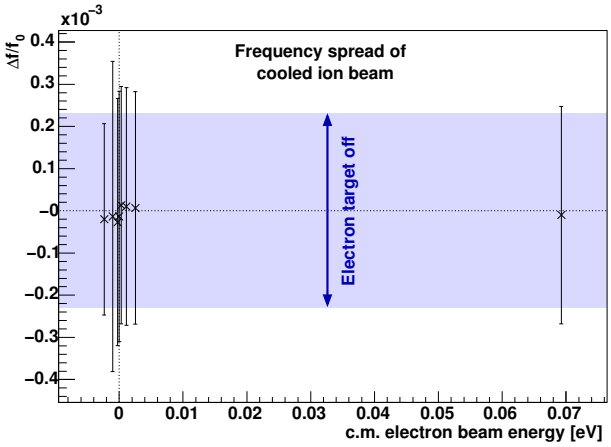


**Fig. 5.6:** *The ion beam revolution frequency is recorded in dependency of the detuning energy of the electron target. The electron target has been set statically to relevant detuning energies for each data point. The bars indicate the $\pm 1\sigma$-spread of the recorded frequency signal. The shaded area indicates the frequency spread of the ion beam merged with the electron cooler at fixed energy only.*

tion to this deviation is the accumulation of positive ions in the spacecharge potential. Since the electron density of the probe beam is much smaller, and thus the spacecharge corrections as well, similar effects are not expected for the electron target and will be considered in the error balance for the experimental energy determination.

### Ion beam energy dragging

[KSS+04] reported the largest uncertainty to the energy scale was the ion beam energy dragging. It is caused by the non-linear cooling force of the probing electron beam (equation 2.20, see also Fig. 2.6). At near zero relative energies this force is strongly attractive and pulls on the ion beam velocity to match the electrons.

The dragging influence of the probing beam can be suppressed in the enhanced setup, as has been discussed in section 2.5. This setup allows to establish continous electron cooling of the ion beam. This fixes the ion beam velocity to the cooling electrons. A low-density probing beam from the electron target applies only a very weak distortion to the cooling force. Systematic measurements of the ion beam revolution frequency allow to estimate the contribution from the additional cooling force. For static settings of the electron energy in the cooler and target sections the Schottky noise signal has been analyzed. The results have been summarized in Fig. 5.6. The shaded area indicates the width of the frequency profile of the ion beam cooled with the electron cooler and switched off electron target. The markers represent the measured average frequency of the ion beam for a specific detuning energy of the electron beam (in the center-of-mass frame) and the bars represent the $\pm 1\sigma$-width of the frequency spread.

Indeed one finds a slight trace of ion beam energy dragging at very small relative energies. This is however far below the frequency spread of the undisturbed ion beam. At a relative energy of $\approx$ 68 meV, where the interesting resonance is expected one finds a frequency dsitribution which is in good agreement with the undisturbed one and constant ion beam energy can be assumed.

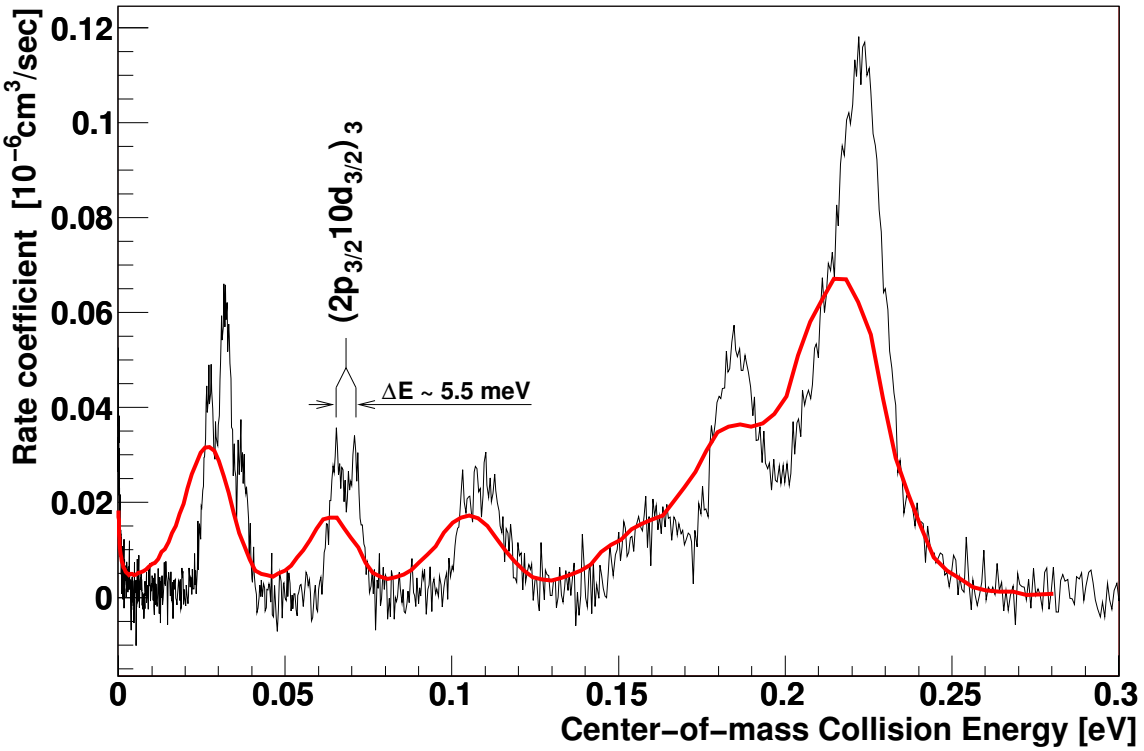


**Fig. 5.7:** $e^- + Sc^{18+}$ *rate coefficient as a function of the relative energy. The overlaid red curve shows the results of [KSS+04]. The black curve is the result of this experiment.*

### Toroid deconvolution

The electron target varies the electron energy by variation of the acceleration potential in the beam formation section. From this follows, that the electron beam is accelerated to full collision energy, when it is merged with the stored ion beam. Due to the finite size of the electron beam of typically $\approx 1$ cm the merging implies, that a during short distance of the merged beam path the electrons velocity vector $\vec{v}_e$ has a relative angle to the straight ion beam velocity vector $\vec{v}_i$. The resulting velocity difference $\vec{v}_d$ is non-zero in the merging section and in effect increases the collision energy.

With a map of the magnetic field directions along the path of the ion beam, obtained in a finite-element-method [Spr03], and the deconvolution method described in [LWH+96] one can remove the toroidal contributions.

## 5.1.3 Data analysis

With all the above considerations the final spectrum is obtained. Fig. 5.7 shows it in comparison with the former results [KSS+04]. The DR capture in the scanned energy range is mediated by the doubly excited states

$$Sc^{18+}(2s_{1/2}) + e^- \rightarrow Sc^{17+}(2p_{3/2}10l_j)_J. \tag{5.6}$$

The improved resolution allows observation of previously unresolved structure. The isolated $(2p_{3/2}10d_{3/2})_3$ resonance at around 68 meV splits up into two peaks, with a

| # | Configuration | Peak energy [eV] | Width [eV] | Strength $10^{-20}$ eVcm$^2$ |
|---|---|---|---|---|
| 1 | $(2p_{3/2}10d_{5/2})_4$ | 0.0289 | 0.0003 | 2909 |
| 2 | $(2p_{3/2}10d_{3/2})_2$ | 0.0337 | 0.0004 | 3211 |
| 3 | $(2p_{3/2}10p_{3/2})_0$ | 0.0342 | 0.0264 | 466 |
| 4 | $(2p_{3/2}10d_{3/2})_3$ | 0.0678 | 0.0004 | 2463 |

**Table 5.1:** *RMBPT calculations of the formed $Sc^{17+}$ DR resonances [KSS+04]*

separation of the maxima by $\approx 5.5$ meV and in the range of 30 meV new structure is seen as well.

From theoretical relativistic many-body perturbation theory (RMBPT) calculations in [KSS+04] four resonances in the energy range below 0.1 eV were identified (table 5.1). In total there are 65 different $(2p_{3/2}10l_j)_J$ configurations [KSS+04] in the energy range below 0.3 eV. However, all levels above 0.1 eV are in close neighbourhood to each other and have broad natural widths. It is questionable to identify individual lines and determine their resonance energy.

The splitting of the low-energetic peaks is explained by taking hyperfine interaction of the $^{45}$Sc nucleus ($I = 7/2$) into account. The initial state ($j = 1/2$) of the parent ion forms two hyperfine substates, $F = \{3, 4\}$. With $C = (F(F+1) - j_1(j_1+1) - I(I+1))$ and the interval factor $A$ one obtains the hyperfine terms as

$$\Delta E_F = C\frac{A}{2}. \tag{5.7}$$

For the $2s_{1/2}$ ground state the HFS splitting between both terms corresponds to $4A$. Calculations of the $2s_{1/2}$ ground state hyperfine splitting gave 6.0767 meV [BI00] or 6.0628 meV [SST97]. The statistical weights of the splitting terms are ($w_F = (2F + 1)/\sum_{F'} w_{F'}$) are $w_{F=3} = 7/16$ and $w_{F=4} = 9/16$.

**Fitting routine:** However, the hyperfine structure of the final state is a little more complicated. The $2p_{3/2}$ core interacts with the nuclear magnetic moment and forms the states $F' = \{2, 3, 4, 5\}$. The initial continuum level of the colliding electron is described as partial wave $\varepsilon l_j$ and one finds varying contributions for the possible partial waves [Lin06].

The resonance strength is then obtained by

$$S(F, K) = S(J) \cdot w_F \cdot \left( \sum_{j_2} (2K + 1)(2j_1 + 1) \begin{Bmatrix} I & j_1 & F \\ j_2 & K & J \end{Bmatrix}^2 \right) \tag{5.8}$$

with $K = 1/2, 3/2, \ldots, (I+J)$, the angular momentum of the initial $2s_{1/2}$ state $j_1 = 1/2$ and the continuum electron angular momentum $j_2$ (see Table 5.2, [Lin06]), the total angular momentum of the final state $J$ (see Table 5.1, [KSS+04]) the strength of the finestructure levels $S(J)$, and the initial $F = 3, 4$. The terms in braces are Wigner $6j$-symbols [Cow81].

| # | Resonance | Continuum state | Fraction |
|---|---|---|---|
| 1 | $(2p_{3/2}10d_{5/2})_4$ | $\varepsilon d_{7/2}$ | 1 |
| 2 | $(2p_{3/2}10d_{3/2})_2$ | $\varepsilon p_{3/2}$ | 0.84 |
| | | $\varepsilon d_{5/2}$ | 0.16 |
| 4 | $(2p_{3/2}10d_{3/2})_3$ | $\varepsilon f_{5/2}$ | 0.99 |
| | | $\varepsilon f_{7/2}$ | 0.01 |

**Table 5.2:** *Continuum partial waves of the incident electron [Lin06]*

The resonance energy is calculated by

$$\begin{aligned} E(J,F,K) =& E_J - \frac{A}{2}C \\ &+ \sum_{F'=2}^{5}\left[\frac{A'}{2}C' + B_{\text{quad}}\left(\frac{3}{4}\frac{C'(C'+1) - j_1'(j_1'-1) * I(I+1)}{2I(2I-1)J(2J-1)}\right)\right] \\ &\cdot (2F'+1)(2J+1)\cdot \begin{Bmatrix} I & j_1' & F' \\ j_2' & K & J \end{Bmatrix}^2 \end{aligned} \tag{5.9}$$

with the finestructure energy level $E_J$, $j_1' = 3/2$ the angular momentum of the $2p_{3/2}$ excited core electron, $j_2'$ for the final Rydberg state electron the interval factor of the $2p_{3/2}$ excited core $A'$ and $C' = (F'(F'+1) - j_1'(j_1'+1) - I(I+1))$, and the nuclear magnetic quadrupole moment $B_{\text{quad}} = 0.236(2)$ barn [MMM$^+$02].

With these, the acquired spectrum can be fitted in the energy range of 0.002 to 0.095 meV to obtain the experimental resonance energies and electron temperatures. In principle a statistical population of the parent ion hyperfine ground state levels should be present when the parent ions are produced in the accelerator stripping foils. But during a the storage time of several seconds the ions are exposed to 300°K background radiation and varyiong magnetic fields. Thus a variable population is allowed with independent ratios for the peak group around 30 meV (HFS weighting a) and the group at 68 meV (HFS weighting b). The strength is split by $S \cdot (1 - P_{\text{HFS}})$ for the $F = 3$ state and $S \cdot P_{\text{HFS}}$ for the $F = 4$ state.

**Fitting results:** The resonance number 3 has a broad natural linewidth and low strength. It is not fitted, but considered with theoretical parameters. The fitted resonance The convolution of the fitted theoretical resonances with the fitted electron temperatures is shown as blue curve in Fig. 5.8. The fitted parameters are summarized in Table 5.3.

The fitted transverse and longitudinal electron temperatures are higher, than expected. For an electron beam from a cryogenic cathode at $k_B T_{\text{cath}} = 100$ K at expansion $\xi = 27.78$ and a electron kinetic energy of 2155.34 eV one expects $k_B T_\perp = 0.310$ meV and $k_B T_\parallel = 4.302$ $\mu$eV.

The fitting routines don't consider the ion beam temperature and assume perfectly monoenergetic ions.

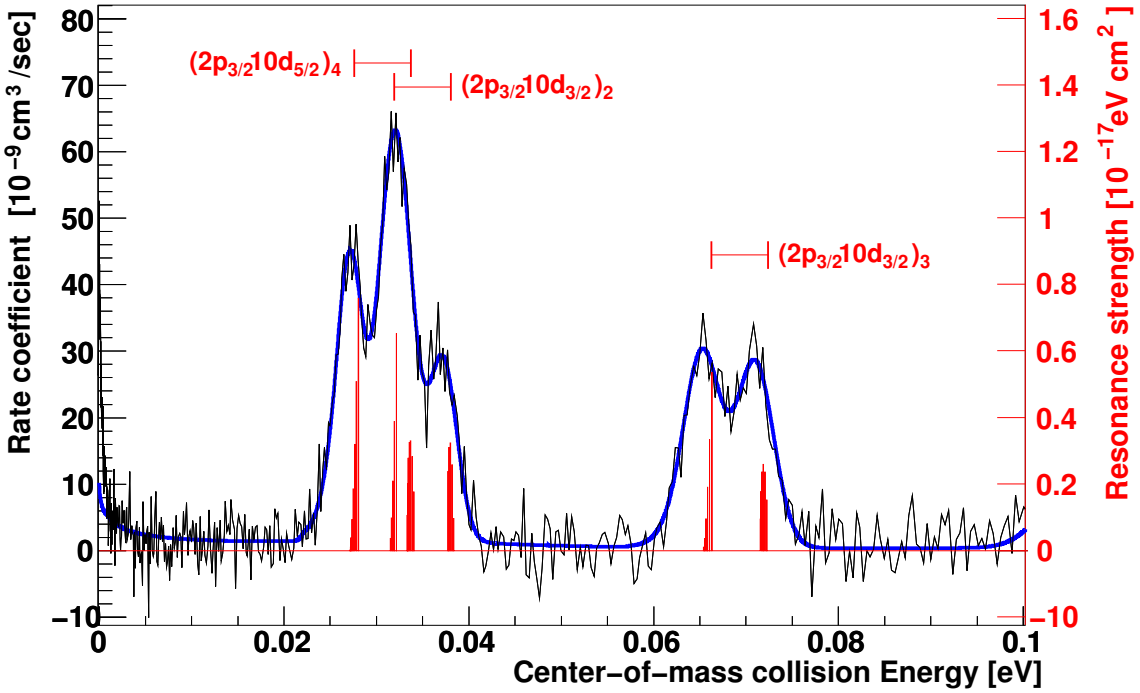


**Fig. 5.8:** *$Sc^{18+}$ fit results. The red sticks represent the fitted hyperfine resonances. The blue curve is the theoretical rate coefficient, convoluted with fitted electron temperature.*

| Parameter | | Value | Unit |
|---|---|---|---|
| Background offset | V | −1.035(150) | $10^{-9}$ cm$^3$/(s eV) |
| Background slope | V | 7.71(95) | $10^{-9}$ cm$^3$/(s eV) |
| Trans. electron temp. $k_BT_\perp$ | V | 1.103(1) | $10^{-3}$ eV |
| Long. electron temp. $k_BT_\parallel$ | V | 23.48(39) | $10^{-6}$ eV |
| HFS Interval factor | V | 0.001553(1) | eV |
| HFS weighting a $P^a_{\mathrm{HFS}}$ | V | 0.5295(79) | |
| HFS weighting b $P^b_{\mathrm{HFS}}$ | V | 0.5094(130) | |
| Amplitude peak 1 | V | 3.625(65) | $10^{-17}$ eV cm$^2$ |
| Position peak 1 | V | 0.030360(34) | eV |
| Width peak 1 | F | 0.0003 | eV |
| Amplitude peak 2 | V | 2.621(62) | $10^{-17}$ eV cm$^2$ |
| Position peak 2 | V | 0.034610(4) | eV |
| Width peak 2 | F | 0.0004 | eV |
| Amplitude peak 3 | F | 4.66 | $10^{-18}$ eV cm$^2$ |
| Position peak 3 | F | 0.0342 | eV |
| Width peak 3 | F | 0.0264 | eV |
| Amplitude peak 4 | V | 2.367(51) | $10^{-17}$ eV cm$^2$ |
| Position peak 4 | V | 0.068600(85) | eV |
| Width peak 4 | F | 0.0004 | eV |

**Table 5.3:** *$Sc^{18}$ fit results. V: varied parameters, F: fixed parameters. Values in parentheses are statistical errors on the last significant digits.*

| | 1 $(2p_{3/2}10d_{5/2})_4$ | 2 $(2p_{3/2}10d_{3/2})_2$ | 4 $(2p_{3/2}10d_{3/2})_3$ |
|---|---|---|---|
| expt. Resonance-energy | 0.03036(1) | 0.03461(1) | 0.06860(9) |
| theor. Binding energy [Lin06] | 44.27916(20) | 44.27480(20) | 44.24071(20) |
| Expt. $2s_{1/2} - 2p_{3/2}$ trans. energy | 44.30952(20) | 44.30941(20) | 44.30931(22) |

**Table 5.4:** *$Sc^{18+}$ $2s_{1/2}-2p_{3/2}$ transition energy determination from the fitted resonance positions. systematic uncertainties from Fig. 5.9*

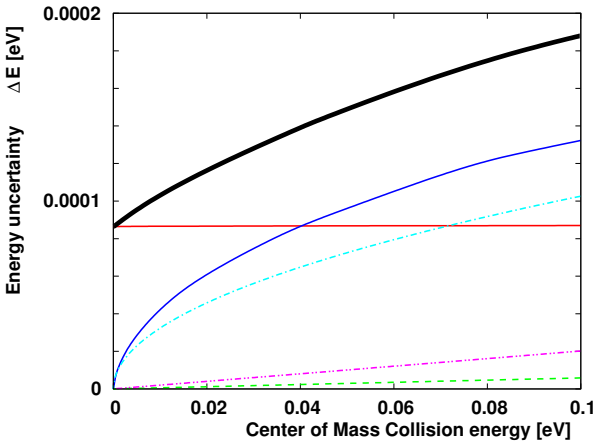


**Fig. 5.9:** *$Sc^{18+}$ systematical uncertainties for the determination of the collision energy. Solid black curve: squared sum of all uncertainties. Red curve: merging angle ($\Delta\theta = 0.2$ mrad). Blue curve: determination of cooling energy by mirroring method (0.02 meV). Cyan curve: Absolute error of spacecharge correction (0.015 meV) Magenta curve: relative voltage precision ($10^{-4}$). Green curve: Absolute error of Cooling voltage measurement (0.125 meV)*

The determinations of the ion beam spread in section 5.1.2 has shown a spread of the ion beam momentum of the order of $\Delta f/f \approx \Delta p/p \approx 2 \cdot 10^{-4}$. This contributes to the longitudinal temperature.

**$2s_{1/2} - 2p_{3/2}$ transition energy:** With RMBPT calculations [Lin06] for the binding energy of the $10l_j$ Rydberg electron and the experimental resonance energies one can determine the $2s_{1/2} - 2p_{3/2}$ transition energy (see Table 5.4).

The results of the individual resonances are compiled into one common value, following the relation [BR91]:

$$E(2s_{1/2} - 2p_{3/2}) = \frac{\sum\limits_m E_m/(\Delta E_m)^2}{\sum\limits_m 1/(\Delta E_m)^2} \pm \frac{1}{\sqrt{\sum\limits_m 1/(\Delta E_m)^2}} \tag{5.10}$$

one obtains from the three individual resonances an error-weighted average $2s - 2p_{3/2}$ splitting energy of

$$E^{\text{expt}}(2s_{1/2} - 2p_{3/2}) = 44.30942(12) \text{ eV}, \tag{5.11}$$

with the statistical error on the last significant digits given in the parenthesis.

To estimate the systematical errors several components are taken into account.

- A skilled experimenter is able to align the beam overlap to 0.1 mrad.
  The magnetic guiding magnetic field in the interaction zone has been manufactured with a precision of 0.1 mrad [Spr03].
  The total uncertainty of the angle alignment is estimated to 0.2 mrad.

- The determination of the cooling energy by the *mirroring*-method is sensitive to 0.02 eV.
- The error of the spacecharge correction depends on how well the ion beam is placed into the electron beam center. It is estimated that this alignment has been established to be better than 2 mm. From Fig. 5.4 one reads a difference between the spacecharge potential in the center and a 2 mm displaced position of $\approx 0.01$ meV. The used electron beam density profile introduces a systematic error of the 0.005 meV over the whole scan range (Fig. 5.5). Thus a total error of the spacecharge correction of 0.015 meV is assumed.
- The instrument for the measurement of the cathode voltage has been calibrated with a relative precision of $10^{-4}$.
- The absolute error of the voltage measurement is estimated to 0.125 $V$.

The squared sum of the contributions is taken as a total systematical uncertainty for the following discussion. An energy-dependend overview of the contributions is shown in Fig. 5.9. All terms considered in the balance of the systematical errors contribute as a shift of the measured resonance energies. Hence, their sum directs into the same direction for all three resonances in Table 5.4. Therefore it is legitimate to take the average of the energy-dependent sum of the included systematics to specify the total systematical uncertainty for (5.11). For the resonance position of 68 meV one finds $\approx 0.16$ meV and for the two resonances close to 30 meV an uncertainty of 0.12 meV is assumed. With this the final result can be specified:

$$E^{\text{expt}}(2s_{1/2} - 2p_{3/2}) = 44.30942(12)(14) \text{ eV}, \tag{5.12}$$

The error in the first parenthesis is the statistical error, the second parenthesis is the averaged systematical uncertainty. The only explicit calculation of this transition in lithiumlike scandium for the $2s_{1/2} - 2p_{3/2}$ in lithiumlike scandium gave 44.307 eV [KBID91].

**Radiative screening corretions:** The results of a RMBPT calculations [KSS$^+$04] for the $2s_{1/2} - 2p_{3/2}$ transition gives 44.5252(3) eV, including, among others the effect of the finite nuclear mean square radius [JS85]. The experimental result presented in equation (5.12) differs from the atomic structure calculation by the radiative contributions:

$$\begin{aligned} E^{\text{rad.shift}} &= E^{\text{expt}} - E^{\text{RMBPT}} && (5.13)\\ &= 44.30942(18) - 44.52520(30) = -0.21478(35). && (5.14) \end{aligned}$$

Again, [KBID91] calculated a value of $-0.2163$ eV, which differs by 1.5 meV from the results of this work. The experimental radiative screening correction can be obtained from this by subtracting the hydrogenic, 2s one-electron radiative shift [JS85] at $Z = 21$,

$$E^{\text{rad.scr.}} = (-0.21564(40) \text{ eV}) - (-0.24830 \text{ eV}) = 0.03266(40) \text{ eV}. \tag{5.15}$$

It is customary [IM01, YAS+05] to express this in terms of $F(Z\alpha)$:

$$F(Z\alpha) = E^{\text{rad.scr.}} / \left[\alpha^2 (Z\alpha)^3 mc^2\right] = \underline{0.337(4)}. \tag{5.16}$$

## 5.2 High-energy DR resonances in hydrogenlike $Mg^{11+}$

The hydrogenic magnesium ion was studied in order to establish a reliable procedure for DR rate measurements at high collision energies. In previous attempts on different atomic ions higher-energetic resonances were hard to observe with the electron target and gave questionable rate coefficients due to loss of the beam overlap and vacuum problems. The implementation of a feed-forward correction system to compensate the toroidal drift allows to perform measurements with a large dynamic range of the collision energy (see section 4.4). $^{24}Mg^{11+}$ represents an ideal candidate for such studies, as it can be produced with a large yield at the Max-Planck-Institut für Kernphysik accelerator facility and the ion beam lifetime in the TSR is reasonable.

Experimental data on recombination of highly charged magnesium ions are of interest for modeling of plasmas near intense radiation sources or hot environments, as planetary nebulae [KVS01] and supernova remnants [FCD+04]. In the hydrogenic charge state $Mg^{11+}$ is formed in plasmas at high temperatures.

[SD06] proposes radio observations of ground state hyperfine transitions in highly charged ions of low $Z$ for studies of hot gaseous environments, like the warm-hot intergalactic medium, starburst galaxies, or supernova remnants. Promising ionic candidates for such observations are e.g. $^{14}N^{6+}$ or $^{25}Mg^{11+}$ and interpretation of the data relies on abundance model calculations.

### 5.2.1 Experiment

As a guidance for the experiment in search for high-energetic resonances and the expected strengths the help of theoretical predictions [Fri05] was asked for. Since the target ion in its initial hydrogenic state is a rather simple system the quality of the theoretical calculations is expected to be sufficient.

The lowest excited state of a hydrogenic system without hyperfine interaction is a $2l_j$-state and thus one finds DR resonances in ground-state $Mg^{11+}$

$$^{24}Mg^{11+}(1s) + e^- \rightarrow ^{24}\,Mg^{10+}(nl_j\; n'l'_{j'}) \tag{5.17}$$

only with $n, n' \geq 2$. The bound electron is excited from the K-shell ground state into the L-shell and the incident electron occupies a state in the L shell (KLL) or any higher states (KL$x$). Thus, the only observable DR recombination channels are $\Delta n \geq 1$-reactions. The lowest possible core excitation is the inverse of the Ly$\alpha$ core transitions with a Rydberg electron in the outer shell. Precise experimental values for the transitions $1s - 2p_{1/2}$ and $1s - 2p_{3/2}$, 1472.67(4) and 1471.62(7) eV respectively, are known from earlier experiments [HFK+98] at an EBIT. A coarse estimate of the

DR resonance series can be made with the Rydberg formula,

$$E_{\mathrm{DR}}(n) = E_{\mathrm{Ly}\alpha} - Ry\frac{q^2}{n'^2} \quad \text{for } n' \geq 2. \tag{5.18}$$

One finds the lowest DR resonance (KLL, $n' = 2$) at an energy interval of approximately 1050 eV. Similarly the energy positions of higher Rydberg resonances can be estimated.

The experiment has been carried out on an $Mg^{11+}$ ion beam produced at the Tandem accelerator and injected into the TSR at a final kinetic energy of 81.4 MeV. The ions were continuously cooled by an electron beam in the electron cooler device, while the electron target provided an electron beam as a collisional probe at high relative energies. Electrons of matched velocity have a lab energy of $\approx$ 1840 eV and one can estimate the lab collision energy (2.7) of the first DR resonances to $\approx$ 5670 eV. Similarly the $\Delta n = 1$ series limit is expected at a lab energy of $\approx$ 6610 eV. With equation (4.7) one estimates a displacement of the electron beam in the interaction section of $\approx$ 5 mm due to the toroid drift in the toroid. The amount of this drift is of the order of the electron beam radius and leads to a loss of overlap if unaccounted for. Initially, during the setup and optimization phase the beam overlap has been established using the electron target in cooling mode at zero relative energy and tuning for efficient phase space cooling of the ion beam. Once this has been achieved, the control over the ion beam position was handed over to the calibrated automatic drift compensation system (section 4.4) to retain the beam overlap throughout the following measurements. The electron target has been set up with the high-yield thermionic cathode gun and provided an electron beam of a density of $n_e \approx 2 \cdot 10^7/\mathrm{cm}^3$ at an expansion factor of $\xi = 13.9$ and $B_{\mathrm{guide}}^{\mathrm{interact.}} = 0.0576$ T. In fact this expansion ratio is the result of a — later discovered — calibration error of the magnetic field in the interaction zone of the electron target, as already described for the $Sc^{18+}$ measurement on page 58. It had been foreseen to use an expansion factor of $\xi = 20$, which indeed was set in all other sections of the electron target, apart from the interaction section.

After one second of cooling of the ion beam at static electron beam conditions the energy scan of the electron target was started by the data acquisition system (section 3.3). The measurement scheme included a wobble scheme with interleaved reference steps at a static energy without DR resonance structure for determination of the background level. To suppress dynamic changes in the rest-gas vacuum the reference point was always chosen close to or within the present energy scan range. The electron-ion recombination products were recorded using the MIDAS detector (section 3.2), adjusted for $\kappa = 10/11$.

As the drift compensation system has been used in this experiment for the first time in a high-energy experiment, its operation was thoroughly tested. This test was performed by introducing an artificial displacement of the electron beam by the "Acceleration-Y" steerer by manually seeding the desired steerer current. For gradual shifts the resonance strength of the KLL resonances at $\approx$ 1040 eV was observed. The results of this test are shown in Fig. 5.10. One finds a plateau of the width of approximately the electron beam diameter and fall-off of the gathered rate coefficients on both ends. The symmetry of the plateau shows that the electron beam is well centered

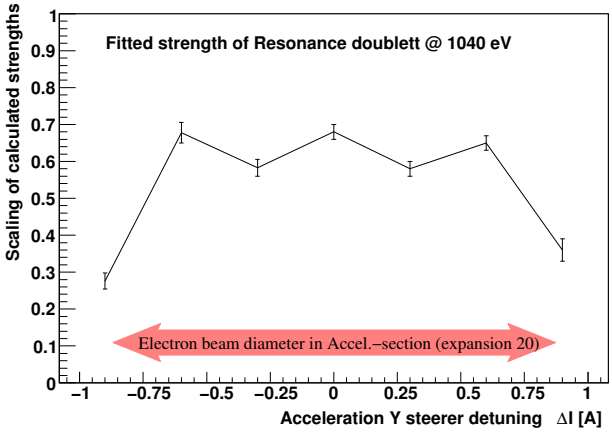


**Fig. 5.10:** *Verification of the beam overlap. The resonance doublet at ≈ 1040 eV has been measured for gradual vertical displacements of the electron beam. The theory resonance strengths fitted with a scaling factor and fixed relative ratio. The scaling factor is shown for different vertical displacements. The symmetry of the fall-off towards both ends means the electron beam is well centered in its original position.*

on top of the the ion beam position in its initial position ($\Delta I = 0$) and confirms the successful operation of the drift compensation system.

### 5.2.2 Data analysis

The precise cooling energy of the electron beam has been determined by the *mirroring method* described previously in section 5.1.2 to $E_{\mathrm{cool}} = 1847.63(2)$ eV using the symmetry of the RR peak. Most of the analysis has been carried out similarly to the $Sc^{18+}$ analysis.

The result of the experiment is displayed in Fig.5.11. This shows the experimental rate coefficient as a function of the relative collision energy. The blue arrows indicate the Rydberg resonance positions estimated with equation (5.18).

Taking a closer look into the structure of the KLL, KLM and KLN resonance groups one finds a remarkably good agreement of the experiment to the theoretical calculations by [Fri05]. A comparison to the calculations is shown in Fig. 5.12. The contributions of the transverse temperature are too small to be derived from calculations and the fitting of the convolutions of the theoretical spectrum have been performed with a calculated value of $k_B T_\perp = 7.863$ meV. The longitudinal temperature was a free fit parameter and a value of $k_B T_\parallel = 51(3)$ $\mu$eV has been derived from the fitting results. For the only isolated single resonance at around 1060 eV one finds a full width at half of the maximum $FWHM \approx 0.78(8)$ eV, i.e. $FWHM/E_{\mathrm{rel}} = 7 \times 10^{-4}$.

The calculated resonance strengths were scaled, and the resonance positions shifted as a whole for each of the three groups with fixed relative positions and relative strengths in each group. Generally the relative peak amplitude ratios of the theoretical calculations are well reproduced, while the experimentally obtained rate coefficients are lower than predicted by ≈ 35 %. However, one finds the calculated resonances to be *stretched* apart slightly, relative to the observed structure.

**Energy uncertainty** The experimental limits on the energy axis due to systematical uncertainties have been estimated in analogy to the $Sc^{18+}$ data analysis (section 5.1.3), one finds systematical uncertainties for this measurement in the range of 0.5 to 0.75 eV

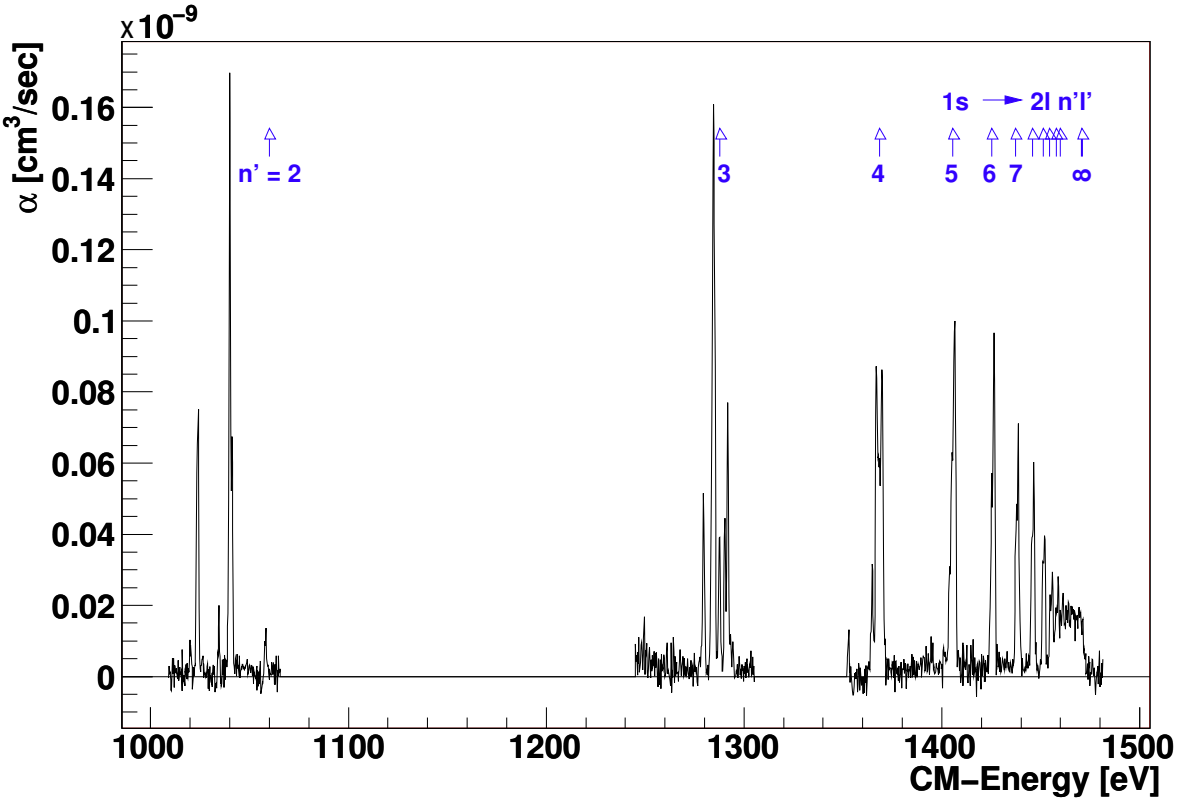


**Fig. 5.11:** *Experimental* $Mg^{11+}$ $\Delta n = 1$ *DR resonances as a function of the center-of-mass collision energy. The blue arrows indicate the Rydberg series* $\mathrm{Mg}^{11+}(1s) + e^- \rightarrow \mathrm{Mg}^{10+}(2p_{3/2}\ n'l'_{j'})$.

over the scanned energy interval (see Fig. 5.13).

**Absolute rate uncertainy** The measurement of the ion beam current is traditionally the largest source of uncertainties for absolute rate measurements, an uncertainty of 15% is assumed [LWH$^+$96]. The calculation of the rate coefficient assumes a homogeneous beam profile. A hollow electron beam profile with thinned out center leads to an overestimation of the electron density and consequentially undersized rate coefficients. An upper limit of 6% for this uncertainty is estimated from known electron beam profiles at similar conditions. The influence of other uncertainties plays a minor role. These influences are the detection efficiency and pile-up in the detector electronics. The product ion beam from a cooled parent ion beam had a diameter of $\approx 1 \times 1$ mm. With an sensitive detector area of $20 \times 20$ mm the geometrical uncertainty is negligible. The pile-up probability can be estimated by $p_{pu} = R_{det} \times \Delta t_{gate}$. With a maximum detector rate of $R_{det} = 100$ kHz and a detector gate length of 100 ns, the contributions are below 1% and can be neglected.

A total uncertainty of the rate determination of 20% is assumed from this contributions.

In a summary it was possible for the first time to successfully measure DR reso-

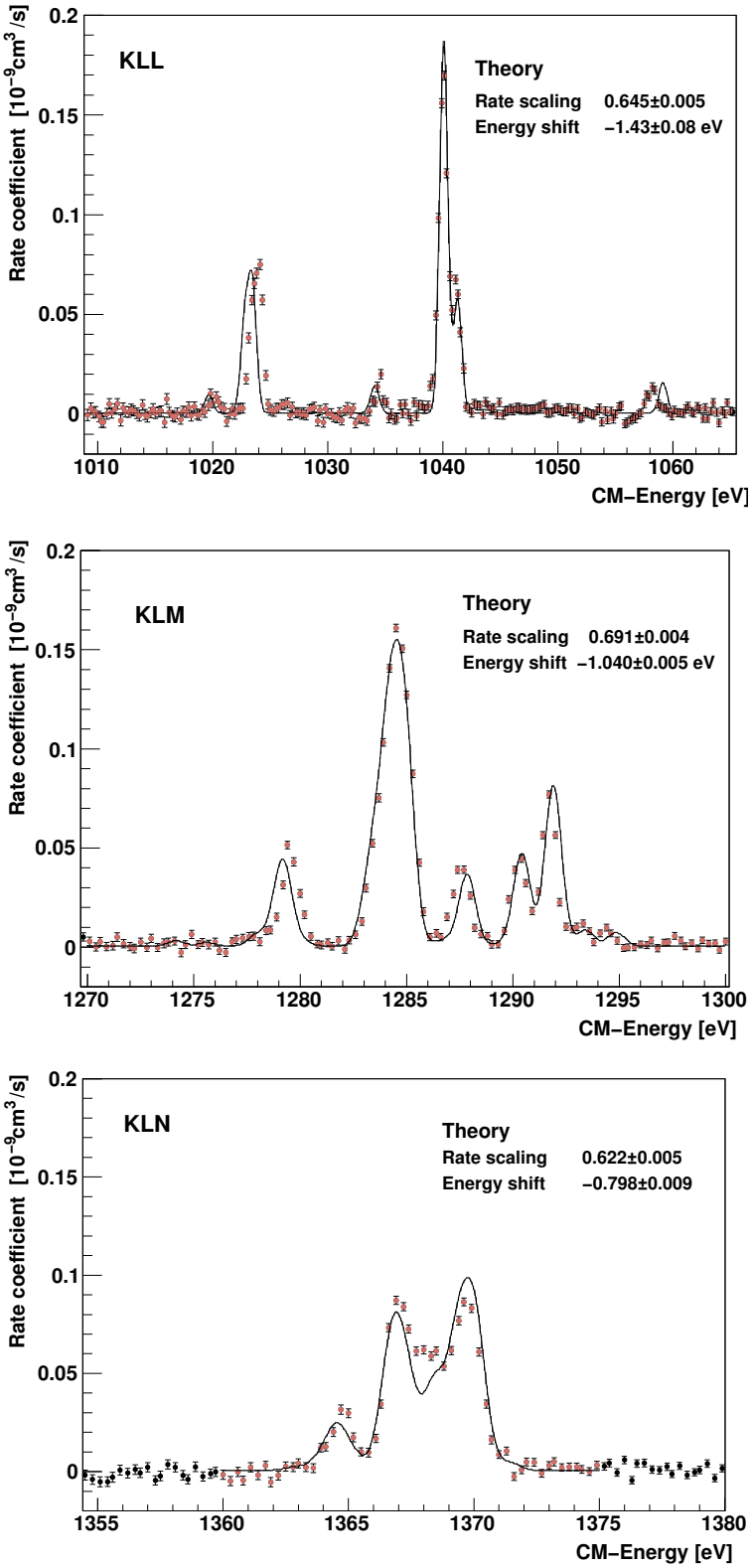


**Fig. 5.12:** *$Mg^{11+}$: comparison to theory for the KLL, KLM and KLN resonance groups. The calculated resonances were convoluted with the electron temperatures and for each group resonance strengths the whole group was scaled and shifted as a total.*

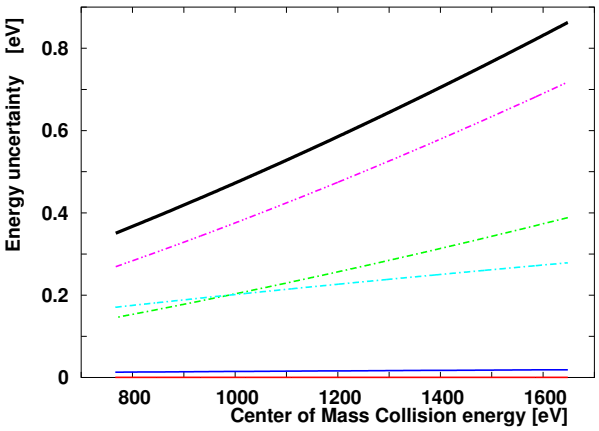


**Fig. 5.13:** *$Mg^{11+}$ systematical error of the energy determination. Solid black curve: squared sum of all contributions. Red curve: merging angle ($\Delta\theta = 0.2$ mrad). Blue curve: determination of the cooling energy by mirroring method (0.02 meV). Cyan curve: Absolute error of the space charge correction (0.2 eV). Magenta curve: relative voltage precision ($10^{-4}$). Green curve: Absolute error of cooling voltage measurement (0.2 eV).*

nances at highest relative energies. This was possible only due to the development of the toroid drift compensation system, which retained the beam overlap throughout the whole energy range of the scans. From the measured spectrum a FWHM resolution of $\Delta E/E = 7.5 \cdot 10^{-4}$ could be derived. Uncertainties on the energy axis are of similar order of magnitude.

The observed spectrum generally agrees quite well with the theoretical predictions. The relative strength ratios mostly agree very well between experiment and theory. The energetic structure of the theoretical model had to be shifted slightly towards lower energies. The spread of the associated fine structure to each Rydberg state slightly overemphasized by the calculations. As the theoretical calculations were obtained without the guidance of experimental results the overall agreement is acceptable. The scaling of the calculated strengths is not explained by the experimental uncertainties. Similarly, in another beamtime on $Si^{3+}$ [Schb] which was performed just one month before the beamtime presented here shows a comparable discrepancy of missing $\approx 35\%$ rate in comparison to results from CRYRING [OGA+06] and theoretical calculations. However, there a later repetition [Schb] of the $Si^{3+}$ experiments resolved in good agreement with theory and the CRYRING results. The origin of this discrepancy, could not yet be safely resolved and is still under study. The experimentally to low rate wasn't discovered during the beamtime, as the interim data analysis was made using the wrong effective expansion ratio[2] in the interaction section and both effects compensated each other. For the future it can be expected that, with the now correct magnetic guiding field calibration, a loss of 35% in the rate coefficients would be discovered soon enough for a timely investigation.

## 5.3 Radiative recombination in lithiumlike $F^{6+}$

As has been discussed in section 2.2.1 the experimental results on radiative recombination (RR) from all cooler-storage rings show an enhancement of the observed low-energy RR rate over equation (2.2) (see also Fig. 2.1). These show an excess recombination

[2] See page 58

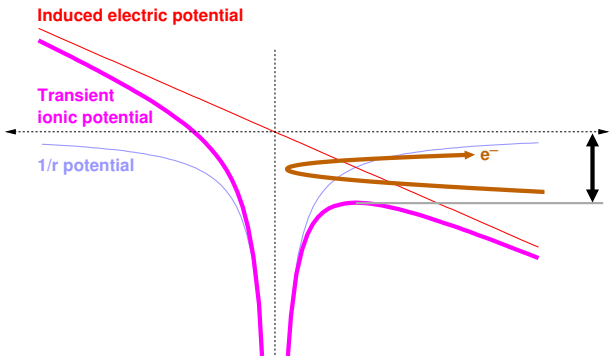


**Fig. 5.14:** *The motionally induced electrical field modifies the ionic potential and a Stark saddle is formed. This lowers the effective ionic potential. Electrons penetrate into the modified ion potential. Upon transition to the constant field region in the interaction section the Stark saddle is attenuated and a $1/r$-potential is reestablished. Electrons within the ionic potential populate highly excited Rydberg states with large angular quantum number [HYW+05].*

rate at small relative energies, typical magnitudes are an enhancement by a factor of approximately two. The enhancement becomes visible at relative energies corresponding approximately $E_{\mathrm{rel}} = k_B T_{\perp}$ and forms a plateau for relative energies $E_{\mathrm{rel}} < k_B T_{\parallel}$ (See Fig. 2.1).

In a recently published work [HYW+05] a promising approach has been taken to explain this behavior. The sketched out model considers the induced electrical field seen by the ions, while they propagate through the merging toroid magnet of electron cooler devices. Along this path the ions are exposed to a time-dependent transverse magnetic field component of the guiding field and see it as a electrical field. The transient electrical field interacts with the ionic potential and forms a Stark saddle (see Fig. 5.14). The electrons are merged with the ion beam while the Stark saddle is developed. As the merged beams pass on to the cooler's interaction region with constant magnetic fields the electric field levels out and the $1/r$-potential is restored and the Stark saddle is removed. In this situation a part of the electrons finds themselves bound to the ionic potential in typically highly excited Rydberg states with large angular quantum numbers [HYW+05]. This coupled system is destroyed by the demerging toroid on the exit end of the electron cooler device. However, during the passage of the ion through the constant field region a fraction of the ions can deexcite further into lower states of the ionic potential which are stable against field ionization and manifests as additional recombination signal.

An experimental approach for studies of this interpretation is available by modifying the merging process of the electrons with the ion beam. The setup of the electron target (section 4.1) allows such a modification, as it features a set of successive drift tubes in it's interaction section. Surrounding the electron beam the electron energy can be tuned by manipulating the drift tube potential. The electrons kinetic energy within the drift-tubes is $E_{\mathrm{rel}} = eU_{\mathrm{cath}} + eU_{\mathrm{drift}}$. While the kinetic energy of the electron beam in the merging section of the toroid $E_{\mathrm{rel}}^{\mathrm{tor}} = eU_{\mathrm{cath}}$. This allows to perform the merging of the electron beams at relative energy and to bring the electrons to their final collision energy when they are already merged with the ion beam. The spatial merging at low relative energy, where the model [HYW+05] predicts the rate enhancement to stem

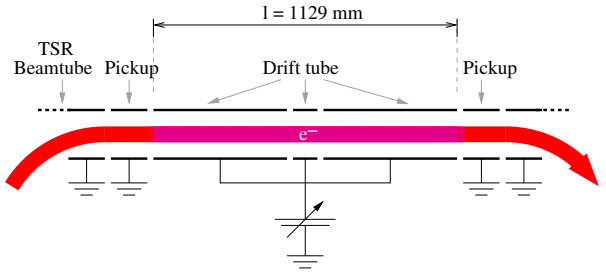


**Fig. 5.15:** *Configuration of the drift tubes in the interaction section of the electron target. By tuning the potential on the drift tubes the electron energy in the interaction section can be manipulated.*

from, is avoided in this phase. Later, the small additional potential (typ. 100 V) does not influence the ion beam energy significantly due to the ions orders of magnitude higher kinetic energy ($\approx$ 74 MeV).

To carry out such experiments a bare parent ion without electronic shell might seem a tempting candidate for systematic studies of RR, such as $C^{6+}$. The recombination of bare ions with electrons is not spoiled by low-energy DR features and given purely by radiative recombination. However we have chosen lithiumlike $F^{6+}$ for the following reasons. Electron-ion recombination in Lithiumlike $F^{6+}$ has been studied intensely in experiment and theory [TEG$^+$02, GH$^+$00] in the past and RMBPT calculations of low-energy $\Delta n = 0$ DR resonances fit remarkably well with experimental results obtained at the TSR [TEG$^+$02]. The low-energetic DR resonances allow the determination of the electron temperatures and to judge the overlap of the electron and ion beams. The ion beam was injected into the TSR at 74.5 MeV energy and cooled by the electron cooler. The kinetic energy of the velocity-matched electron beam was reconstructed to 2136.25(2) eV employing the mirroring method, as described in section 5.1.2. A recombination probe beam of 1 mA has been provided by the electron target at an expansion factor of $\xi = 30$. The laboratory energy of the electron beam has been varied in the range of 2200 to 2070 eV, corresponding to a center-of-mass energy range of +0.8 eV to −0.8 eV. The measurements have been performed in a wobble scheme alternating between a constant reference electron energy and a scanning measurement energy with 20 ms length of each step and 5 ms waiting time in between to adjust for the slew-rate (see section 4.5.1).

In a first measurement the spectrum was taken employing the classical method of scanning the electron energy by variation of the cathode potential and merging to the ion beam at the final electron energy. The experimental data was deconvoluted for toroid effects, similar to section 5.1.2. This results are shown in the upper pane of Fig. 5.16.

In a different attempt, the electron beam formation was kept at static energy, slightly detuned from cooling energy by +15.26 eV. For parallel beams this translates to a relative energy of 27.2 meV. The electron beam was merged with the ion beam and the final collision energy was tuned by variation of the potential on the drift tubes in this section. The results are displayed in the lower pane of Fig. 5.16. Further measurements have been performed at different detuning voltages of −25, +25, +75, and +150 V. Those results were essentially comparable to the results at +15.26 V and therefore are not shown here. As well, the geometry of the accelerating field has

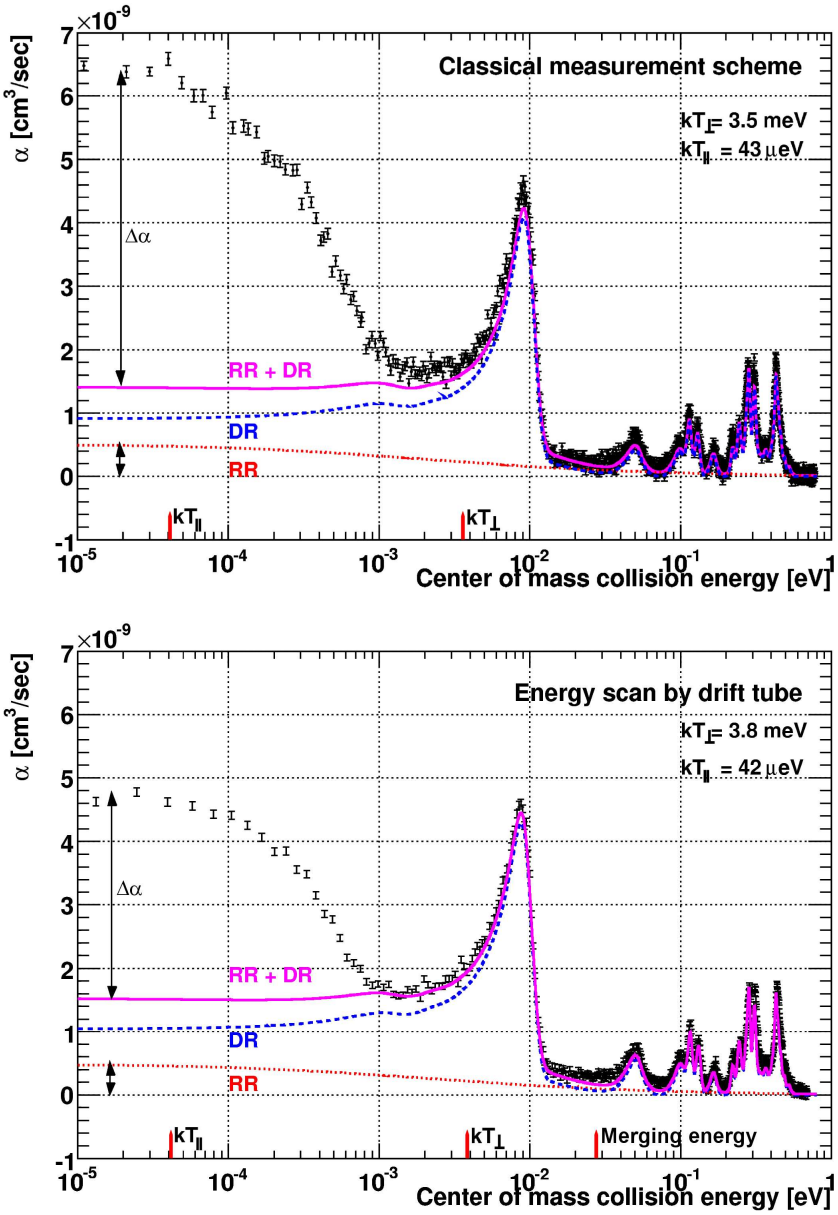


**Fig. 5.16:** *Low-energy recombination of* $F^{6+} + e^-$. *The upper pane shows the results of a measurement employing the classical scanning method by variation of the cathode potential and grounded drift tubes in the interaction section.*
*In the lower pane the electrons have been merged with the ion beam at a static energy and tuned to collision energy by variation of the drift tube potential.*
*The overlayed curves are the individual contributions from radiative recombination (dotted red curve), dielectronic recombination (dashed blue curve) and their sum (solid magenta curve).*

been varied by excluding different elements of the available drift tubes, which gave essentially the same results as the geometry indicated in Fig. 5.15, scanning all three drift tubes.

Both experimental spectra were fitted with the theoretical resonance structure

| Resonance | # | Energy [eV] | Strength $10^{-20}$ eV cm$^2$ |
|---|---|---|---|
| $(2p_{3/2}\ 6p_{1/2})_2$ | 2 | 0.01031(2) | 388.9(2.5) |
| $(2p_{1/2}\ 6d_{3/2})_2$ | 3 | 0.0524(3) | 67.6(2.3) |
| $(2p_{1/2}\ 6d_{5/2})_3$ | 4 | 0.1005(4) | 54.9(2.1) |
| $(2p_{3/2}\ 6p_{3/2})_2$ | 5 | 0.1168(1) | 57.5(1.7) |
| $(2p_{1/2}\ 6d_{5/2})_2$ | 6 | 0.1324(2) | 52.3(1.5) |

**Table 5.5:** *Fitted $F^{6+} + e^- \rightarrow F^{5+}$ DR resonances ($\Delta n = 0$). All errors are statistical errors only. $k_B T_\perp = 3.5(1)$ meV and $k_B T_\parallel = 42(2)$ $\mu$eV. All other resonances and all natural widths have not been varied and are according to [TEG$^+$02].*

[TEG$^+$02] in the energy range of 4 meV to 200 meV. Free parameters of the fits were the electron beam temperatures $k_B T_\parallel$ and $k_B T_\perp$ and the peak strengths and positions of the second to sixth resonance. The first resonance has a very broad structure and was not varied during the fit. The remaining structure is a blend of 46 overlapping theoretical resonances with partly broad natural widths [TEG$^+$02]. All resonance widths weren't varied during the fit, either. The results of the fitting for the *classical* method are summarized in Table 5.5. From the fitted results the individual contribution from the DR- and RR channels have been isolated and are displayed as blue dashed and red dotted lines respectively in Fig. 5.16. The sum of the RR and DR channels is given by the solid magenta line and one can identify the excess rate $\Delta\alpha$ for low energies. One finds a strong difference between both types of measurement at small relative energies $\leq k_B T_\perp$. The *classical* scanning method shows a remarkably high enhancement by $\Delta\alpha = 5.1 \times 10^{-9}$ cm$^3$/s, while for the drift tube method a $\Delta\alpha = 3.1 \times 10^{-9}$ cm$^3$/s is found. Also, the shape of the enhancement changes. In the case of the classical method the enhancement is becoming visible for energies approximately below to the thermal energy of the electrons transverse degree of freedom. On the other hand the calculated curve agrees reasonably to the experimental data for relative energies down to $\approx 1$ meV until a visible discrepancy appears. In both cases the enhancement reaches a constant level for energies below the thermal energy of the longitudinal degree of freedom.

Both measurements gave electron temperatures comparable to a previous measurement [Spr03]. The experimentally derived transverse temperatures agree with the estimate using equation (2.25), $k_B T_\perp = 3.59$ meV for a cathode temperature of 1250 meV and expansion $\xi = 30$.

The initial objective of these measurements has been to experimentally analyze the theoretical model [HYW$^+$05], which attributes the rate enhancement to the merging process of the electron beam with the ion beam. The model explains the observed excess rate by capture electrons in a motionally induced electrical field in the toroid sections of the electron beam device. This experiment has taken measures to merge the electron beam at a detuned energy and to adjust the final collision energy in the straight interaction section of the electron target. The ions see the detuned electron beam with a large relative energy and the transient highly excited Rydberg states are not formed

in this phase of the interaction. The experimental results show a significant reduction of the rate enhancement in the *drift tube* method over the *classical* method and is qualitatively within the expected behavior from [HYW+05]. Yet, the enhancement is not be completely eliminated by the drift tube method, as the acceleration of the electron beam to it's final collision energy by applying a tunable potential on the drift tubes introduces additional electrical fields, although their field strengths are small (typ. 5 V/cm), compared to the large motionally induced field strenghts in the toroid region (typ. 1000 V/cm).

# Chapter 6

# Conclusion

## 6.1 Summary

Electron beams in heavy ion storage rings are used mainly for two purposes, for electron cooling and as collisional probes. A magnetized electron beam is described as a plasma with anisotropic flattened double Maxwellian velocity distributions for the longitudinal and transverse degrees of freedom. One usually describes both distributions by associated longitudinal and transverse temperatures. In typical conditions the longitudinal temperature is a few orders of magnitude smaller than the transverse temperature. Both, electron cooling and collisional probe operation, benefit from low transverse and longitudinal spreads. The former by a enhanced cooling force, leading to improved efficiency of the cooling process. The later by enhanced resolution of energy-resolved measurements.

The central theme of this work has been to produce ultimately cold electron beams and apply them as a probe in merged beam electron-ion collision experiments. Following the objectives of this work, formulated in section 2.6, the following issues have been addressed:

**Detector setup and data acquisition** The detector setup has been implemented and taken into operation. It allows detection of ions on both, the ionization and the recombination sides of the ion beam. It has been integrated into a complete experiment control and data acquisition system. The *mileDAQ* system has been successfully used in various experiments on molecular and atomic ion beams.

**Electron temperature studies** The production of the electron beam is a multistep process and the electron optics influence the final achieved temperature. The kinematic transformation of the accelerated electron beam efficiently reduces the longitudinal spread in the electrons rest frame. However additional processes in realistic electron plasmas contribute as heating mechanisms, so that the observed temperatures are always higher. The heating mechanisms are the result of relaxation processes between the longitudinal and transverse degrees of freedom.

The transverse-longitudinal-relaxation (TLR) is the result of the strong anisotropy between the longitudinal and the transverse temperatures when energy is transferred from the transverse onto the longitudinal degree of freedom. The TLR contributions depend strongly on the ratio of the inter-electron distance $d = n_e^{-1/3}$ and the cyclotron radius $r_{\mathrm{cycl}}$ of an electron in the magnetic guiding field. The experimental results obtained in this work agree well with this simple picture, although the quantitative comparison in our models of present TLR theories has potential for further improvement.

The longitudinal-longitudinal relaxation (LLR) is the result of the acceleration of an electron beam. The timescale for thermal rearrangement processes in a electron plasma is defined by the plasma frequency. Fast distortions of the electron plasma on this timescale distort the equilibrium of the arrangement of the electrons. The strong coupling of the electrons by Coulomb interaction leads to release of potential energy while the electrons reestablish equilibrium situation. The released energy leads to a heating of the longitudinal degree of freedom. The suppression of this LLR contributions is only possible by performing a smooth acceleration of the electron beam, where the electrons always adjust to the slowly increasing energy and inter-electron density. This scheme was applied here in a practical two-step acceleration scheme combined with transverse magnetic expansion. This work shows a series of measurements for a range of different acceleration field gradients and clearly demonstrates the impact of the acceleration structure on the longitudinal temperature.

These measurements were performed at electron energies up to 4000 V and small densities, as technical limits restricted the operation range of the retarding field analyzer. As Fig. 4.9 shows, the contributions from LLR are becoming more pronounced for higher electron currents. Ultimately low longitudinal electron temperatures of $k_B T_{\parallel} = 11$ $\mu$eV were obtained for an electron current of 50 $\mu$A. As the slope of the accelerating gradient increases towards higher energies and identical gradient lengths, LLR effects will play a more important role. On the other hand TLR contributions become apparent for overdimensioned length of the electron path (Fig. 4.4). It decreases for faster electrons, since the drift times are shortened (see Fig. 4.6). A strong magnetic guiding field helps to control the TLR effectively (Fig. 4.5).

**Electron beam properties at high energies** The operational range of the electron target was advanced to higher energies. This has been possible by the studies of the energy-dependent toroid drift behavior, which destroys the overlap of the electron beam with the ion beam. An automatic system for compensation of this toroidal drift has been developed and implemented and calibrated here. Time-resolved studies of the electron energy upon energy jumps allow to compensate artifacts due to the slew-rate of the setup and improve the resolution.

**Merged beam electron ion collisions** With the improved electron beam temperatures a series of electron collision experiments on simple hydrogenic and lithiumlike ions has been performed to study recombination reactions. The electron target gave an

unprecedented high resolution in recombination measurements The increase in resolution is attributed partly to the improvement of the ion beam quality and partly to the low energy spreads of the electron beam. The decoupling of the cooling- and probe-operation into two dedicated electron beams is beneficial to the ion beam quality, as a constant strong cooling eliminates transient energy dragging and suppresses intrinsic heating effects. It also allows to tune both electron beams at different parameters for expansion and density and thus to achieve optimized conditions for the required mode of operation. The superior electron beam quality from the electron target gives highest sensitivity for energy resolved electron-ion collision reactions. Three different ionic species have been studied in this work.

1. Low-energy $\Delta n = 0$ DR resonances in lithiumlike $Sc^{18+}$ have been measured at relative energies up to 300 meV. The electron target was operated with the cryogenic photocathode electron source. Low electron temperatures of $k_B T_\perp \approx 1$ meV and $k_B T_\parallel \approx 25$ $\mu$eV were reached and allowed a significant improvement of the resolution. With this record sensitivity the hyperfine splitting of DR resonances has been resolved for the first time.

   The experimental data has been fitted in the energy range from 2 meV to 95 meV. In combination with earlier results of RMBPT calculations [KSS+04] on the binding energy of the $10l$ Rydberg-electron the $Sc^{18+}$ $2s_{1/2} - 2p_{3/2}$ transition energy can be determined to 44.30942 eV with 5 ppm accuracy.

2. The measurement on hydrogenlike $Mg^{11+}$ has been used as a test-bench for spectroscopy measurements at large detuning energies. Earlier experiments were suffering from the inherent drift of the electron beam in the toroidal merging sections of the electron cooler device. As a result the electron beam enters the interaction sections on energy-dependent positions. Thus, the position of the ion beam within the parabolic space charge potential changes during energy scans. Ultimately the beam overlap is lost, when the toroidal drift is of the order of the electron beam radius. An automatic compensation system has been developed to correct the electron beam position in the interaction zone in a feed-forward system. The correct operation of the compensation system could be clearly demonstrated for $\Delta n = 1$ resonances in $Mg^{11+}$. To reach the required relative energies, spanning from 1000 and 1500 eV, the laboratory energy of the electron beam had to be stepped up by $\approx 4000$ eV. Manually displacing the electron beam off-axis to scan for the beam overlap confirmed that the original position had been well-centered on the ion beam. The discrepancy of the observed absolute rate coefficients from the theoretical data [Fri05] is a little mysterious. The origin of this discrepancy can't be reconstructed from the available data, however it cannot be excluded, that this discrepancy stems from the experiment.

3. Low-energy recombination in the $F^{6+}$ ion was measured to investigate the predictions of a theoretical model [HYW+05] on the radiative recombination puzzle. The model predicts the origin of the rate enhancement to stem from the

low-energy motionally induced electric fields in the toroidal merging section of electron beam devices. This fields modify the ionic potential and allows to populate high Rydberg states and thus contribute by an excess recombination rate. In the experimental studies the electron beam was merged with the ion beam at detuned relative energy and accelerated to the final collision energy by drift tubes within the interaction section. The experimental results show a clear reduction of the excess rate with the drift tube scanning method over the classical method where the ions are merged with fully accelerated electrons. The results show that the merging geometry is of important influence for the recombination rate and confirm qualitatively the argument of the model calculation.

Especially with the cryogenic photocathode electron source ultralow energy spreads of $k_B T_\perp \approx 1$ meV and $k_B T_\parallel \approx 25$ $\mu$eV were observed in recombination experiments. The ion beam quality benefits strongly from the constant cooling. Ion beam energy dragging is eliminated and intrinsic ion beam heating processes are suppressed.

## 6.2 Outlook

The ionic range where the TSR offers good operation conditions for multiply charged ions at masses up to around iron. This range is also the most interesting range for studies motivated by astrophysically relevant atom species and experimental plasma rate coefficients from DR data are becoming available [SSM+06].

The scaling of the electrical field strengths towards higher nuclear charges $Z$ increases the sensitivity for atomic structure measurements. This has motivated plenty experimental and theoretical studies in few-electron heavy ions and is presently a vivid field of research. Among the most interesting effects are isotopic shifts and radiative screening contributions. These fundamental aspects are beyond the reach of the present TSR setup. Presently experiments at the ESR or in EBIT setups [BCTT05] represent the currently most sensitive method.

### 6.2.1 The Heidelberg electron target

The TSR presently features the best-resolving electron collision facility world-wide. This allows many different fields of experiments on atomic or molecular ions, as well as studies of the magnetized electron plasma itself.

Recently it was possible for the first time to measure the life-time of metastable 2s 2p $^3P_0$ states in beryllium-like ion $Ti^{18+}$ for isotopes with ($A = 47$) and without ($A = 48$) nuclear spin [SSB+07]. The principle of this measurement was based on time-resolved observation of DR resonances in both isotopes. This has been possible only due to the high resolution available at the electron target, and the continuous phase-space cooling by the electron cooler fixing the ion beam energy. This method opens an interesting field for future experiments.

Various projects using newly developed detectors at the electron target are under way for molecular ion studies. A three-dimensional imaging system allows reconstruction of the molecular axis from the impacts of neutral fragment [Nov04]. A detector for negatively charged molecular fragments [Hof] gives access to the resonant ion pair formation channels in the molecular break up.

The behavior of electron beams with very low energies is an highly interesting topic for the design of the future electron cooler device for the CSR. The parameter range for that device hasn't been investigated thoroughly, so far. It is highly important to understand the influence of TLR and LLR at low energies and low magnetic guiding fields. The electron target, especially when operated with the cryogenic photocathode electron gun can help to explore this regime and guide the design of the CSR cooler.

The technical side of future developments concentrates presently on the improvement of the performance of the photocathode electron gun. Improvement of the semiconductor design, as well as redesigned vacuum pumping system in the cathode region and additional thermal shields will increase the durability and electron yield of the photocathode samples [Kra].

### 6.2.2 Future electron beam devices

The development of heavy ion storage rings is an active area. Various projects are going on worldwide to implement storage of simple systems. Electron collision spectroscopy is an important experimental method for studies of atomic and molecular systems and appropriate devices are foreseen in each future storage ring. The future storage rings will turn from general purpose devices to specialized operation ranges, as the anticipated experiments demand entirely different conditions.

One such field are studies of interactions in cold molecular matter. The ionic chemistry is a fundamental process which are important e.g. for the formation of stars. Laboratory studies on such systems are difficult as the low-energy molecular ro-vibrational structure is sensitive to the thermal background radiation from the walls of the vacuum vessel. The production of molecular beams, which are not only cold in their relative phase-space, but also internally requires ambitious measures. A consequent path is followed by the plans for the electrostatic cryogenic storage ring CSR [ZWS$^+$05], which will be cooled down to the temperature of liquid helium to suppress the background radiation. This ring will be able to store molecular heavy ions of several thousand atomic masses. The production of a velocity-matched monoenergetic electron beam in such an environment is not a straight-forward task. The electron energy range will have to reach down into the range few eV. The parameters of such slow electron beams are an interesting field for future studies at the Heidelberg electron target.

The proposed extensions of the GSI facility within the FAIR framework cover the other side of the energy regime of highly charged heavy atomic ions with the plans for the future NESR [SPA04] ion storage ring. It will give access to heaviest elements in highest charge state. The GSI has a long tradition in producing exotic atomic species in collision reactions and separation of the fragments. With a high-resolution electron

probe and an efficient cooling mechanism a completely new window for measurements will open and allow precision spectroscopy on short-lived radioactive ion beams. The implementation of a high-resolution electron target is an important component of the NESR design. The acceleration scheme for the NESR electron target is still under discussion and the work presented here can provide some guidance. The experimental results in this work clearly demonstrate that the acceleration structure based on adiabatic acceleration over $\approx 50$ cm can be optimized for minimum longitudinal temperature. A reliable extrapolation into the regime envisaged for the NESR electron target, with electron beams of 40 keV energy and 100 mA current is not easily possible from the limited range accessible with the TSR electron target. However, the results of this work strongly favor designs with an extended multistaged acceleration section. A rough estimate can be made by the following way. The results of this work showed a strong suppression of LLR for a acceleration gradient length of $\approx 50$ cm at an electron energy of 4 keV. Scaling the energy by a factor of 10 to 40 keV increases the electron velocity by $\sqrt{10} \approx 3$. Thus, to keep the acceleration ratio constant gradient length has to be scaled equally and one arrives at $\approx 1.5$ m. It is probably wise to chose a modular design, which allows easy extension of the acceleration structure, if it turns out to be shorter than ideal. This has to be balanced against TLR suppression, which favors short electron paths into the interaction zone.

# Appendix A

# mileDAQ

The changed instrumentation of the TSR with it's new electron target setup and various new detectors required an increased level of flexibility regarding control of the fast parameters and data acquisition and faster computers with a state of the art operating system. The traditional *Cyril*-suite which was used before was running on a outdated Motorola 68030 based LynxOS system and replacement parts for this setup started to fall short. It was also learned from years of experience with this suite that a simpler approach would have been more adequate.

In various other areas of the institute a new, Intel Pentium-III based hardware architecture for VME systems had been established in the meantime. And vendor support for the CPU module is expected to be available for the intermediate future. This new setup was based on a Debian[1] Linux operating system and a versatile driver module [Kih01] for access of the VME backplane.

Based on top of this a new experiment control and data acquisition system, *mileDAQ*, has been implemented. The basic design decisions and introductory documentation will be sketched out here. However it is assumed the reader is familiar with at least a rudimentary level of software development in C, Unix-like operating systems and modern kernel and scheduler concepts. For a complete programmer's reference one should be referred to [Les06].

## A.1 Structure of the controlled parameters

Most experiments performed at the TSR have a common structure. This is to adjust the fast parameters to some predefined values and accumulate data for some period. After this period the data is read out and a new parameter set is tuned for another period of time. This scheme loops over and over until the experimentalist chooses to stop.

Most of the signals to be recorded are voltage signals which are transformed into frequencies by VFC-modules or count rates and can be easily acquired by scalers. In some experiment types a surface-barrier semiconductor detector is used. It's pulseheight is

[1] `http://www.debian.org`

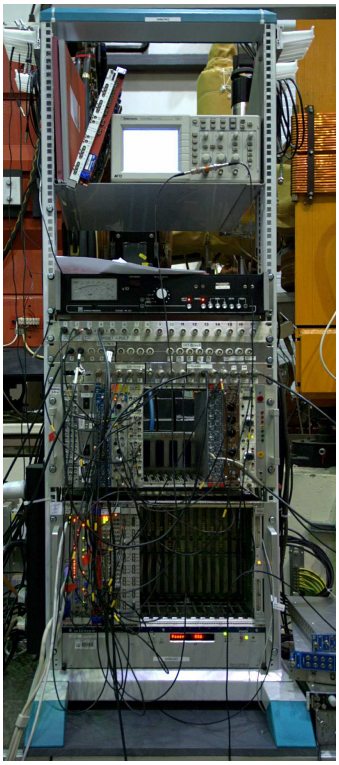

**Fig. A.1:** mileDAQ *Electronics setup. All electronics components of the data acquisition setup are in a compact 19 inch wide rack. A NIM-crate houses all the analog electronics. The data acquisition front-end computer system is in a VME crate of the bottom of the rack.*

recorded by a buffering multichannel peak-sensing ADC.

To achieve a synchronization of all input channels of the scaler and ADC modules the data acquisition setup hands out a *Master-gate*. This is fanned out and used to switch all input channels on or off simultaneously.

## A.2 Anatomy of the mileDAQ software suite

For the implementation of the *mileDAQ* Suite a monolithic approach was chosen, although on selected occasions deviations from this approach have been done for pragmatic reasons.

The architecture is based on a few assumptions on the underlying operating system and hardware setup:

1. The operating system and especially context switches are fast on a timescale relevant for TSR experiments ($\ll$ msec).
2. The data acquisition software has nearly exclusive control of the system.
3. The operating system supports POSIX threads[2].
4. The operating system scheduler supports POSIX[3] soft realtime extensions.
5. String formatting is slow, but can be offloaded to some other system.

[2]See standard *ISO/IEC 9945-1:1996 ("POSIX.1")*
[3]See standard *IEEE Std 1003.1b-1993 ("POSIX.1")*

6. The TCP/IP network subsystem has reliable flow control and the bandwidth to peer systems is fair.

The DAQ system is organized in three layers. The foundation is laid by a control and hardware layer (available as a static library *mileDAQ*, see section A.2.1) which is completely independent of any experiment specific details. On top of this a site description layer is constructed, which contains solutions to common tasks of various experiments at the TSR. The final experiment layer is specific to the specific experiment and implements the measurement and data readout loop.

### A.2.1 Control and Hardware layer

**Timing.**

Timing in a experiment control is an important issue. To avoid a too high complexity of the hardware setup or the underlying operating system a pragmatic approach has been chosen to solve this problem has been chosen, as the possible situations are not critical to regulations of safety or the observable data. Mis-timed events can be identified and sorted out in a later analysis step of the recorded data, where this is justified.

The operating system kernel is a plain official Linux 2.4.20 system and it's scheduler works at a internal beating rate of 100 Hz. The timing of this scheduler works unreliable on timescales below 10 ms. Such a system allows fine-grained timing only by busy loops. However busy loops are wasting CPU resources and block the scheduler from other, possibly more imminent tasks, such as interrupt-handling. The POSIX.1 conforming function `sched_yield()` comes in as a handsome solution, as it allows a running process drop out early and hand back assigned CPU-time to scheduler if other processes are waiting in the run queue. With the assumptions 1 and 2 the probability of coming back in due time is high. This concept is implemented in a `timing.c` by the function `daq_sleep()` as a loop of:

1. The current time is resolved to a nanosecond resolution[4].

2. for delay times $> 3$ s the standard kernel routine `sleep()` is used to suspend execution for one second.

3. for delay times $> 20$ ms the standard kernel routine `nanosleep()` is used for to suspend execution for 5 ms.

4. for delay times $> 2$ ms the function voluntarily offers to drop out early and hand back the assigned CPU time to the scheduler if other processes are pending.

5. If the desired delay time is due, the function returns, else it starts over at step 1.

[4]In fact the time resolution of the used kernel only keeps time to a microsecond, but for future applications the used data structures had been laid out to nanosecond resolution. The last 3 digits therefore are not significant.

As one can see the last 20 ms of this loop are spent in a *nearly busy* loop mode, except for the last 2 ms, where the function does not voluntarily give up CPU time. Since this also means that interrupt handling could be blocked during the last two milliseconds, the hardware modules are laid out with fairly sized buffers for the expected event rates.

**Data passing.**

The storage of experimental data is done to structured text files. These allow to be read and analyzed by human operators and are portable and independent of the underlying machine byte-ordering. However the formatting of the binary experimental data into readable strings is a time-consuming process and should be avoided on the front-end computer. Therefore the process of writing the experiment data to disk has been offloaded to a separate daemon, *daq_listen*, which reads experiment data in a simple binary message protocol (implemented in `message.c`) from a TCP/IP stream (See assumption 6 in section A.2) and writes them formatted to ASCII output file. A detailed description of this format is given in [Les06].

**Hardware support.**

Based upon the Mizzi VME driver[5] for access of the backplane the support for the used hardware components is implemented as userland drivers. As of this writing the following modules are supported.

- a optical fiber communication board, type IPC01 for communication with the two DACs, which are located at the high voltage platforms of the two coolers and are galvanically isolated from the data acquisition setup, `ipc01_kepco.c`,
- a digital I/O-Module with 8 input channels and 8 output channels, `mpiorl.c`,
- an peak-sensing 8-channel ADC board, type CAEN V556S, `caen_v556.c`,
- a 250 MHz 32-channel scaler, type Struck SIS 3820, `sis3820.c`.

### A.2.2 Site description layer

The site description layer implements all necessary functionality for a given experimental site. For experiments at the TSR these are e.g. control of the injection into the storage ring, control of shutters in front of sensitive detectors, control of the electron beam energy, gate control, or detector readout.

### A.2.3 Experiment layer

The topmost layer is the experiment layer. It completely describes the individual experiment and the sequence of steps. It has to be provided by the experimentalist as

[5]Mizzi Computer Software GmbH, `http://www.mizzi-computer.de/`

an own application written on top of the site description layer and the lower control- and hardware layer. However a collection of such programs has emanated during this work, which are dedicated to typical atomic or molecular experiments.

Since the compilers on modern computer systems are reasonably fast, the compilation time is negligible. Therefore the parametrization of the Experiment layer is done through C header files instead of a dedicated parser for a jet-to-be-invented parameter file format. A well documented template for the parameter file format guides even unexperienced programmers through the steps. A companion wrapper script, `start` manages the compilation and startup of the freshly parametrized experiment control program.

A friendly user interface (fig. A.2) gives feedback and control of the current experiment status.

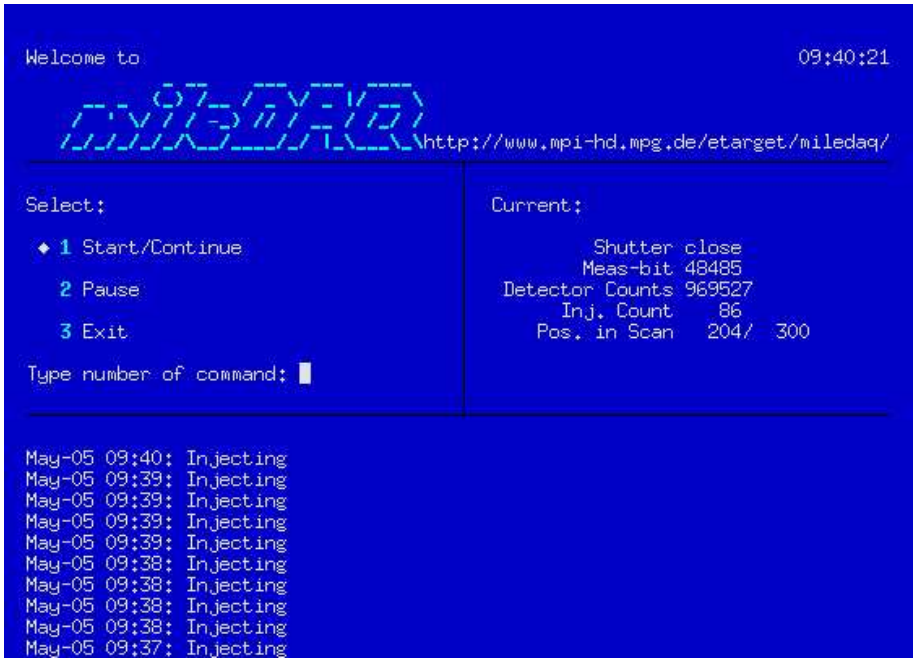


**Fig. A.2:** *A screenshot of the mileDAQ user interface during a running experiment.*

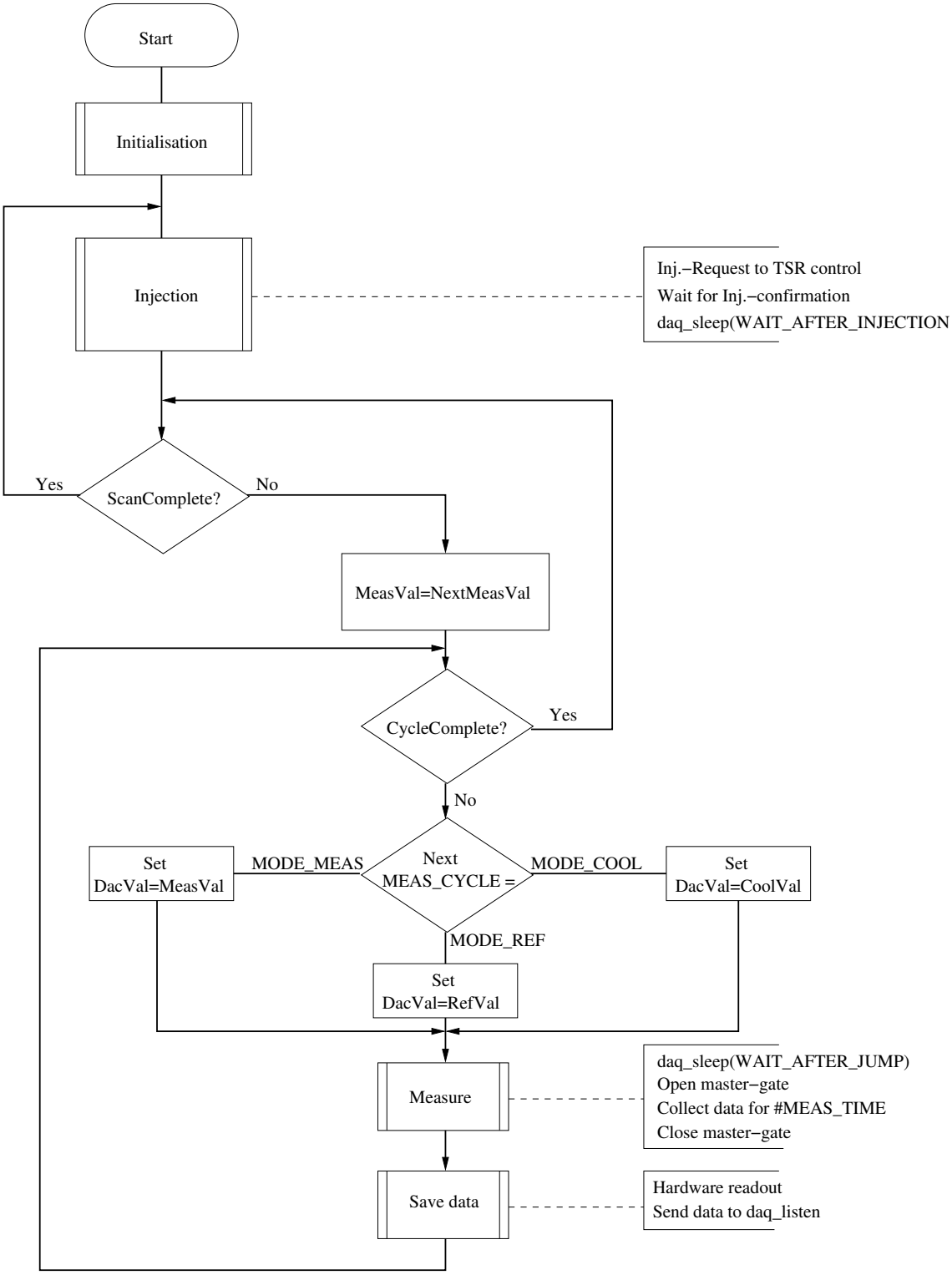


**Fig. A.3:** *Simplified Flow diagram for DR experiments*

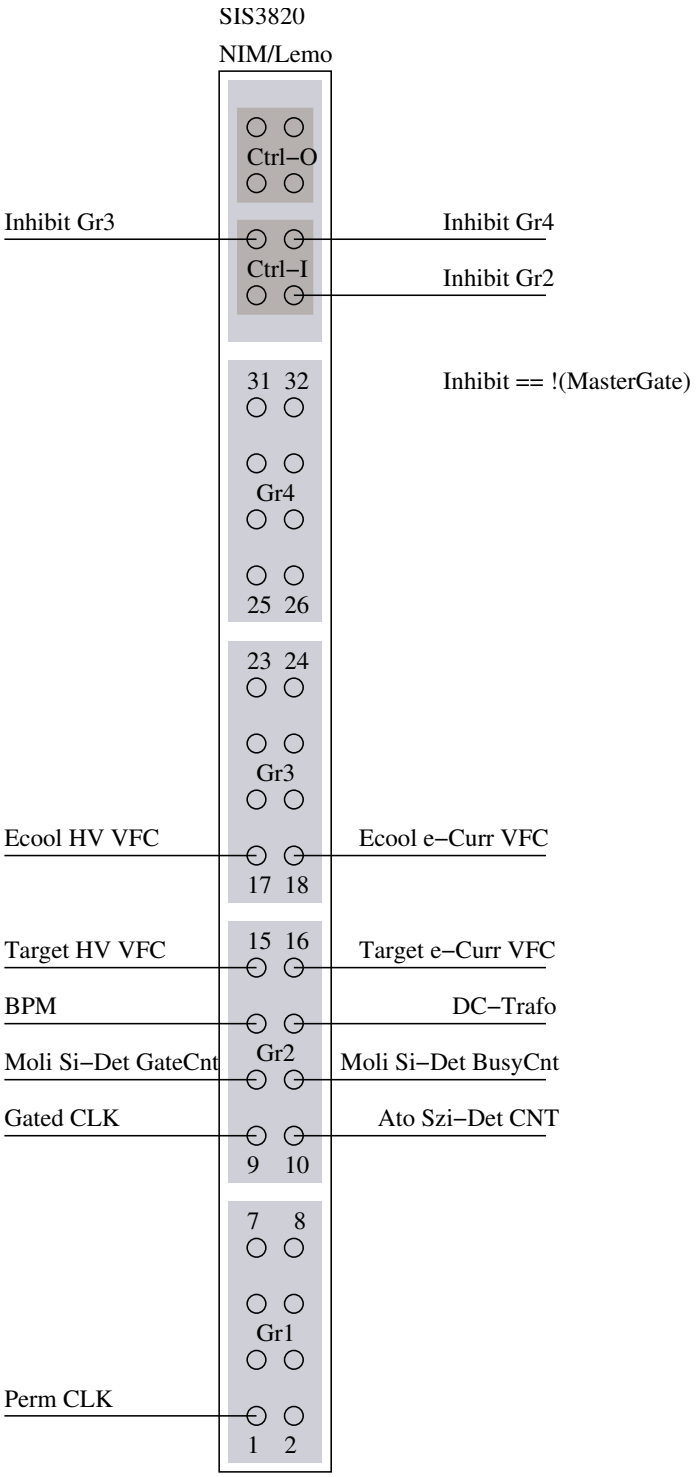


**Fig. A.4:** *SIS 3820 multiscaler. Input channel assignment*

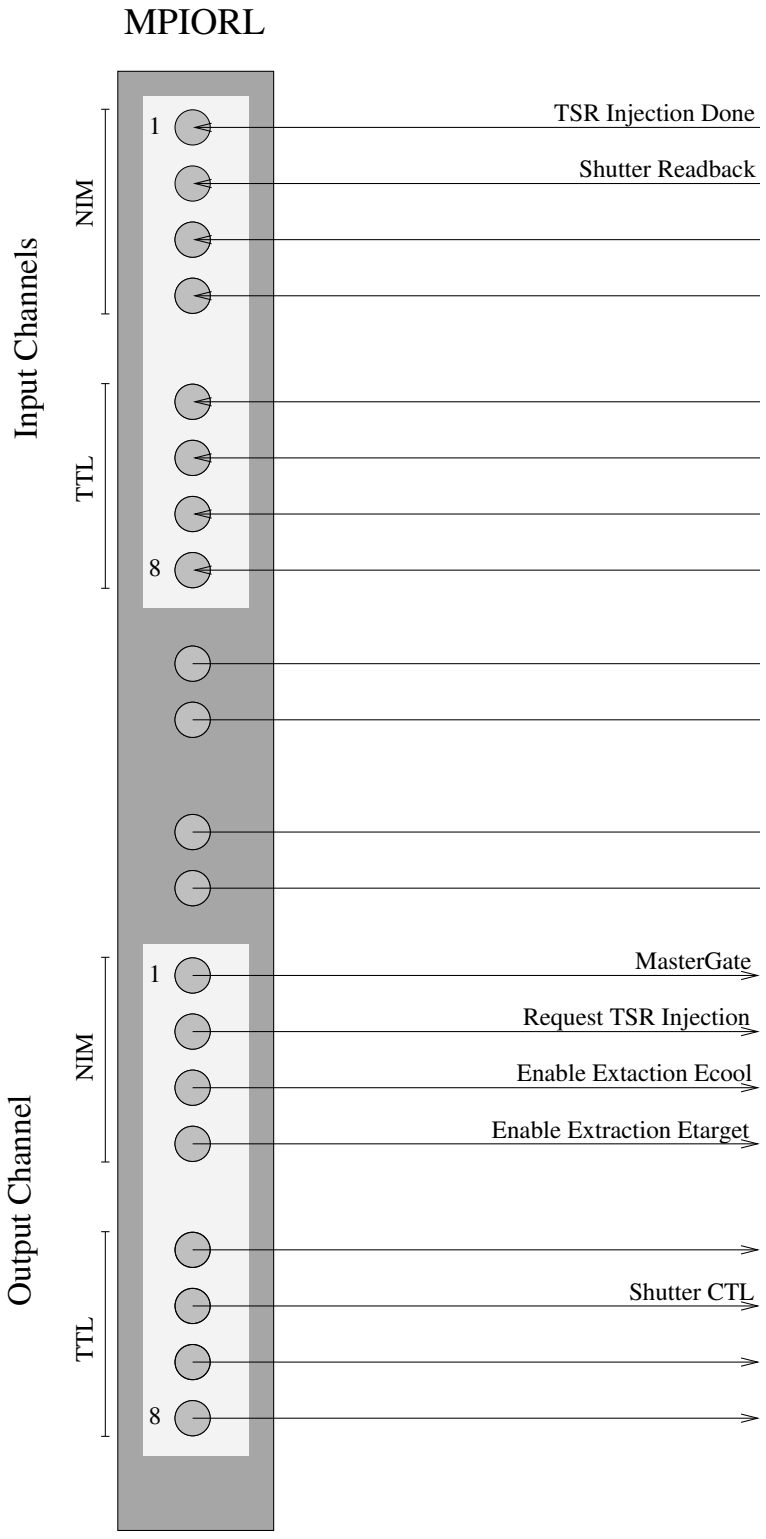


**Fig. A.5:** *MPIORL digital IO board. Channel assignment.*

# Appendix B

# Electronics layouts

The layout of the electronics for the toroidal drift compensation (described in section 4.4) is shown in Fig. B.1.

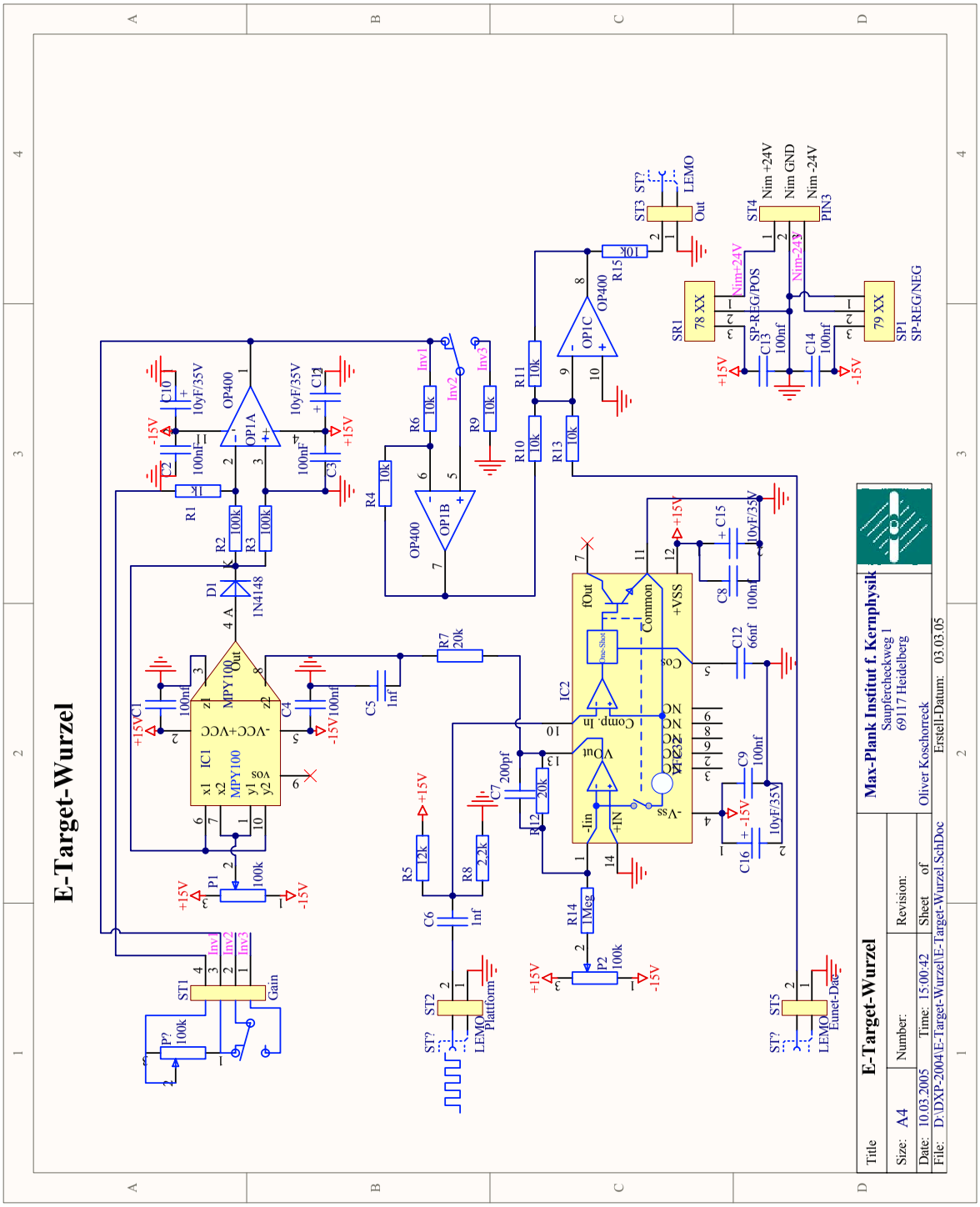


**Fig. B.1:** *Layout of the electronics for correction of the toroidal drift. Drawing courtesy of Oliver Koschorreck.*

# List of Figures

# Bibliography


[ABG+01] M. Audard, E. Behar, M. Güdel, A. J. J. Raassen, D. Porquet, R. Mewe, and C. R. Foley. The XMM-Newton view of stellar coronae: High-resolution X-ray spectroscopy of Capella. *Astron. & Astrophys.*, 365:L329–L335, 2001.

[Ale90] A. V. Aleksandrov. Electron spread from GaAs photoemitter. Unpublished, 1990.

[B+95] S. Baird et al. Measurement of the lifetime of $Pb^{52+}$, $Pb^{53+}$ and $Pb^{54+}$ beams at 4.2 MeV per nucleon subject to electron cooling. *Phys. Lett. B*, 361:184, 1995.

[BCTT05] P. Beiersdorfer, H. Chen, D. B. Thorn, and E. Träbert. Measurement of the Two-Loop Lamb Shift in Lithiumlike $U^{89+}$. *Phys. Rev. Lett.*, 95:233003, 2005.

[BI00] S. Boucard and P. Indelicato. Relativistic many-body and QED effects on the hyperfein structure of lithium-like ions. *Eur. Phys. J. D*, 8:59–73, 2000.

[BKM+91] V.G. Baryshevsky, M.V. Korzhik, V.I. Moroz, V.B. Pavlenko, and A.A. Fyodorov. $YAlO_3$:Ce-fast-acting scintillators for detection of ionizing radiation. *Nucl. Instrum. Methods B*, 58:291–293, 1991.

[BR91] P. R. Bevington and K. D. Robinson. *Data Reduction and Error Analysis for the Physical Sciences*. McGraw-Hill, second edition, 1991.

[BS57] H. A. Bethe and E. E. Salpeter. *Quantum Mechanics of One- and Two-Electron-Atoms*. Plenum Press, New York, 1957.

[Buh06] H. Buhr. *Electron collisions and internal excitation in stored molecular ion beams*. Dissertation, Universität Heidelberg, 2006.

[CDMU99] J. R. Crespo Lopéz-Urrutia, A. Dorn, R. Moshammer, and J. Ullrich. The Freiburg Electron Beam Trap/Source Project FreEBIT. *Phys. Scr.*, T80:502, 1999.

[Cow81] R. D. Cowan. *The Theory of Atomic Structure and Spectra*. University of California Press, 1981.

[DAB+94] H. Danared, G. Andler, L. Bagge, C. J. Herrlander, J. Hilke, J. Jeansson, A. Källberg, A. Nilsson, A. Paál, K.-G. Rensfelt, U. Rosengård, J. Starker, and M. af Ugglas. Electron cooling with an ultracold electron beam. *Phys. Rev. Lett.*, 72(24):3775, 1994.

[DKL+88] N. S. Dikansky, V. I. Kudelainen, V. I. Lebedev, V. A. Meshkov, V. V. Parkhomchuk, A. A. Sery, A. N. Skrinsky, and B. N. Sukhina. Ultimate possibilities of electron cooling. *Institute of Nuclear Physics, Novosibirsk, Preprint*, 88-61, 1988.

[FCD+04] K. A. Flanagan, C. R. Canizares, D. Dewey, J. C. Houck, A. C. Fredericks, M. L. Schattenburg, T. H. Markert, and D. S. Davis. Chandra High-Resolution X-Ray Spectrum of Supernova Remnant 1E 0102.2-7219. *Astrophys. J.*, 605:230–246, 2004.

[Fri05] S. Fritzsche. private communication, 2005.

[GH+00] G. Gwinner, A. Hoffknecht, et al. Influence of Magnetic Fields on Electron-Ion Recombination at Very Low Energies. *Phys. Rev. Lett.*, 84:4822, 2000.

[Gri06] M. Grieser. private communication, 2006.

[GS03] G. F. Gribakin and S. Sahoo. Mixing of dielectronic and multiply excited states in electron-ion recombination: A study of $Au^{24+}$. *J. Phys. B*, 36:3349–3370, 2003.

[GSZ+97] H. Gao, R. Schuch, W. Zong, et al. Energy and charge dependence of the rate of electronion recombination in cold magnetized plasmas. *J. Phys. B*, 30:L499, 1997.

[Gu02] M. F. Gu. $\Delta N = 0$ Dielectronic Recombination as a Line formation Process in Photoionized Plasmas. *Astrophys. J.*, 579:L103–L106, 2002.

[HFK+98] G. Hölzer, E. Förster, D. Klöpfel, P. Beiersdorfer, G. V. Brown, J. R. Crespo López-Urrutia, and K. Widmann. Absolute wavelength measurement of the Lyman-$\alpha$ transitions of hydrogenic $Mg^{11+}$. *Phys. Rev. A*, 57:945, 1998.

[Hof] J. Hoffmann. Dissertation. In preparation.

[HYTB03] M. Hörndl, S. Yoshida, K. Tökési, and J. Burgdörfer. Enhancement of Low-Energy Electron Ion Recombination in a Magnetic Field. *Hyperfine Interact.*, 146–147:13, 2003.

[HYW+05] M. Hörndl, S. Yoshida, A. Wolf, G. Gwinner, and J. Burgdörfer. Enhancement of Low Energy Electron-Ion Recombination in a Magnetic Field: Influence of Transient Field Effects. *Phys. Rev. Lett.*, 95:243201, 2005.

[IM01] P. Indelicato and P. M. Mohr. Coordinate-space approach to the bound-electron self-energy: Self-energy screening calculation. *Phys. Rev. A*, 63:052507, 2001.

[Jac81] J. D. Jackson. *Klassische Elektrodynamik*. de Gruyter, 1981.

[JS85] W. R. Johnson and G. Soff. The Lamb Shift in Hydrogen-like Atoms, 1 ¡ 2 6 110. *At. Data Nucl. Data Tables*, 33:405, 1985.

[KBC+95] D. A. Knapp, P. Beiersdorfer, M. H. Chen, J. H. Scofield, and D. Schneider. Observation of Interference between Dielectronic Recombination and Radiative Recombination in Highly Charged Uranium Ions. *Phys. Rev. Lett.*, 74:54, 1995.

[KBID91] Y.-K. Kim, D. H. Baik, P. Indelicato, and J. P. Desclaux. Resonance transition energies in Li-, Na-, and Cu-like ions. *Phys. Rev. A*, 44:148, 1991.

[KHS+92] G. Kilgus, D. Habs, D. Schwalm, A. Wolf, N. R. Badnell, and A. Müller. High-resolution measurement of dielectronic recombination of lithiumlike $Cu^{26+}$. *Phys. Rev. A*, 49:5730, 1992.

[Kih01] T. Kihm. *VME library manual*. Mizzi Computer Software GmbH, 2001.

[Kra] C. Krantz. Dissertation, Universität Heidelberg.

[Kra92] P. Krause. *Temperaturrelaxation in magnetisierten Elektronenstrahlen*. Dissertation, Universität Heidelberg, 1992.

[KSS+04] S. Kieslich, S. Schippers, W. Shi, A. Müller, G. Gwinner, M. Schnell, A. Wolf, E. Lindroth, and M. Tokman. Determination of the 2s-2p excitation energy of lithiumlike scandium using dielectronic recombination. *Phys. Rev. A*, 70:042714, 2004.

[KVS01] J. H. Kastner, S. D. Vrtilek, and Noam Soker. Discovery of extended X-ray Emission from the Planetary Nebula NGC 7027 by the CHANDRA X-ray Observatory. *Astrophys. J.*, 550:L189–L192, 2001.

[Les06] M. Lestinsky. *mileDAQ Programmers Manual*. Max-Planck-Institut für Kernphysik, 2006. WWW: `http://www.mpi-hd.mpg.de/etarget/miledaq/`.

[Ley97] R. Ley. Positron Production Using Accellerators. *Hyperfine Interact.*, 109:167, 1997.

[Lin06] E. Lindroth. Private communication, 2006.

[LMB+89] M. A. Levine, R. E. Marrs, J. N. Bardsley, P. Beiersdorfer, C. L. Bennett, M. H. Chen, T. Cowan, D. Dietrich, J. R. Henderson, D. A. Knapp, A. Osterheld, B. M. Penetrante, M. B. Schneider, and J. H. Scofield. The use of an electron beam ion trap in the study of highly charged ions. *Nuclear Instruments and Methods in Physics Research B*, 43:431–440, September 1989.

[LS78] C. M. Lederer and V. S. Shirley, editors. *Table of Isotopes*. Wiley Interscience, New York, 1978.

[LSH] M. Lestinsky, F. Sprenger, and J. Hoffmann. *Electron Target Knowledgebase*. Max-Planck-Institut für Kernphysik. Internal documentation. WWW: `http://www.mpi-hd.mpg.de/etarget/wiki/`.

[LWH+96] A. Lampert, A. Wolf, D. Habs, J. Kenntner, G. Kilgus, D. Schwalm, M. S. Pindzola, and N. R. Badnell. High-resolution measurement of the dielectronic recombination of fluorinelike selenium ions. *Phys. Rev. A*, 53:1413–1423, 1996.

[MEK94] R. E. Marrs, S. R. Elliott, and D. A. Knapp. Production and Trapping of Hydrogenlike and Bare Uranium Ions in an Electron Beam Ion Trap. *Phys. Rev. Lett.*, 72:4082–4085, 1994.

[MHK+96] G. Miersch, D. Habs, J. Kenntner, D. Schwalm, and A.Wolf. Fast scintillators as radiation resistant heavy-ion detectors. *Nucl. Instrum. Methods A*, 369:277–283, 1996.

[MMM+02] T. Minamisono, K. Matsuta, K. Minamisono, S. Kudo, M. Ogura, S. Fukuda, K. Sato, M. Mihara, M. Fukuda, S. Takeda, and S.Y. Zhu. Quadrupole Moments of the $^{40}$Ca Core Plus One Nucleon Nuclei $^{41}$Sc and $^{41}$Ca. *Z. Naturforsch.*, 57a:595, 2002.

[NKB+03] H. Netzer, S. Kaspi, E. Behar, et al. The Ionized Gas and Nuclear Environment in NGC 3783. IV. Variability and Modeling of the 900 Kilosecond Chandra Spectrum. *Astrophys. J.*, 599:933–948, 2003.

[NLK+04] D. Nikolić, E. Lindroth, S. Kieslich, C. Brandau, S. Schippers, W. Shi, A. Müller, G. Gwinner, M. Schnell, and A. Wolf. Dielectronic recombination resonances in $Na^{8+}$. *Phys. Rev. A*, 70:062723, 2004.

[Nov04] S. Novotny. *Fast-beam molecular fragmentation imaging using a high-speed gated camera system*. Diplomarbeit, Universität Heidelberg, 2004.

[OGA+06] I. Orban, P. Glans, Z. Altun, E. Lindroth, A. Källberg, and R. Schuch. Determination of the recombination rate coefficients for Na-like Si IV forming Mg-like Si III. *Astron. & Astrophys.*, 459:291–296, 2006.

[OH85] T. M. O'Neil and P. G. Hjorth. Collisional dynamics of a strongly magnetized pure electron plamsa. *Phys. Fluids*, 26:2128, 1985.

[OSL+05] D. A. Orlov, F. Sprenger, M. Lestinsky, W. Weigel, A. S. Terekhov, D. Schwalm, and A. Wolf. Photocathodes as electron sources for high resolution merged beam experiments. *J. Phys.: Conf. Ser.*, 4:290, 2005.

[Pot90] H. Poth. Electron cooling: theory, experiment, application. *Phys. Reports*, 196:135–297, 1990.

[Rei05] S. Reinhardt. *Measurement of Time Dilation by Laser Spectroscopy on Fast Stored Lithium Ions*. Dissertation, Universität Heidelberg, 2005.

[SCC+80] S. Suckewer, J. Cecci, S. Cohen, R. Fonck, and E. Hinnov. Tracer Element Injection into PDF Tokamak for Spectral Line Identification and Localized Doppler Temperature Measurement. *Phys. Lett.*, 80A:259, 1980.

[Scha] S. Schippers. Private communication.

[Schb] E. W. Schmidt. Dissertation, Universität Gießen. In preparation.

[Sch03] M. Schnell. *Di- und trielektronische Rekombination an berylliumähnlichen Ionen*. Dissertation, Universität Heidelberg, 2003.

[SD06] R.A. Sunyaev and D. Docenko. Hydrogen-like Nitrogen radio line from hot interstellar and warm-hot intergalactic gas. *arXiv*, astro-ph:0608256-v3, 2006.

[SG78] S. Saini and M. R. Gunye. Nuclear structure of $^{45,47}$Sc. *Phys. Rev. C*, 18:2879, 1978.

[SLO+04] F. Sprenger, M. Lestinsky, D.A. Orlov, D. Schwalm, and A. Wolf. The high-resolution electronion collision facility at TSR. *Nucl. Instrum. Methods A*, 532:298–302, 2004.

[SPA04] SPARC Collaboration. Letter of Intent for Atomic Physics and Installations at the International FAIR Facility, 2004.

[Spr03] F. Sprenger. *Production of Cold Electron Beams for Collision Experiments with Stored Ions*. Dissertation, Universität Heidelberg, 2003.

[SSB+07] S. Schippers, E. W. Schmidt, D. Bernhardt, D. Yu, A. Müller, M. Lestinsky, D. A. Orlov, M. Grieser, R. Repnow, and A. Wolf. Storage ring measurement of the hyperfine induced $^{47}Ti^{18+}$ ($2s\ 2p\ ^3P_0 \rightarrow 2s^2\ ^1S_0$) transition rate. *Phys. Rev. Lett.*, 98:033001, 2007.

[SSM+06] E. W. Schmidt, S. Schippers, A. Müller, M. Lestinsky, F. Sprenger, M. Grieser, R. Repnow, A. Wolf, C. Brandau, D. Lukic, M. Schnell, and D. W. Savin. Electron-Ion Recombination Measurements Motivated by AGN X-Ray Absorption Features: Fe XIV Forming Fe XIII. *Astrophys. J.*, 641:L157, 2006.

[SST97] V. M. Shabaev, M. B. Shabaeva, and I. I. Tupitsyn. Hyperfine structure of Lithium-like Ions. *Astronomical and Astrophysical Transactions*, 12:243–246, 1997.

[ST00] Q. Spreiter and C. Toepffer. A screening model for density enhancement near ions at rest in magnetized electron plasmas. *J. Phys. B*, 33:2347, 2000.

[Sv65] J. J. Scheer and J. van Laar. GaAs-Cs: A new type of photoemitter. *Solid State Commun.*, 3:189–193, 1965.

[SW50] R. E. Sheriff and D. Williams. The Nuclear Magnetic Moment of Scandium$^{45}$. *Phys. Rev.*, 79:175, 1950.

[TEG+02] M. Tokman, N. Eklöw, P. Glans, E. Lindroth, R. Schuch, G. Gwinner, D. Schwalm, A. Wolf, A. Hoffknecht, A. Müller, and S. Schippers. Dielectronic recombination resonances in $F^{6+}$. *Phys. Rev. A*, 66:012703, 2002.

[U+97a] O. Uwira et al. Recombination measurements at low energies with $Ar^{16+}$ and $Ar^{18+}$ ions in a dense, cold electron target. *Hyperfine Interact.*, 108:167, 1997.

[U+97b] O. Uwira et al. Recombination measurements at low energies with $Au^{49+,50+,51+}$ at the TSR. *Hyperfine Interact.*, 108:149, 1997.

[WBD+95] K. Widmann, P. Beiersdorfer, V. Decaux, S. R. Elliott, D. Knapp, A. Osterheld, M. Bitter, and A. Smith. Studies of He-like krypton for use in determining electron and ion temperatures in very-high-temperature plasmas. *Rev. Sci. Instrum.*, 66:761, 1995.

[Wei03] U. Weigel. *Cold Intense Electron Beams from Gallium Arsenide Photocathodes*. Dissertation, Universität Heidelberg, 2003.

[Wis02] G. Wissler. *Ein Detektorsystem für Umladungs- und Fragmentationsexperimente mit gespeicherten Ionen*. Dissertation, Universität Heidelberg, 2002.

[YAS+05] V. A. Yerokhin, A. N. Artemyev, V. M. Shabaev, G. Plunien, and G. Soff. Screened Self-energy Correction to the $2pi_{3/2}2s$ Transition Energy in Li-Like Ions. *Optics and Spectroscopy*, 99:12–17, 2005.

[ZWS+05] D. Zajfman, A. Wolf, D. Schwalm, D. A. Orlov, M. Grieser, R. von Hahn, C. P. Welsch, J. R. Crespo Lopez-Urrutia, C. D. Schröter, X. Urbain, and J. Ullrich. Physics with colder molecular ions: the Heidelberg Cryogenic Stroage Ring CSR. *J. Phys.: Conf. Ser.*, 4:296, 2005.

# Acknowledgments

A work such as this would not have been possible without a lot of support from many people and I am pleased to acknowledge their efforts. And the first mentioned should be my parents, who have supported my studies in the field of physics and thus laid the foundation of this work.

I would like to thank Prof. Andreas Wolf for allowing me to join his workgroup and perform this work. I am deeply indebted for his helpful and forgiving supervision.

I'm grateful to all of my colleagues for the nice working atmosphere and insightful discussions. Especially should be pointed out Dr. Dmitry Orlov and Jens Hoffmann, and my former colleagues Dr. Frank Sprenger and Dr. Michael Schnell. It was the responsibility of Mrs. Helga Krieger, that we were supported with the best coffee machine money can buy and all kudos go to her.

Mr. Oliver Koschorreck and Christian Föhr from the electronics workshops, and Dr. Frank Köck and Dr. Thomas Kihm have contributed wise advices during the design and setup phases of all the used electronic components and I gratefully acknowledge their help. Rolf Epking's kind support with the EUNet setup is appreciated. The skillful support of the mechanical workshops of Mr. Hahn and Mr. Mallinger should not be unmentioned here, as well.

The accelerator operator team, lead by Dr. Roland Repnow and Dr. Robert von Hahn, did a fantastic job to provide beautiful ion beams. And Dr. Manfred Grieser and Kurt Horn generously devoted *their* TSR and their manpower to these experiments.

The experiments have been carried out in a fruitful collaboration with the working group of Prof. Alfred Müller, University of Giessen, and especially Dr. Stefan Schippers and Eike Schmidt should be named. The same holds true for Prof. Daniel Savin and his companions at the astrophysics department, Columbia University, NY. Dr. Stephan Fritzsche, Univerisity of Kassel supported this work with theoretical calculation of DR in $Mg^{11+}$.

This work received partial financial support by the NASA Space Astrophysics Research and Analysis program, grant number NAG5-5420, through Prof. Daniel Savin, and by the GSI, Darmstadt within the framework of the GSI Hochschulprogramm through Prof. H.-Jürgen Kluge, Dr. Christophor Kozhuharov, and Dr. Carsten Brandau.

Last, but not least I thank Kathrin for all her moral support and patience.